# The Sky as a Laboratory

2009-2010

Project Director
Prof. Piero Rafanelli
Dept. of Astronomy, Padova University

Scientific Coordinators Stefano Ciroi Valentina Cracco Alessandra Frassati

Scientific Collaborators Elena Dalla Bontà Rosaria Tantalo

Project Secretary Rossella Spiga

# **Preface**

This book collects the final scientific reports of the students, who took part in the observational training periods organized in February 2010 at the Asiago Astrophysical Observatory in the frame of the IX Edition of The Sky as a Laboratory, the educational project of the Department of Astronomy of Padova University, addressed to the Secondary Schools of the Veneto Region (Italy). Created by Prof. Piero Rafanelli, currently Head of the Dept., and carried out by means of a close cooperation between the scientific and technical staff of the Dept., and the teachers of the participating schools, every year this project involves about 300-350 Secondary School students, 40-45 teachers and 35 institutes.

The main aim of The Sky as a Laboratory is to introduce a new approach in teaching and learning astronomy, through the interpretation of the observed celestial phenomena and the use of the physical and mathematical tools available to the students. This project allows the students to deepen the issues studied at school and makes a link among astronomy, physics, mathematics, and chemistry. In addition it guides the students to the university choice, since it allows them to be exposed to the university environment and scientific research.

The first part of the project consists of 7 lectures of fundamentals of astrophysics given by the teachers of the 10 reference schools and by the scientific staff of the Dept. Then, a competitive test allows to select the 50 most eligible and motivated students, who will attend a training period of 3 days and 3 nights at the 122 cm Galileo Telescope of the Asiago Astrophysical Observatory. This training gives the students a chance to deepen the knowledge they acquired during astronomy classes both at school and during the project. In addition, they receive 1 or 2 ECTS from the Science Faculty of Padova University.

The project ended on May 11th, 2010 with the official presentation of the scientific reports by the students at the Dept. of Astronomy.



## PSF photometry of the globular cluster M53

Tommaso Spanio<sup>1</sup>, Franceschini Giacomo<sup>1</sup>, Saltalamacchia Stefano<sup>1</sup>

<sup>1</sup>Liceo *U.Morin*, sez.Scientifico, Mestre(VE)

**Abstract.** We studied the PSF photometry of the glubular cluster M53, using images taken from both ground, with g and r filters, and space, with f555w and f439w filters. Our purpose was to derive information in order to draw an H-R diagram and to determine several parameters of the cluster, such as distance, magnitude and star population distribution.

#### 1. Introduction

Our aim was to obtain the information necessary in order to build an H-R diagram of the glubular cluster M53 through PSF (Point Spread Function) photometry of images taken from both ground and space. Studying the diagram, we were able to deduce the cluster's main properties, such as distance, magnitude, age estimation and stellar population distribution. Quoting Messier catalogue, the cluster M53 is one of the most remote clusters of the Milky Way, being located at a distance of 6 kly from the centre of the galaxy; it can be easily found at 1° NE of Alpha Comae Berenices. Like every other globular cluster, it is mainly populated by first generation stars (old stars of population II). The most unusual aspects of this cluster are its 112 km/s velocity towards the Earth and its metallicity under the average (with metallicity we indicate every element heavier than helium the cluster is composed of) which is an important factor in determining cluster's age.

Object	Globular Cluster M53
Right Ascension	13:12.9 (h:m)
Declination	+18:10 (deg:m)
Constellation	Comae Berenices

#### 2. Observational Data

For our work we used four images of M53, two taken from ground by the Sloan Digital Sky Survey (SDSS) project and two taken from space by the Hubble Space Telescope (HST). The SDSS Project supplies high-detailed sky images thanks to a 2.5m telecope placed on Apache Point Observatory, New Mexico, equipped with a 120 Mpx CCD camera (with a scale of 0.4"/pixel). Images had been taken with two different filters: g and

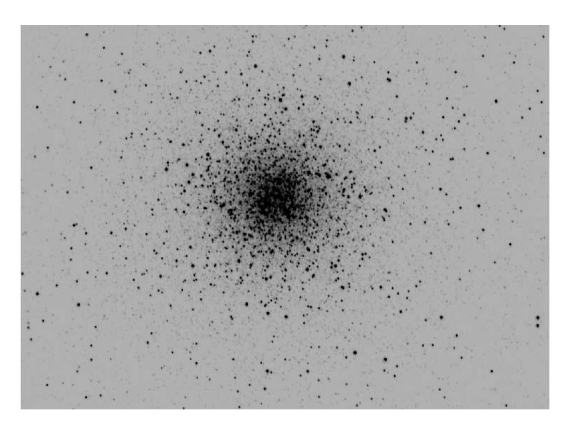


**Fig. 1.** The glubular cluster M53 captured in the g filter, with reverse colors.

r of ugriz system. These filters are centered on precise wavelenghts, in order to observe in specific ranges of the electromagnetic spectrum. More precisely, g filter is centered at 4686 Å, while r filter at 6165 Å.

Images were taken from space with HST, which, thanks to its advantageous position in the high atmosphere layers, does not suffer from the many disadventages ground telescopes have to, such as light absorption or refraction (also called seeing effect). HST utilizes WFPC2, a sophisticated camera equipped with four 800x800 pixels arrays. The images had been taken with the f439w filter and the f555w filter. These filters approximate the Johnson-Cousins system B and V filters, respectively: f439w filter is centred at 4282Å, with a bandwidth of 464 Å, f555w filter is centred at 5345 Å, with a bandwidth of 1500 Å.

#### 3. Work description

The method we followed to produce the magnitudecolor diagram of the globular cluster M53 is divided

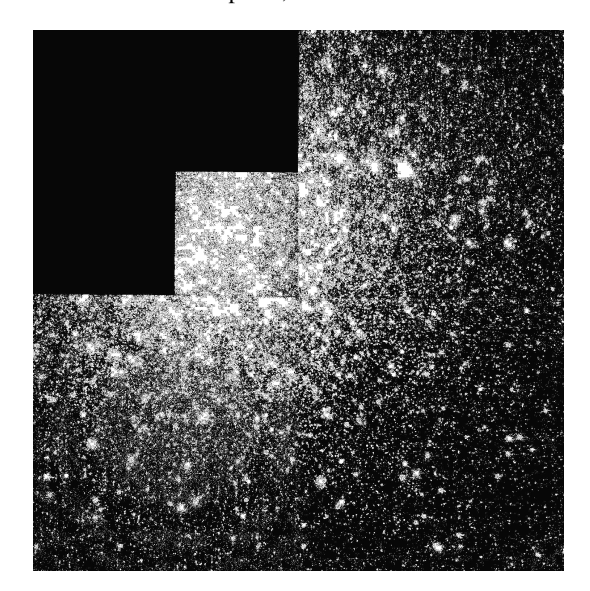


**Fig. 2.** The cluster M53 image taken by the HST in the f349w filter.

into two main parts. The first part consists in the images analysis, trough aperture and PSF photometry, to calculate the magnitude of every single distinguishable star in the cluster, while the second part consists in generating and analysing the graph from the data obtained in the first part.

#### 3.1. Part One - Data Analysis

The analysis of observational data was carried out with the photometry analysis software package of IRAF (Image Reduction and Analysis Facility) offered by N.O.A.O (National Optical Astronomy Observatories) from Tucson, Arizona.

The first step in the analysis is the count of stars in every image, starting from g filter. Stars are identified as sources in pixels (or pixel areas) that have photon counts higher than the sum of the value of the sky counts and the standard deviation multiplied by a treshold value. The standard deviation is the error in the determination of the mean flux coming from the background sky. Usually several attempts with different treshold values are made, until the software identifies a reasonable number of stars. This is, anyway, an approximated count because in images of clusters (expecially globular ones) certain areas reach sources densities so high that is too difficult to solve the stars separately. The software identifies, then, sources that satisfy the following relation:

$$I_{star} > I_{sky} + threshold * stdev_{sky}$$
 (1)

where  $I_{star}$  are the photon counts of the source,  $I_{sky}$  the background counts, *threshold* is the error threshold we provided and  $stdev_{sky}$  is the standard deviation calculated as above. The software was able to find around 30000-40000 stars.

We then proceeded with the aperture photometry. Aperture photometry is a tecnique used to derive the magnitude of the stars from their photon counts in a CCD image, according to equation (2):

$$m_{instr} = 25 - 2.5 \log(\frac{lum - I_{sky}}{t_{exp}})$$
 (2)

where in the logarithm there is the subtraction of the background counts from the photon counts of the star, divided by the exposure time. The conventional value 25 is added in order to make every magnitude positive and easier to work with. It is important to point out that we used aperture photometry just as a rough estimation of the magnitude, to prepare the PSF model later described. In fact, magnitudes calculated with the aperture photometry method suffer from a considerable issue when stellar sources are too dense: if in the image stars are too close one another, as in our case, the magnitude calculation suffers from a flux superposition on the same line of sight. To avoid this disturbing consequence, we adopted the PSF technique. This method consists in generatig a mathematical model of the PSF, which represents the distribution of photons emitted by a stars and detected by the CCD. More precisely, it is a gaussian curve, whose axis is centered on the source emission peak and which describes the light distribution drifting away from the centre. The twodimensional curve is then rotated in order to generate a three dimensional curve: the PSF (fig??). In order to

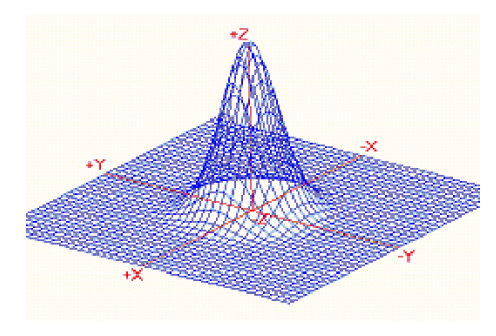


Fig. 3. A 3D graph of a PSF.

make an effective PSF model, we had to generate it using a proper sample of stars, expressly chosen according with their regular radial profile, with no saturation, and their isolated location, but uniformly distributed throughout the frame. With the list of the appropriate stars, there are several functions that can be used to produce a mathematical model; IRAF can choose the one that best fits the profile. Once the PSF was built, we fitted each source previously found with it obtaining the PSF magnitude, and generated a new image with fitted stars removed. Then, using residual images, we applied all over again the previous steps to the residual stars. This process is iterated several times, in order to fit as many stars as possible.

# 3.2. Part Two – Generation and analysis of the graphs

At this point we had several files containing information about fitted stars in g an r filter images from ground, f555w and f439w from space. The date we were interested in were magnitude and coordinates, therefore we extracted and joined them in one file for each image, in order to be analyzed with Topcat. Topcat is a graphic editor software that easily handles data tables in order to generate graphs, as well as to make calculations on the data themelves. Topcat is developed and released as a part of the AstroGrid project. With Topcat we created two H-R diagrams, one built from the ground data and the other from the space data. The procedure to follow is slightly different for the two diagrams.

#### SDSS data

The very first thing to do was to match the coordinates found in g and r filter images, in order to ensure to be working with the same stars in both images. This was done with Topcat by finding the match between the coordinates inside a radius in pixels, which also determines the error. After many attempts, we found a reasonable radius of 5 pixels. We calculated calibrated g and r magnitudes with the equation (3):

$$m_{cal} = m_0 + (m_{instr} - 25) - k \cdot x$$
 (3)

in this equation,  $m_0$  stands for the photometric zero point,  $m_{instr}$  is the instrumental magnitude (from which is subtracted 25, previously added), k is the atmospheric extinction coefficient, representing the light absorption rate in magnitudes per airmass units, and x is the airmass. In the following table we report the values we used.

filter	$m_0$	k	X
g	24.3941	0.1893	1.118
r	23.9759	0.1095	1.1095

Then, it was necessary to convert all magnitudes to the standard UBVRI system, in order to compare the two graphs. The conversion was carried out trough the equations (4) and (5):

$$B = 0.349 \cdot (g_{cal} - r_{cal}) + 0.245 + g_{cal}$$
 (4)

$$V = -0.569 \cdot (g_{cal} - r_{cal}) + 0.021 + g_{cal}$$
 (5)

We also calculated the color index B-V.

These conversion formulas have been formulated to compensate the differences in SDSS outputs from the ones in the UBVRI system. We were therefore able to create the color-magnitude diagram.

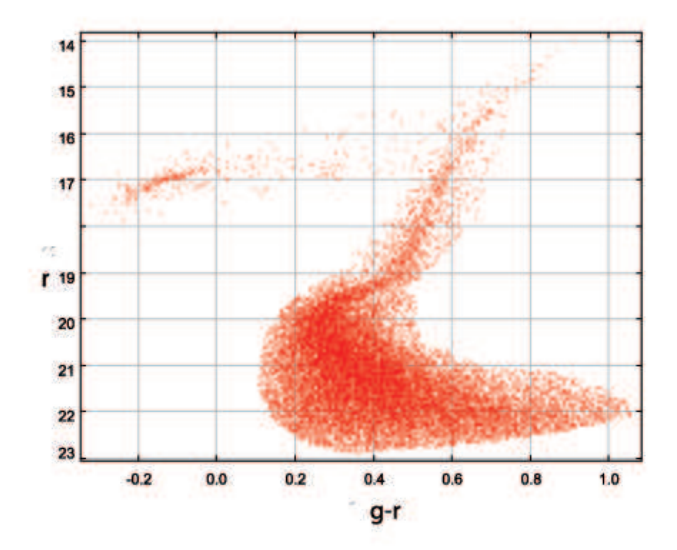


Fig. 4. The H-R diagram obtained with the SDSS data.

#### **HST** data

A similar procedure, but slightly more complicated, allowed us to obtain B and V magnitudes from the images taken with f555w and f439w filters. Therefore, we repeated the method to match the coordinates and we calculated calibrated magnitudes with equation (6).

$$m_{cal} = ZEROPOINT + (m_{instr} - 25)$$
 (6)

This equation is simplified because no light absorption compensation is needed for space images. ZEROPOINT is calculated with equation (7).

$$ZEROPOINT = -2.5 \cdot log_{10}(PHOTFLAM) + PHOTZPT(7)$$

where PHOTFLAM and PHOTZPT are keywords of the image header. Nevertheless, the resulting magnitudes are in the STMAG system. To transform these values into UBVRI magnitudes, some correction factors had been calculated. More precisely, correction factors change in relation to the spectral class of the objects. We were then forced to choose the most probable spectral class of the stars belonging to the globular clusters (globular clusters are populated by old, cold stars therefore low-temperature ones, such as G, K and M) and calculate an average factor. Then with equations (8) and (9) we found B and V magnitudes for HST data as well.

$$B = m_{f439w} + 0.4575 \tag{8}$$

$$V = m_{f555w} - 0.0166 \tag{9}$$

At this point we were able to generate the second graph (see fig.3) and we proceeded with the conclusions.

#### 4. Results

#### 4.1. Distance

To calculate the cluster distance, we adopted the RR Lyrae method: RR Lyrae are an important class of pulsating variable stars, which take up a specific zone of the H-R diagram (the so-called instability strip). This zone is approximately located between the red giant branch and the horizontal branch. Their name derives from the reference model which is, indeed, a star of the Lyra constellation. RR Lyrae are similar to Cepheids, but much less bright: they are about 40-50 times brighter than the Sun, whereas Cepheids are usually 100-10000 times brighter. For this reason, they can not be used for extragalactic distances, but they work perfectly with globular clusters ones. Since theorethical models can derive several parameters of these stars, such as luminosity or absolute magnitude, we are able to calculate the distance, using formula (10):

$$d = 10^{(m-M+5)/5} (10)$$

where m is the apparent magnitude of the RR-Lyrae stars, obtained from our diagram, while M is the absolute magnitude. With M=0.5 and m=16.80, we obtained a distance of approximately 19kpc, which is consistent with catalogues data.

# 4.2. Cluster dimension and stars distribution from cluster center

By determining the stars coordinates, all over the cluster, we can calculate both cluster dimension and stellar distribution. To find the coordinates, we examined the image with ds9, and we determined pixel coordinates. Knowing that the pixel scale is 0.4"/px and having previously calculated the distance, we can calculate the angle ( $\theta$ ) subtained by the cluster in radiants, and then the diameter (D) in parsec, using the spatial scale (d in pc/") The formula that summarizes this process is the following:

$$D(pc) = d(pc/") \cdot \theta(") \tag{11}$$

where the subtained angle  $\theta$  is equal to:

$$\theta = d(px) * 0.4"/px \tag{12}$$

where 206265 is the number of arcseconds contained in a radiant. With a diameter of about 780 pixels, and the distance previously obtained, we foud a diameter of approximately 28.73 pc. To calculate the stellar distribution we needed to determine only the euclidean distance from the centre for each star of the cluster, by applying Pythagoras' theorem to the coordinates previously calculated. We were then able to make a cumulative distribution with Topcat, from which we observed that 90% of the stars are located no more than 55 pc from the cluster centre, as shown in fig.(5).

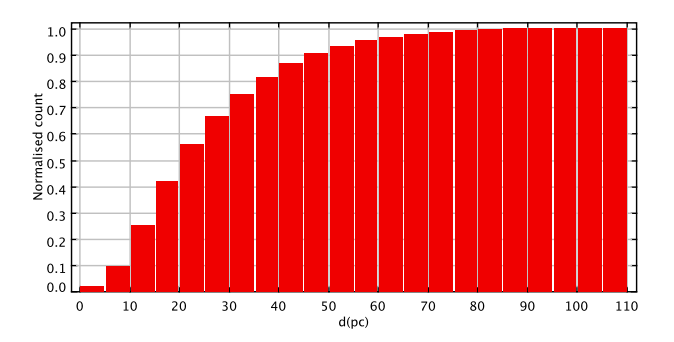


**Fig. 5.** The cumulative stars distribution of the cluster from its centre.

#### 4.3. Population distribution

Using Topcat, it was possible to color with different dyes specific areas of the H-R diagram. We used this task to observe where stars of different population are located in the cluster. We used green for main sequence stars, red for red giants and turn-off stars, blue for variables and horizontal branch stars. Then we re-organized the graph in order to have on x and y axis the real coordinates instead of magnitudes. The result is an image similar to the cluster one, in which we can identify different stellar populations. By studying this image we wanted understand if different kinds of stars have a different distribution. The results showed us no unusual configuration, as each star type equally distributes in the cluster (see fig.4).

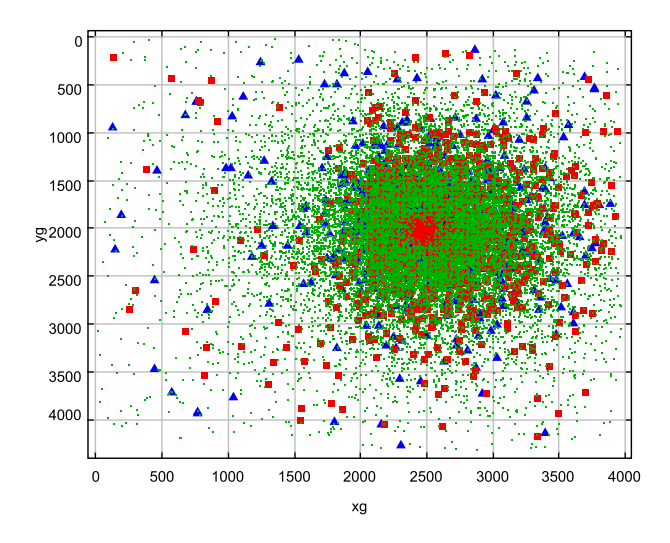


**Fig. 6.** The stellar population distribution. It seems there is an empty zone in the centre for main sequence stars, but it is just a software issue.

#### 4.4. Determining the age of the cluster

In order to determine the age of the cluster, we used a method that consists in fitting the data of the H-R diagram with theoretical models. Theoretical models of stellar evolution can produce the so-called *isochrone curves*. These curves reproduce the evolutionary trend of a group of stars of the same age, as in the globular cluster case. Their shape depends on many parameters, such as metallicity. Several isochrones with different ages and low metallicity (we used metallicity of 0.001) have been generated. Our task was to compare them with our H-R diagrams, in order to choose the one that best fitted our data. The isochrone age is then the cluster age, and in our case it is approximately 10.25 Gyr (see fig.7).

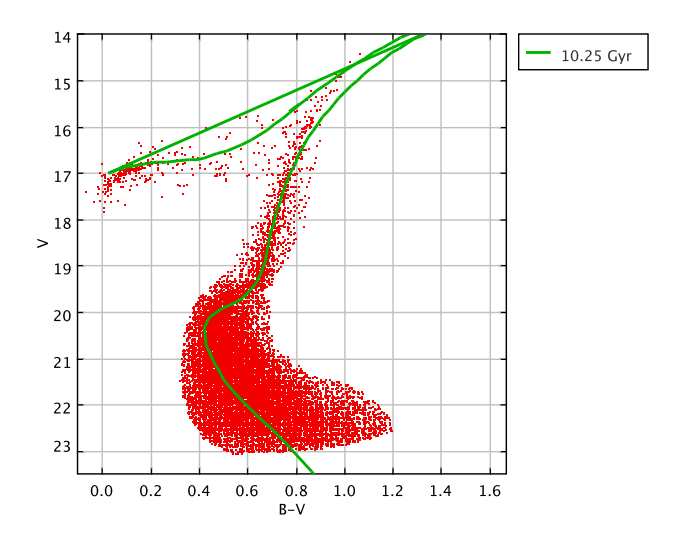


**Fig. 7.** The isocrone-diagram composition. We used a metallicity of 0.001.

#### References

www.stsci.edu www.astro.utoronto.ca www.astro.washington.edu seds.org www1.cadc-ccda.hia-iha.nrc-cnrc.gc.ca www.sdss.org



## Photometric analysis of the open cluster NGC 2420

Kevin Da Roit<sup>1</sup>, Jacqueline Tognetti<sup>1</sup>, Alessandro De Lorenzi<sup>2</sup>, Marco Michelini<sup>2</sup>

<sup>1</sup>Liceo Scientifico PNI *U. Follador*, Agordo <sup>2</sup>Liceo Scientifico *G. Galilei*, Belluno

**Abstract.** The working group studied the photometry of the stars of the open cluster NGC2420, in the Gemini constellation, with two different procedures: aperture photometry and PSF-method. Both methods allow to calculate the magnitude of stars: the first by counting the photons recorded from a pixel per second in a determined aperture; the second by determining a PSF model, which represents the distribution of the light on the digital support. The objective of the analysis is to verify whether the H-R diagrams, obtained with the two methods, are similar or not, in order to be able to assess the reliability of the procedures and to analyze analogies and differences between the results of the two methods.

#### 1. Introduction

An open cluster is a group of stars generated more or less at the same time from one giant molecular cloud; being tied by the mutual gravitational attraction, the stars are relatively close one another (even if an open cluster is less dense than a globular cluster) and therefore all of them are approximately at the same distance from Earth. Generally, they can be found inside the disc of spiral galaxies or in irregular galaxies. The open clusters are constituted by young stars of population I (therefore generally hot and very luminous); most of them are situated in the main sequence.

#### 2. Observational Data

The cluster hereby studied is NGC 2420. NGC 2420 is formed by approximately 1000 stars, which are dislocated in a spherical volume of 30 light-years of diameter. Since all the stars of a cluster have similar age, distance and composition, the clusters can be analyzed in order to study many different branches of astronomy.

Constellation	Gemini
Right Ascension	$07^h \ 38^m \ 23.9^s$
Declination	+21° 34' 27"
Galactic longitude	198.107
Galactic latitude	19.634
Apparent dimension	10'
Apparent magnitude	8.3



Fig. 1. The cluster NGC 2420

#### 3. Work description

The photometry was realized with the data (in the five ugriz filters) taken from the database Sloan Digital Sky Survey (SDSS). Each one of the five ugriz filters perceive different wavelengths; they cover the range betweenapproximately 3000 Å and 9000 Å. The image has been realized with a 120 Mpx CCD (Charde Coupled Device) using the 2.5 meters telescope situated at Apache Point in New Mexico (USA).

Filter	u	g	r	i	Z
λ	3551Å	4686Å	6165Å	7481Å	8931Å

In order to select stars for the photometry, in the images of every filter we calculated: the average background intensity;the average FWHM, that is the width

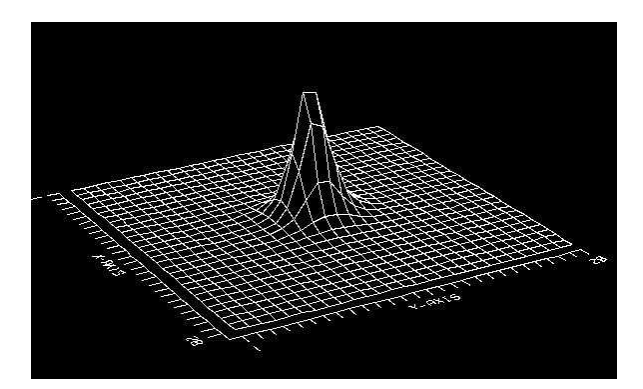


Fig. 2. The Point Spread Function model.

at half height of the Gaussian curve; the average apparent star radius ( $r = 4.5 \times FWHM$ ); the radius of the sky ring that surrounds the stars ( $r_{ring} = 6.5 \times FWHM$ ); the ring thickness ( $\Delta r = 1/4 \times r_{ring}$ ). The working group has been divided in two subgroups; each subgroup calculated the magnitudes of the starsof the cluster with one of the two methods (aperture photometry or PSF).

The "aperture photometry" method is used in order to determine the magnitude of stars; it consists in calculating how many photons flow in each pixel in a digital image of a luminous source (usually a star), adding the counts within one determined aperture (calculated from the typical FWHM of the stars in that image) centered on the peak of the source (the point with the highest brightness), and subtracting the counts concerning the background, determined in a ring centered on the star. We inserted the calculated data (average intensity of the background, average FWHM, average appearing radius, average radius of the sky ring and its thickness) in a program that calculates the magnitudes of the stars selected from the images of each filter. The Point Spread Function (PSF) represents the distribution of the light intensity emitted by a source on the digital support (CCD). It has the form of a Gaussian curve, rotated on the central vertical axis. In fact, the light that reaches from the dot-like source (considered so because of the distance) would have to arrive dot-likely on the support of the image. Actually that does not happen: it is diffracted passing through the telescope optics, and refracted by the atmospheric turbulence. These two effects cause the PSF form of the star image when reaching the receiving support, spread exactly according to this model of curve (fig 2).

Knowing this, it is possible to do the photometric analysis, which is the calculation of the luminous intensity emitted, counting the whole real luminous intensity emitted by the source towards the observer direction. The method based on PSF model is used in order to compare the results with those obtained with the aperture photometry, finding analogies and differences and discussing about the equivalence of the two procedures. Both methods, in fact, allow to find the rough magnitude of stars in the image and with those it is possible

to realize twoHR diagrams to compare. To select the stars on the image and make other calculations, we used the background data, average FWHM, average radius of stars, radius and average thickness of the sky ring as previously calculated. In order to obtain the magnitude, it is necessary to have a mathematical model that fits the PSF of stars in the image. We have to select some sample stars in the image whose PSF is representative of the PSF of all the stars, according to the following criteria:

- a) radial profile representative of the average profile of stars in the image;
- b) same FWHM as other stars in the image;
- c) reasonable brightness, but without saturation;
- d) isolation from other stars;
- e) distribution all over the image.

The program uses sample stars in order to choose the best fit of the PSF model and to calculate the rough magnitudes. Then the rough magnitudes of the two photometric systems (aperture photometry and PSF) are calibrated and converted from ugriz to Johnson system. The photometric calibration is the correction of the rough magnitudes in the photometric system (optics, CCD, filters, problems related to the presence of the atmosphere between the instrument and the observed object) in calibrated magnitudes in the standard photometric system. The calibration is carried out through the following formula:

$$\mathbf{m} = |\mathbf{m}_0| + (\mathbf{m}_s - \kappa) - \mathbf{k} \cdot \mathbf{X} \tag{1}$$

#### where:

- m is the calibrated magnitude;
- m<sub>0</sub> is the zero point of each filter (aa), that is the constant that we have to add to the magnitudes in order to pass from one measure of computations to the flux in physical units;
- m<sub>s</sub> is the instrumental magnitude previously calculated:
- $\kappa$  is a constant applied by the program to calculate  $m_s$  so to have positive values of the instrumental magnitude; in this case we took it equal to 25;
- k is extinction coefficient of every filter (kk);
- X is the air mass (airmass) in each filter, which depends on the amount of atmosphere crossed by the light before reaching the observer (the greater is the atmosphere crossed by the light, the greater it is the value of the air mass and the greater it is the attenuation suffered by the light).

ſ	filter	Airmass	aa	kk
ſ	u	1.06188012	23.3341	0.414047
	g	1.06481762	24.4471	0.142222
	r	1.05904983	24.0709	0.090216
	i	1.06045201	23.7411	0.034458
l	Z	1.06333527	21.8745	0.03363

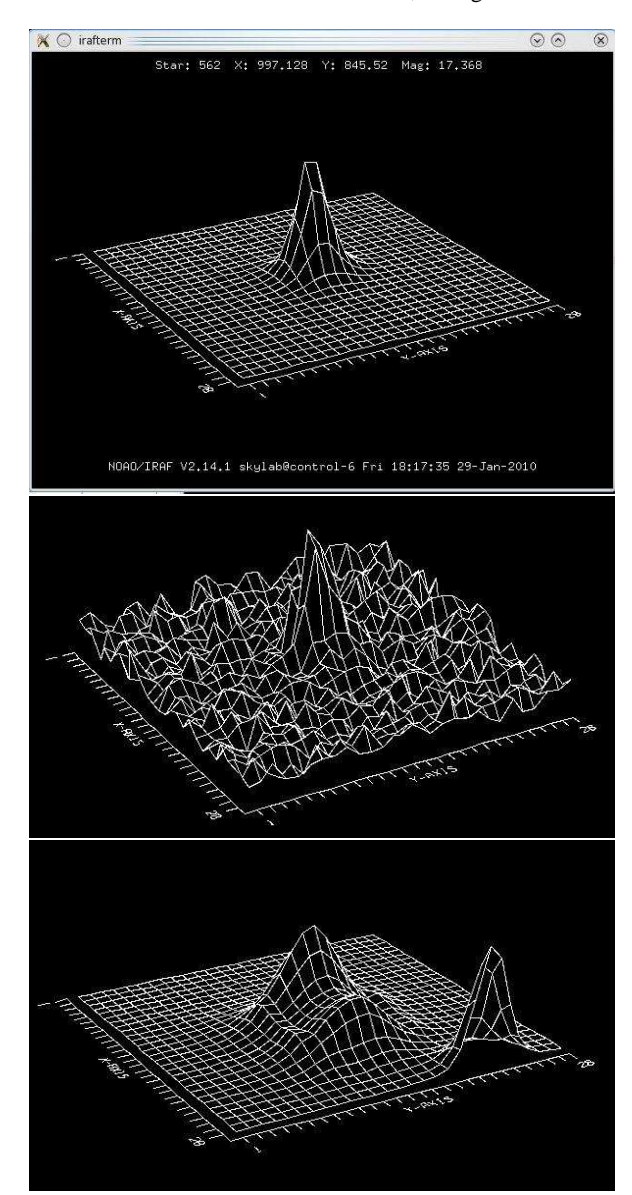


**Fig. 3.** Acceptable PSF model of a sample star (top); the PSF model of a star too weak—the model does not stand out from the background noise (center) and the PSF model of a star close to another—the wings are fused together (bottom).

After obtaining the calibrated magnitudes in the ugriz photometric system, they were converted in the Johnson system (UBVRI). The formulas used for the conversion are the following ones:

$$B = g + 0.313(g - r) + 0.219$$
 (2)

$$V = g - 0.565(g - r) - 0.016$$
 (3)

(where B and V are the magnitudes in the respective Johnson filters, and g and r the ones in the two ugriz filters) Now, with the calibrated magnitudes in the two band systems we made two H-R diagrams:

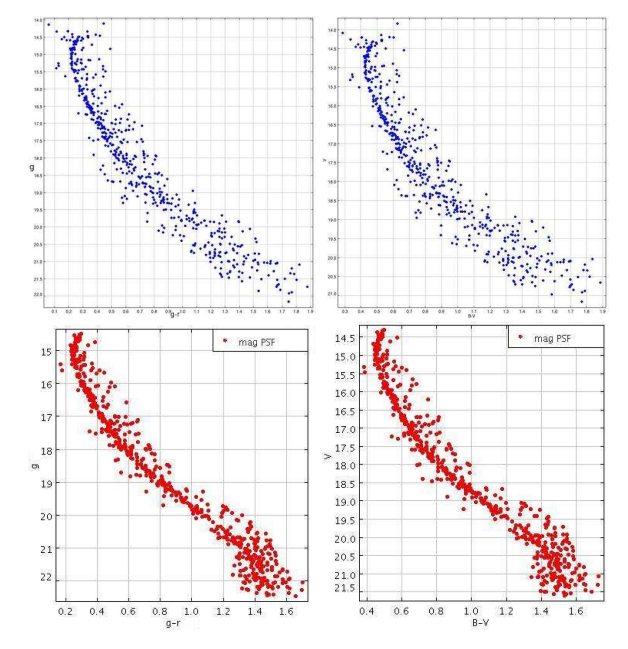


**Fig. 4.** HR diagram of NGC2420 in ugriz system obtained with aperture photometry method (upper left); H-R diagram of NGC2420 in the Johnson system obtained with aperture photometry method (upper right); H-R diagram of NGC2420 in the ugriz system obtained with the PSF method (bottom left); H-R diagram of NGC2420 in the Johnson system obtained with PSF method (bottom right).

- with the Johnson system: on the y axis we have the magnitude in the V-band and on the x axis the difference between the magnitudes in B band and V-band
- with the ugriz system: on the y axis the magnitude in g band, on the x axis the difference between the magnitudes in g band and r band.

Comparing the H-R diagrams, some consideration emerged:

- 1. The two curves show a good fit, especially in the middle-upper section;
- 2. The PSF method perceived a larger number of stars;
- 3. The tail of the curve (that is the bottom right portion of the graph) obtained with the PSF method has a clearer assessment than the one obtained with the aperture photometry, which is highly fragmented and has the tendency to spread out to the right.

In order to estimate the age of the cluster we made a comparison between the H-R diagram (B-V, V) and the isochrones (locus of points of equal age) which represent the H-R diagrams of coeval populations of stars, meaning that they all formed at the same time but with different initial mass. The H-R diagrams of isochronal traces had been drawn from theoretic data that are not affected by absorption (caused by the galactic plane) and they are in absolute magnitudes, while the experimental diagram is in apparent magnitudes. In our analy-

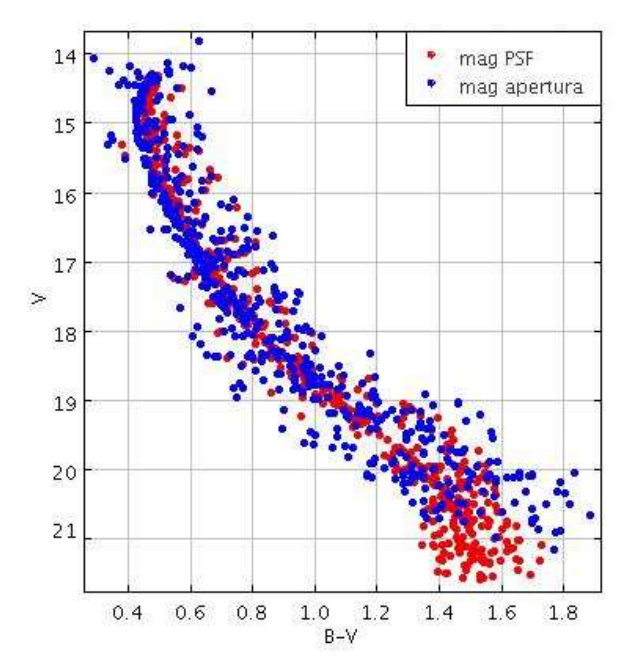


**Fig. 5.** Overlapping of H-R diagrams in Johnson system with the two methods.

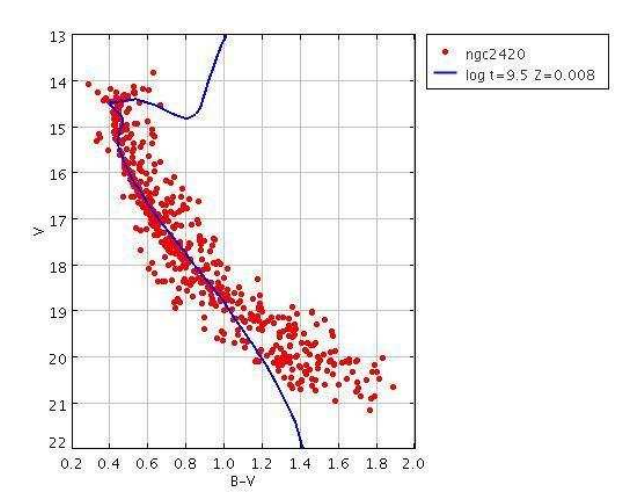


**Fig. 6.** Observed diagram and evolving track with the fitting parameters.

sis, we used isochrones of stars with sub-solar metallicity (0.008). By comparing the experimental curve with theoretical ones, we chose the one that best fitted with our data. The best fit indicated an age of  $10^9.5$  years. To overlap the theoretical curve to the experimental one, we made a translation in vector V (0.02, 11.85). The translation along the X axis (0.02) is the excess of colour that can be also obtained by the difference between B-V measured and the theoretical one, without extinction ( $E_{(BV)} = (BV)(BV)_0$ ); the translation along the Y axis (11.85) is the distance module, that means the difference between the apparent magnitude and the absolute one in the same band ( $V - M_V$ ).

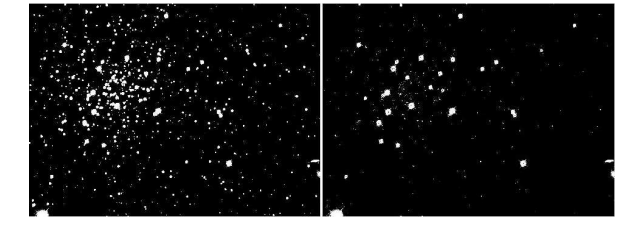


**Fig. 7.** Comparison between the original image and the one without the analyzed stars.

To calculate the distance of the cluster we used the formula of the absolute magnitude in V band

$$M_V = V - 5 \cdot \log d + 5 - A(V) \tag{4}$$

 $M_V$  is the absolute magnitude in V-band; V is the apparent magnitude in V-band; d is the distance of the cluster; A(V) represents the absorption in V-band (due to dust on the galactic plane), which is calculated using the formula  $A(V) = 3 \cdot E_{(B-V)}$ ,  $A(V) = 3 \cdot 0.02$ , so in this case A(V) = 0.06. We solved the equation in  $V - M_V$ , which is the distance module (13.2):

$$V - M_V = 5 \cdot \log d - 5 + A(V)$$
 (5)

The distance is:

$$d = 10^{[(V-M_V)-A(V)+5]/5} = 10^{(11.85-0.06+5)/5} = 10^{3.56} pc(6)$$

The result is 2280 pc, very close to the real one (2299 pc): we have a small error (0.82%).

We can see which stars have been analyzed by the PSF method, i.e. the ones that corresponded to the selection parameters. This is possible thanks to a program that allows to remove the original image of the stars whose magnitude has been calculated, in order to verify if the analysis has considered a large number of stars. If the result is not satisfactory, we can go back to the method of selection to choose less restrictive parameters. The parameter B-V (or the g-r) allows to identify the position of maximum emission and therefore the temperature of the stars in the image. Then we selected three different bands on the abscissa of the H-R diagram that distinguish different temperatures indicated (in order of decreasing temperature) with the colours blue, green and red. This allows to divide the stars in three different ranges of temperature highlighting their hotness also in the original image.

#### 4. Results

The diagrams fit well one another: we can say that both methods are more or less valid. The tail (i.e. the bottom right) of the diagram shows a clearer form in PSF method than in the aperture photometry, and this is because the first one considered better than the second one the small stars; in particular the aperture photometry also "exaggerates" the small stars (i.e. it gives a more

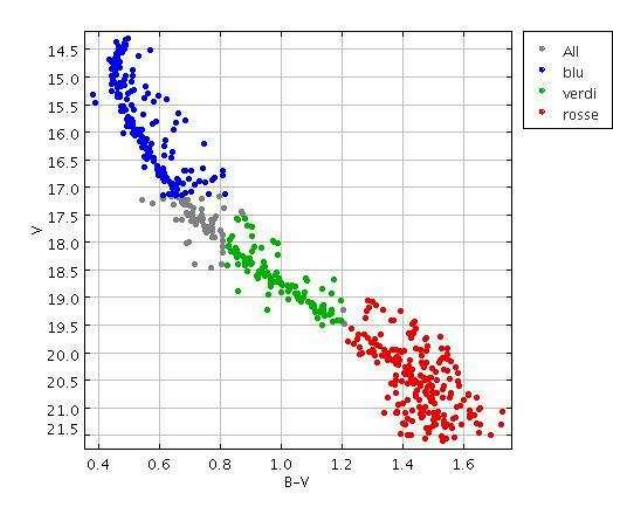


**Fig. 8.** The three temperature ranges.

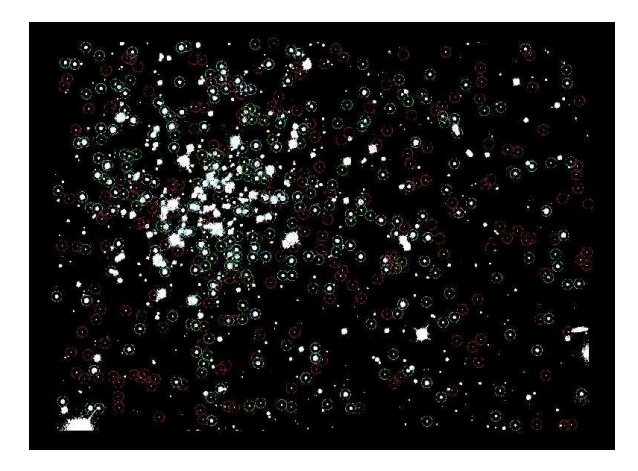


**Fig. 9.** Identification of the stars with different temperatures.

negative magnitude degree) because it does not distinguish very well the background from the actual trace of the star, making it brighter. This does not happen with the PSF, which gives a mathematical model that is able to exclude the background noise. The PSF is generally better to detect stars very close one another than the aperture photometry (which confuses them), so it is the best method of investigation, especially if we are working on a particularly dense groups of stars (such as a globular cluster). In this case the object we were studying was an open cluster, whose stars are not too close to each other, so in our investigation the aperture photometry is also a valid method, although it is worse and less accurate than the PSF, which has the advantage of being able to detect a greater number of stars. In conclusion, even if we proceeded with two different methods we arrived to results largely compatible.

#### References

Il Cielo come Laboratorio, Unità didattica 3: Le magnitudini, i colori e gli spettri delle stelle Il Cielo come Laboratorio, Unità didattica 4: I diagrammia H-R e l'evoluzione delle stelle Gratton, Introduzione all'astrofisica, cap. IX Ammassi e Associazioni, popolazioni stellari, Zanichelli http://www.noao.edu/outreach/press/pr01/pr0107.html http://astro.uchicago.edu/~sleitner/outreach/Pancino et al. 2010, 2010, A&A, 511, 56



## Temperature and radius analysis of 5000 stars

Giacomo Elefante<sup>1</sup>, Gabriele Fonti<sup>2</sup>, Beatrice Marinello<sup>2</sup>, Sofia Verza<sup>1</sup>

<sup>1</sup>Liceo Scientifico *P. Paleocapa*, Rovigo <sup>2</sup>Liceo Classico *Celio*, Rovigo

**Abstract.** In this work we analyzed 5000 stars randomly selected among those in the Galaxy, within a (g-r) color range between -2 and 2. By studying the spectral classification and the initial temperature of 50 of them, we derived the relationship between r magnitude (mag-r) and temperature (T), and subsequently we obtained the temperature distribution of all 5000 stars. The spectral class and temperature were determined, respectively, by comparison with spectra of known stars and with spectra of known black body temperature. Finally, we determined the distance and the radius of the stars and built the R-T diagram.

#### 1. Introduction

The main concept in the spectral classification of stars is that for each chemical composition, the pattern of absorption lines formed in the photosphere of a star depends on the temperature and pressure of the photosphere itself. We can therefore see different spectra in different stars. This diversity comes from the variations in effective temperature of stars because of the different chemical composition and surface pressure. Therefore, in first approximation, the spectral type of a star gives us an estimate of its temperature.

Initially, stars were ranked in alphabetical order according to the decreasing intensity of hydrogen absorption lines. The stars of type A had the most intense lines, the B a little less, etc. It was clear very soon, however, that this system did not order the stars according to their effective temperature. Rearranging spectral types according to decreasing values of the photosphere temperature, we can obtain the following set (Harvard classification):

#### OBAFGKM

This way, we obtain seven spectral classes. Class O includes blue stars, with the highest temperature, class M includes red stars of lower temperature.

Here are the essential characteristics of the classes:

- Class O blue-white stars with the highest temperatures, between 50000K and 25000K.
- Class B blue-white star, about 25000K 12000K.
- Class A white stars with temperature between 12000K and 7500K.
- Class F white stars with temperature between 7500K and 6000K.

- Class G yellow-white star of temperature between 6000K and 5000K.
- Class K Stars "cold", red-orange. The temperature is between 5000K and 3500K.
- Class M Stars even colder, having temperature of about 3000K and then reddish.

Each spectral class is divided into 10 sub-classes numbered from 0 to 9 in decreasing order of T (for ex. O4, A0, ...). The original classification also included the stars R, N, S. These stars, with apparently different spectra, are not cooler than type M, but, as it became clear later, are plentiful of heavy elements.

Physicists usually resort to an ideal body that absorbs all the incident radiation and re-emits thermal radiation, therefore temperature dependent, called black body. For a black body at a given temperature, the distribution of the emitted radiation is just one, whatever the substance that constitutes it.

The emission intensity of a certain temperature black body in the different waveleghts is represented by a graph and it is called the Planck curve. For each temperature exists a different Planck curve: while the temperature gets higher, the maximum of intensity shifts to a shorter wavelength, namely from red to violet.

#### 2. Observational Data

We used images extracted from the public archive of the Sloan Digital Sky Survey (SDSS). SDSS is a project that provides optical images covering more than a quarter of the sky and a tridimensional map containing about one million galaxies and 120000 quasars. SDSS used a 2.5m telescope, at Apache Point in New Mexico. For the photometric survey, five filters have been used; every filter can select only a determined range of the electromagnetic spectrum of visible light. The five filters (u, g, r, i, z) and their average wavelengths are:

u	g	r	i	Z
3551 Å	4686 Å	6165 Å	7481 Å	8931 Å

We selected 5000 stars looking for those that have (g-r) color between -2 and 2. Then we added the 5000 stars in a graph (built with the program Topcat) with (g-r) in abscissa and (r-i) in ordinate, and sorted out 50 stars of magnitude lower than 19 and downloaded their spectra.

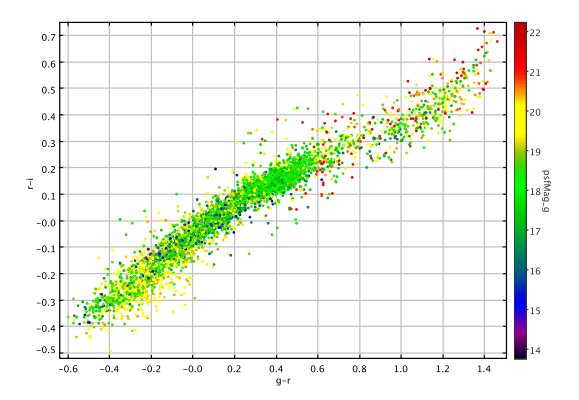


**Fig. 1.** Color-color diagram of the 5000 stars selected from SDSS.

#### 3. Work description

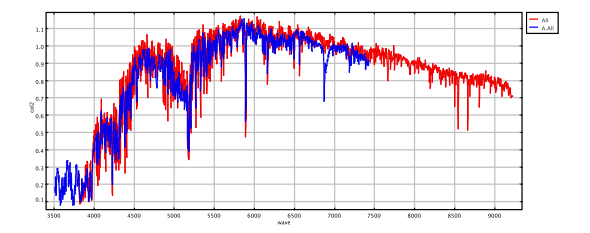
Each stellar spectrum was composed by four stacked spectra; using the IRAF (Image Reduction and Analysis Facility) program we selected only the first of them, namely the one representing only the star's light, without interferences from the light of other stars in the sky around it.

We normalized these spectra dividing by the value at 5500Å, which means imposing the intensity at wavelength 5500Å equal to  $1erg/(cm^2s\text{Å})$  and scaling the other intensities. In this way, our spectra became comparable with standard templates of known stars.

Then, we determined, by comparison, the spectral class of each star: with Topcat we overlapped, on top of the normalized spectra, the spectra of stars of known spectral type. (Remember that each spectral class corresponds to a range of temperatures.)

To determine the temperature of each one of the 50 stars, we searched for the Planck function that best interpolates our observational continuum spectrum.

With all these data (number of stars, temperature, spectral type, Mv - visual magnitude), we wrote a table in Excel, and then we combined our data with those



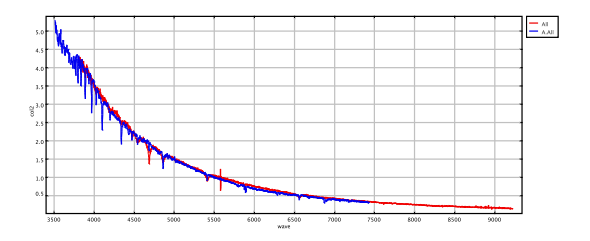


Fig. 2. Example of spectra obtained by IRAF

downloaded from the SDSS database in order to learn all the characteristics about the 50 stars. Following there is an example of the data collected:

StarRef.	S p.Type	Temp	$M_{\nu}$
261	O6-7	140000	-3.7
1736	B0-1.5	45000	-3.0
4410	A2	12500	1.8
1166	A7	10000	2.5
99	F0-3	7150	3.0
1040	F7	6700	3.8
2599	G1	6500	4.6
1973	G4-5	6000	5.0
141	K0-4	4700	6.2
3161	K4	4600	6.5
1532	M1	4000	8.0

Table 1. An example of stellar data obtained

By creating the graph (1/T) vs (g-r), we can see that the color index (g-r) is inversely proportional to temperature (see Fig 3).

The data are linearly interpolated to obtain the equation:

$$m_g = 7320.65/T - 0.739 \tag{1}$$

With this formula, and using the values of  $m_g$  of all the 5000 stars, we were able to obtain the temperature distribution: most of the stars have a temperature between 6000 and 8000K; this happens for classes F, G, and K.

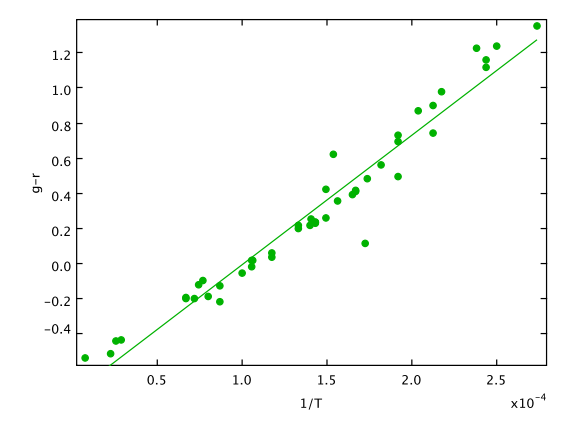


Fig. 3. Graph g-r vs 1/T for the 50 stars of the table above

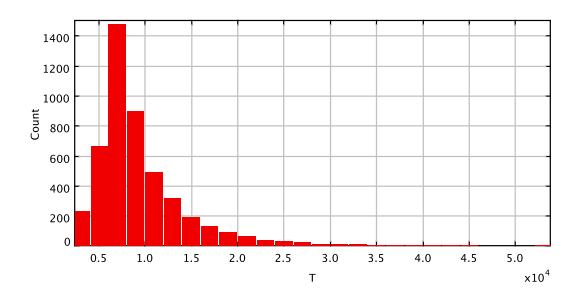


Fig. 4. Temperature distribution of the 5000 stars

#### 3.1. Determining distance

First, we transformed the ugriz magnitudes in Johnsons with the formula:

$$V - g = -0.535(g - r) - 0.016$$
 (2)

we added g to this, to get V (visual or apparent magnitude). Then, we found the distance with the formula:

$$M_v - m_v = 5 - 5Log(d) \tag{3}$$

where  $m_{\nu}$  is the visual magnitude we calculated with the previous formula, and  $M_{\nu}$  is the absolute magnitude, obtained from the HR diagram, assuming that the stars were all on the main sequence.

#### 3.2. Radius of stars

The aim is to calculate the radius using the stars brightness in the V filter:

$$L_{v} = 4R^{2}\sigma T^{4} \tag{4}$$

also,

$$L_{v} = 10^{-0.4} (M_{v} - M_{o}) L_{o} \tag{5}$$

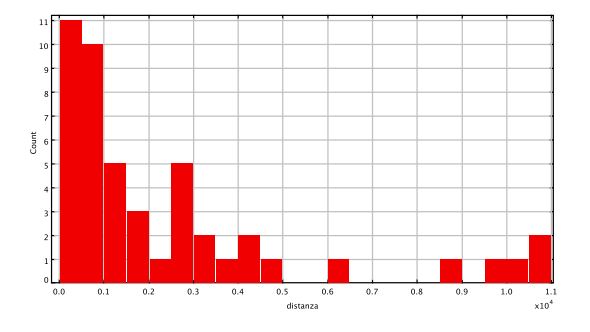


Fig. 5. Distance distribution

where  $M_o = 4.83$  is the solar magnitude,  $L_o = 3.83 \cdot 10^3 erg/sec$  is the solar brightness and  $\sigma = 5.67 \cdot 10^{-5} erg/sec \cdot cm^2 K^4$  is the Stefan-Boltzmann constant.

Building the R-T graph, we expected that with the temperature increase, the radius of the stars also increases (trend similar to the one in HR diagram). The graph, however, did not meet our expectations: infact, the radius increases with growing temperature up to a maximum value, and then it becomes smaller and smaller, even if the temperature keeps growing.

Thus, we analyzed the stars with an anomalous behavior, and discovered that many of them were white dwarfs (result obtained by checking first the SDSS database, and thereafter by noticing that the spectral lines were wider than usual. This depends on the so-called Spark effect, which is typical of white dwarfs). We put these stars in the white dwarfs area of HR diagram (outside the main sequence), determined the proper value of  $M_{\nu}$ , and finally we recalculated the radius.

There were also other anomalous stars, which were not white dwarfs. We checked if they lie on the galactic plane (in that case we should have considered the phenomenon of light extinction due to galactic dust). All the stars were outside the galactic plane. By checking the SDSS database, we found that those stars belong to the horizontal branch. We recalculated magnitude and radius as well for these stars. The R-T graph appears to be correct as in Fig.6.

Finally, we found that the main sequence was almost entirely lacking of O-B-A stars: all the hottest selected stars were white dwarfs and therefore they were rejected!

#### 4. Results

With our work, we tried to derive the relationship between the temperature and the radius of the stars. We expected to find that the radius increases when the temperature raises up; instead, we obtained a lot of errors, but we understood they were due to the fact that not all the selected stars belonged to the Main Sequence: some were, infact, white dwarfs and others belonging to the

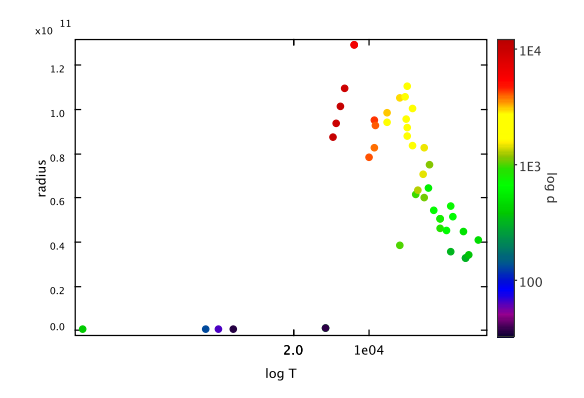


Fig. 6. Temperature-radius relation of our stars

Horizontal Branch. Having eliminated from the calculation these stars, and having left only those of the main sequence, we obtained the expected results.

The reason of having found so many white dwarfs is probably due to the initial choice of stars with color index between -2 and 2, which is very bright. It would have been interesting, but not possible for time limits, to change the initial parameters of selection and try again with different samples.



### Relation between spectral lines and temperature of a star

Matteo Gallone, Andrea Gastaldi, Matteo Lionello, Elettra Sommavilla, Sebastiano Verde

Liceo Scientifico G. B. Benedetti, Venezia

**Abstract.** The purpose of our work was to verify the relation between the intensity of the absorption lines in some stellar spectra and their temperatures. The examined lines are CaK, CaH, Mg, Na,  $H_{\alpha}$  and CaII, measured on a sample of about 50 stars.

#### 1. Introduction

The analysis of a stellar spectrum provides plenty of information about the physical nature of stars (temperature, atmospheric composition, orbital speed, etc.), which are classified in 7 major spectral classes in descending order of temperature: O, B, A, F, G, K, M.

A stellar spectrum is characterized by a spectral continuum - whose intensity can be approximated with the Planck function - interspersed with the absorption lines typical of the various chemical elements that compose the star's atmosphere.

The hot gas on the star's surface (photosphere) behaves as a white light source emitting a continuous spectrum. The presence of atmospheric gas with a lower temperature than the surface gas causes the absorption of electromagnetic radiation at certain wavelengths, generating the absorption lines.

The intensity of these lines does not depend solely on the quantity of the chemical elements composing the star (nowadays we know that stars are all similar in composition), but depends also on the photosphere temperature and the electronic pressure. Different elements or elements with electrons in different energy levels require different energies to be ionized. For instance, at high temperatures atoms are so excited that their electrons jump to levels higher than the ground one and they are easily ionized; whereas at low temperatures the electrons jump readily down to the ground level. This is the reason why the Balmer series of Hydrogen (lines caused by the electron transitions connected with the second energetic level of the hydrogen atom) is not visible in the M spectral class spectrum.

Temperature significantly affects the presence and the intensity of the lines, causing different trends according to the considered element.

Our work is based precisely on the verification of this phenomenon, describing the trends of some se-

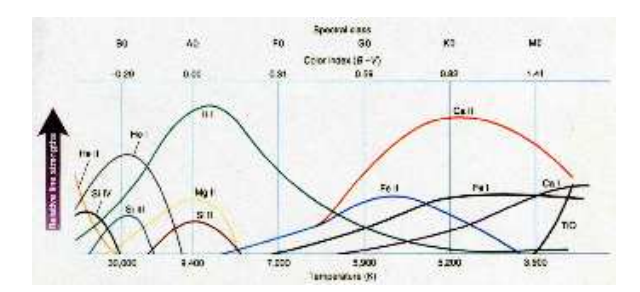


**Fig. 1.** Expected relation between intensity of absorption lines and temperature.

lected spectral absorption lines in relation to temperature variations (see fig.1).

#### 2. Observational Data

For our work, we used data taken from the online archive of the Sloan Digital Sky Survey. The SDSS used a dedicated 2.5 meters telescope at the Apache Point Observatory, New Mexico, equipped with two powerful special-purpose instruments. The 120 megapixel camera imaged 1.5 square degrees of sky at a time.

The spectra used to study the lines and to calculate the temperature were selected from a sample of 5000 stars, whose colour index g-r is included between -2 and 2. Using the software TOPCAT, we displayed the star data in a colour graph, with g-r indexes in abscissa and r-i indexes in ordinate.

From the densest zone of the graph we chose 54 stars with increasing g-r indexes. We assumed that higher g-r readings corresponded to lower temperature readings. We listed the selected stars in a TOPCAT table, we downloaded their spectra from the online archive and used the program IRAF to extract the right files.

#### 3. Work Description

It was necessary to divide the work in two groups: the first group measured the equivalent width of some spectral absorption lines, the second group sought to approximate the temperature of the selected stars with the Planck function.

The equivalent width (EW) of a spectral absorption line is defined as the width that the line would have when absorbing all the photons in an interval  $\Delta\lambda$  and no other photons outside this interval, thereby producing the same energy absorption as the line considered (see fig. 2). Therefore the EW quantitatively measures the energy content of the line in units of length (Å).

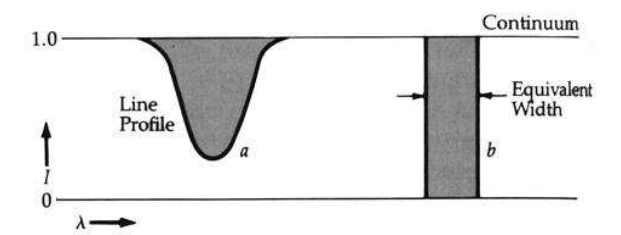


**Fig. 2.** The equivalent width is equal to the base of the rectangle whose area equals that of the spectral line

The lines selected for our work were:

Line	Wavelength
CaK	3934 Å
CaH	3969 Å
Mg	5175 Å
Na	5891 Å
$H_{\alpha}$	6562 Å
CaII	8498 Å- 8542 Å- 8662 Å

First of all we had to identify them in the extracted spectra. IRAF software allows to display the spectrum in a graph and to work on it interactively through the task *splot*. The zoom function ('a' key) highlights the portion of the spectrum around the line being measured. Measurements were carried out with the integration function ('e' key) that calculated the spectral area described by the line and output the value of the equivalent width in length units. We entered those values in the table of the selected stars.

The main difficulty, due to the loud background noise in many spectra, was to estimate accurately where the line began and ended. So we often preferred to do more than one measurement and to take a mean value; however we did not consider the percentage of error. As some lines were weak, hardly distinguishable from the continuous spectral trend, or totally absent, it was impossible to estimate their exact equivalent width value.

The spectra were converted to a text format to be read with TOPCAT and normalized at the wavelength

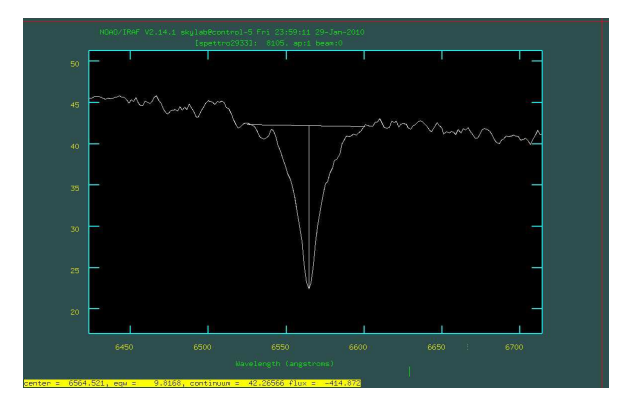


**Fig. 3.** Given the base of the line the program outputs the equivalent width.

of 5500 Å. Normalizing means assigning arbitrarily the value of 1 erg·cm $^{-2}$ s $^{-1}$ Å $^{-1}$  to the intensity of a certain wavelength. To avoid mistakes due to background noise we chose the mean value of the intensities between 5450 Å and 5550 Å as value of the intensity at 5500 Å.

To estimate the temperature we entered in the same graph the stellar spectrum and the Planck function normalized at 5500 Å given by:

$$U(\lambda, T) = \frac{5500^5}{\lambda^5} \frac{e^{\frac{c}{55007}} - 1}{e^{\frac{c}{\lambda T}} - 1}$$

We entered different temperature values in the Planck function, comparing the black body graph with the stellar one. We did so several times to get the best approximation as in fig 4.

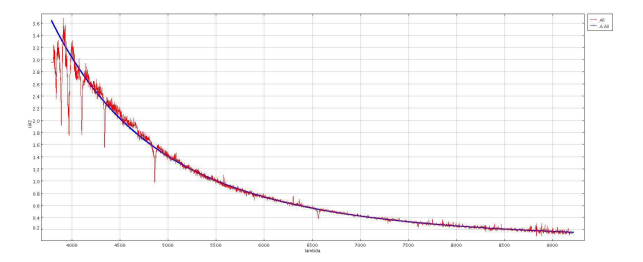


**Fig. 4.** Approximation of a stellar spectrum with Planck function

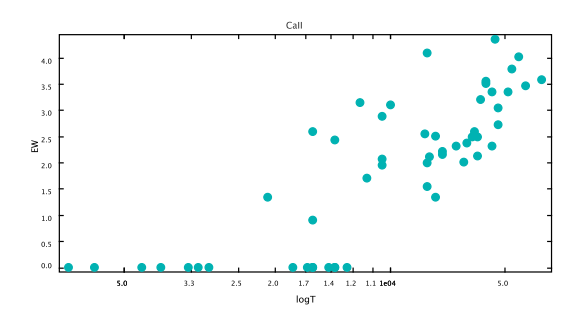
While approximating the spectra with the Planck function, we noticed that it was very hard to approximate at low wavelengths. And if we managed to approximate correctly the spectrum at low wavelengths, the Planck function did not approximate it at high and medium wavelengths. We attributed this to atmospheric absorption and regarded the functions that approximated the spectrum at high and medium wavelengths as more reliable. For this reason the temperatures of the hottest stars are more uncertain than the others.

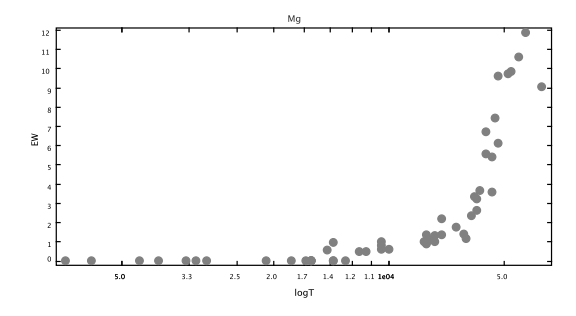
We carried out this procedure for all the stars in the sample, entering the temperature results in the table previously produced with the EW values. In the following table there is an example of the data we obtained: only few stars of different temperatures and some lines are presented.

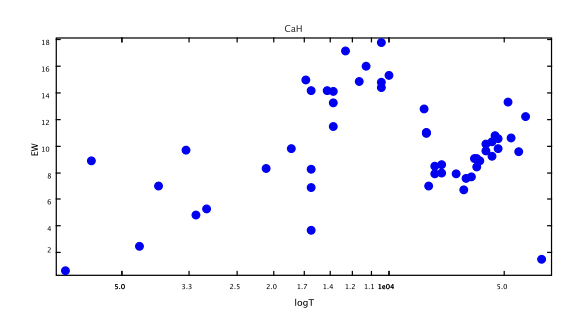
Star	Temp	CaH	Na	Н	CaII
3297	4400	12.15	6.85	1.01	3.46
1326	6000	8.9857	1.5407	3.833	2.5782
971	10000	15.2466	0.5122	9.9261	3.0867
4115	14000	11.38	0.81	7.14	2.43
1041	21000	8.2682	-	6.0546	1.329
3047	45000	2.40	0.08	3.44	-
865	70000	0.6242	-	3.2241	-

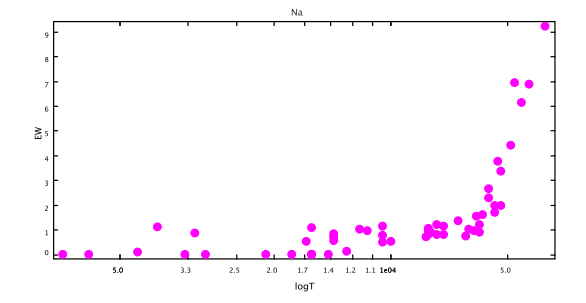
#### 4. Results

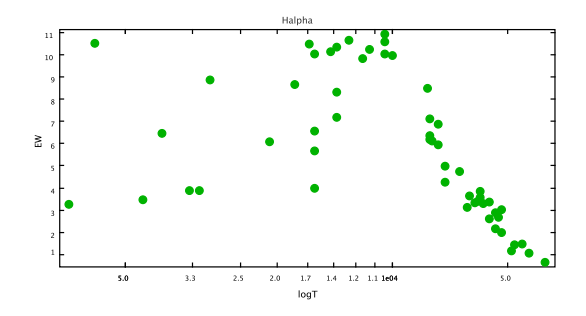
Trough the temperature/equivalent width table we obtained the following graphs:











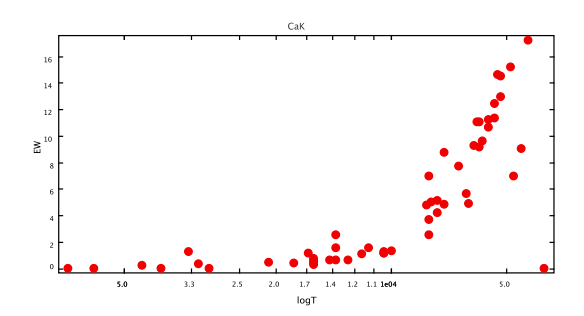


**Fig. 5.** EW/T relation for different elements. Each dot represents a star.

As can be seen, the distribution is not uniform in the graphs. It is possible to observe (often very clearly) a specific trend. Some trends are very different from the expected ones. The clearest case is CaII, where two peaks can be observed. Probably this is caused by the presence of absorption lines of other elements at nearly the same wavelengths.

But all-in-all our work verifies the relation between the intensity of the absorption lines in certain stellar spectra and their temperature.



# Study of the stellar population of the galaxies NGC3351, NGC660, NGC2903, NGC3310

Anna Baldin<sup>1</sup>, Elisa Dughiero<sup>1</sup>, Andrea Marangon<sup>2</sup>, Gaia Naccari<sup>1</sup>, Lorenzo Voltolina <sup>2</sup>

<sup>1</sup>Liceo *G. Veronese*, sez. Classico, Chioggia <sup>2</sup>Liceo *G. Veronese*, sez. Scientifico Brocca, Chioggia

**Abstract.** Our work proposes to study the stellar population in four galaxies through the analysis of their electromagnetic spectrum by means of the spectroscopic observations of NGC2903, NGC3310, NGC660, NGC3351.

#### 1. Introduction

The basis of astronomy is light. The dual nature of light requires two types of observation: light as a wave is measured with spectrographs, which allow to rebuild the characteristic electromagnetic spectrum; light as a particle, in its units, that is photons, is observed with the modern CCD, digital sensors of photons.

Galaxies are sources of electromagnetic radiation: this can be studied in order to determine their physical properties (redshift, stellar population and flux). We reproduced the spectral continuum combining three types of stars belonging to three different groups:

- 1. young stars (O-B);
- 2. middle stars (A-F-G);
- 3. old stars (K-M);

Object	NGC2903
Right Ascension	9h32m10.1s
Declination	+21d30m03s
Constellation	Leo

Object	NGC3310
Right Ascension	10h38m45.86s
Declination	+53d30m12s
Constellation	Ursa Major

Object	NGC660
Right Ascension	1h42m
Declination	+13d23m64.00s
Constellation	Pisces

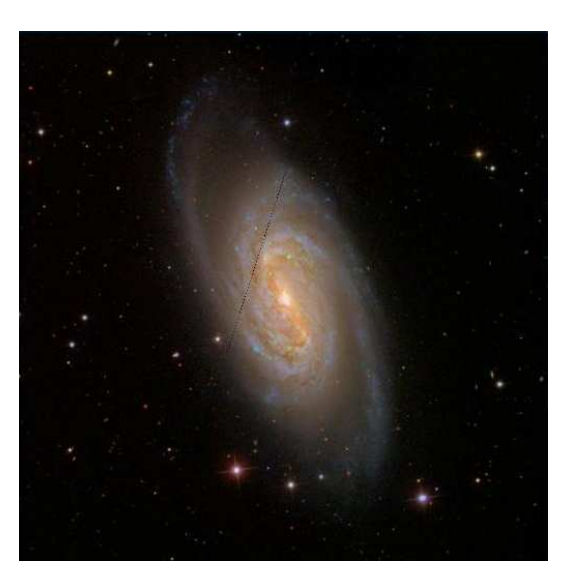


Fig. 1. Galaxy NGC2903

Object	NGC3351
Right Ascension	10h43m57.70s
Declination	11d42m13.00s
Constellation	Leo

#### 2. Observational Data

The spectroscopic observations of the objects were carried out with the Boller & Chivens spectrograph mounted at the Cassegrain focus of the 120 cm telescope of the Asiago Astrophysical Observatory. The galaxies' spectra were corrected for bias, using the overscan section, and flat field. Then the spectra were

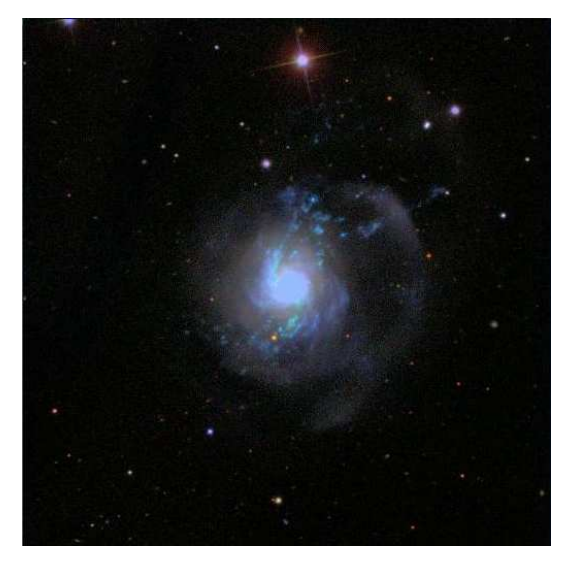


Fig. 2. Galaxy NGC3310



Fig. 3. Galaxy NGC660

calibrated in wavelength and flux and extracted. The galaxies' spectra need to be also corrected for redshift. For the reduction of the spectra and for the measures we used IRAF.

#### 3. Work description

Using the task IMPLOT, we plotted graphs showing the distribution of light of the galaxies along the slit. We divided each spectrum into two parts, obtaining two graphs for each galaxy. We calculated the redshift (z) of the galaxies subtracting from the measured value of the  $H\alpha$  wavelength ( $\lambda_1$ ) the theoretical one  $\lambda_0$  and dividing by  $\lambda_0$ . The following step was to bring back the spectrum to redshift z=0 in order to reproduce it with the best approximation through the linear combination of spectra of known spectral class stars.



Fig. 4. Galaxy NGC3351

We also corrected the values for absorption. There were  $H\beta$  and  $H\alpha$  emission lines among the absorption bands. We measured the flux of  $H\alpha$  and the flux of  $H\beta$ . The results were inserted in the following formula:

$$A(V) = \frac{\log\left(\frac{I(H\alpha)}{I(H\beta)} / \frac{F(H\alpha)}{F(H\beta)}\right)}{-0.1386}$$
(1)

Then we found the A(V) of each part of the spectrum. We faced the extinction problem: we gave IRAF the values of A(V), so that it could correct our spectra, but the correction could be overvalued. Indeed, we used the values obtained from gas to correct the stellar component, but if the ionized gas and the stars are not in the same place, the gas extinction can be overestimated.

Then, we normalized the spectra at 5500 Å, by dividing the spectra for the value of the flux at 5500Å.

Every stellar spectrum was multiplied by a coefficient (0 < c < 1) which represents the percentage of the contribution in light of this particular stellar population (the sum of the coefficients must give one), then the spectra were summed in linear combination. We selected main sequence stars, after various attempts, that represent old, middle and young stars, and so we deduced the percentage of the light shed by each of these classes, whose sum gives the 100% of the light coming from galaxies.

	NGC3351a	NGC3351b	NGC660
$F(H\alpha)$	$8.65 \cdot 10^{-14}$	$7.00 \cdot 10^{-14}$	$2.74 \cdot 10^{-14}$
$F(H\beta)$	$1.22 \cdot 10^{-14}$	$71.05 \cdot 10^{-14}$	$3.74 \cdot 10^{-14}$
A(v)	2.8448	2.6515	2.9473

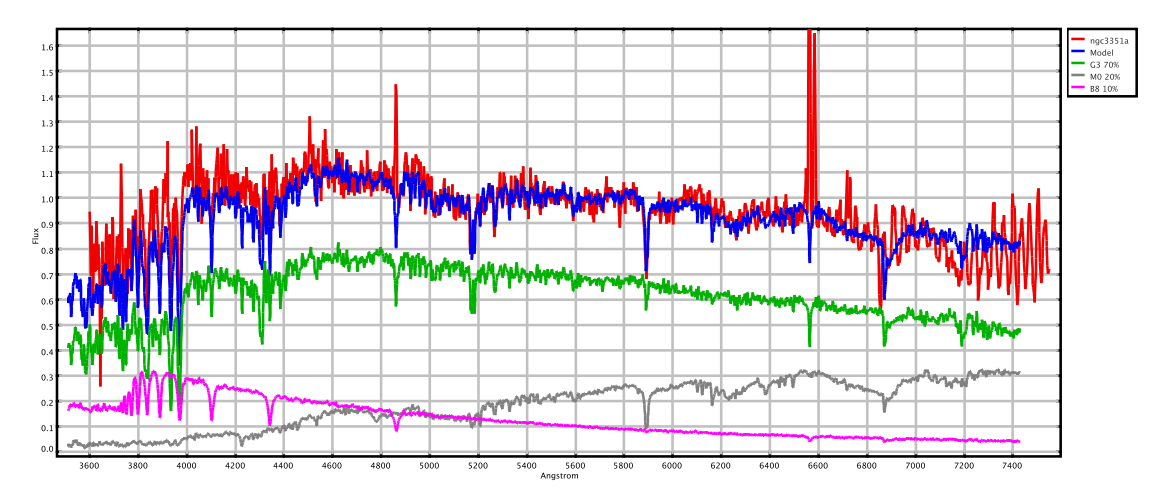


Fig. 5. Stellar population synthesis: NGC3351a

Galaxy	$\lambda(H\alpha)$	Z	$H\alpha/H\beta$	A(V)
NGC2903a	6576	$1.9 \cdot 10^{-3}$	8.4	3.376
NGC2903a	6573	$1.5 \cdot 10^{-3}$	5.2	1.8732
NGC2903b	6578	$2.4 \cdot 10^{-3}$	3.61	0.73
NGC2903c	6585	$3.3 \cdot 10^{-3}$	3.43	0.56

#### 4. Results

Using the linear combination of stellar spectra to match the absorption spectrum of the galaxy, the percentage of different stellar populations in the galaxies could be deduced. The stars are concentrated in the nucleus, in the arms and in a halo where there are globular clusters orbiting around the galaxy. Stars are divided in two populations, an older one (Population II) is found mainly in the bulge and in the halo and a younger one (population I) concentrated mostly in the arms.

The spectrum of NGC3351 was divided into two parts to facilitate the process of detecting the stellar population. In NGC3351a (see fig.5), there is a high presence of old, cold stars and a small percentage of young stars. Indeed, G and M-type stars occupy 90% of the population, the remaining 10% are young stars of type B, with temperatures between 10000 K and 30000 K. These stars, usually, reveal a process of star formation and they are, in most cases, in the arms of spiral galaxies. In the second part of galaxy NGC3351 (see fig.6), there is no presence of young stars: 75% of the stellar population is represented by G-type stars, the remaining 25% are M-type stars. This is due to the fact that the spectrum of spiral arms, with the possible presence of young stars and star formation processes, is found only in Part A of the total spectrum of galaxy NGC3351.

We had to divide the spectrum in two parts also in the case of NGC2903. In NGC2903a (see fig.7) there are mainly young stars: A-type stars represent 70% of the population and only 30% are M-type stars

whose surface temperature is near 2500 K. The second part of the galaxy (NGC2903b, see fig.8) is characterized for 60% by young hot A-type stars with temperatures between 7500 K and 10000 K, and for 40% by colder, older stars (K-type). Barred spiral galaxies like NGC2903 have a large amount of gas mixed with dust from which new stars form continuously.

In galaxy NGC3310 (see fig.9 and fig.10) the stellar population is young (B type stars with temperatures between 10500 - 30000 K) for 60%. The other percentages are given by G and M-type stars: 10% of G-type and 30% of M-type in the first part of the galaxy; 30% of G-type and 10% of M-type in the second one.

In galaxy NGC660 (see fig.11) the stellar population is predominantly of type G (80%), i.e., stars with temperatures between 5500 and 6000 K. The other percentage contributions in the stellar population are given by M and K type stars, both older and colder (from 4000 to 2000 K) and even of lower mass.

#### References

Wikipedia.en nasaimages.org cosmo.nyu.org xoomer.virgilio.it/waphil/popolazioni%20stellari.htm

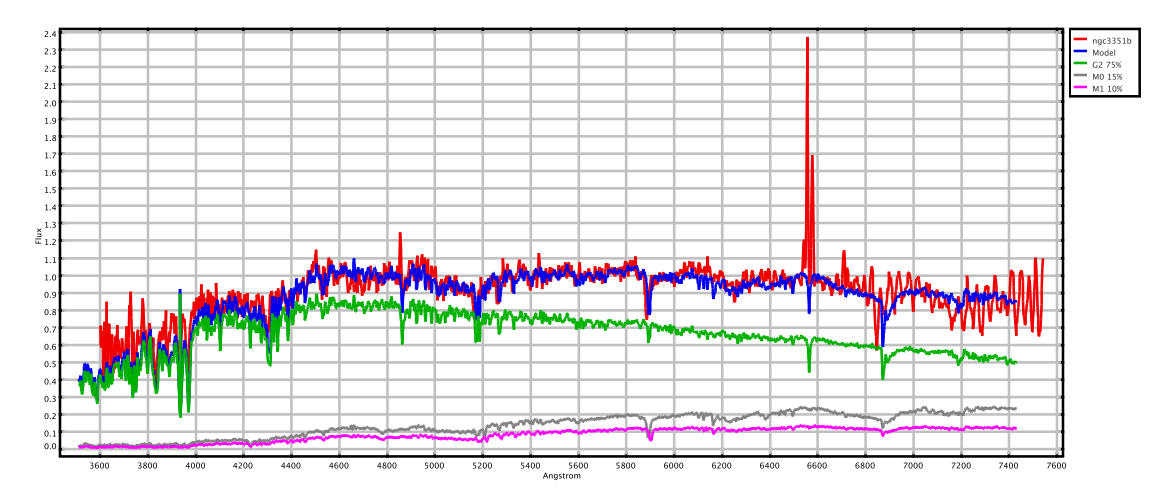


Fig. 6. Stellar population synthesis: NGC3351b

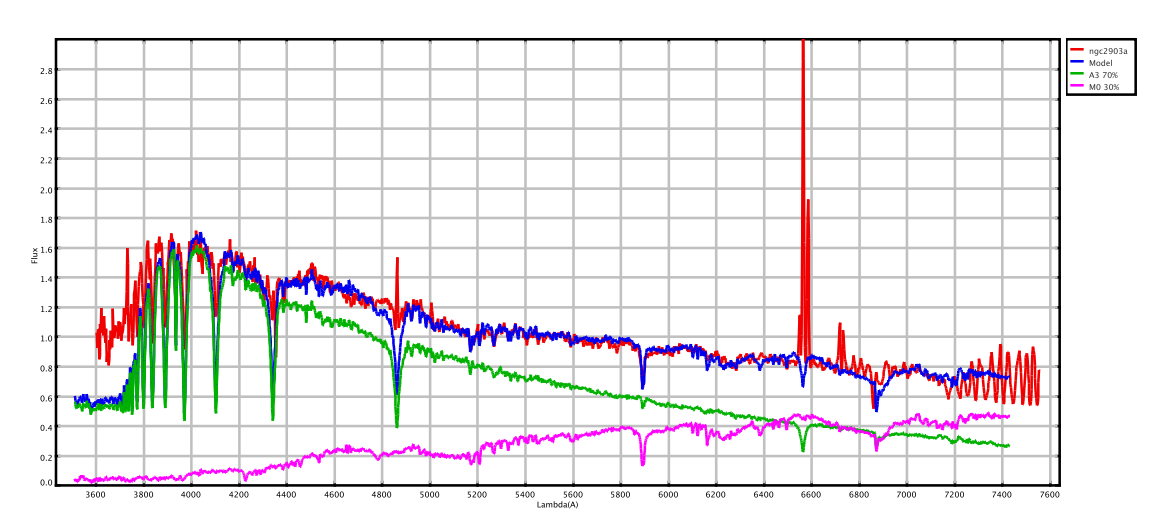


Fig. 7. Stellar population synthesis: NGC2903a

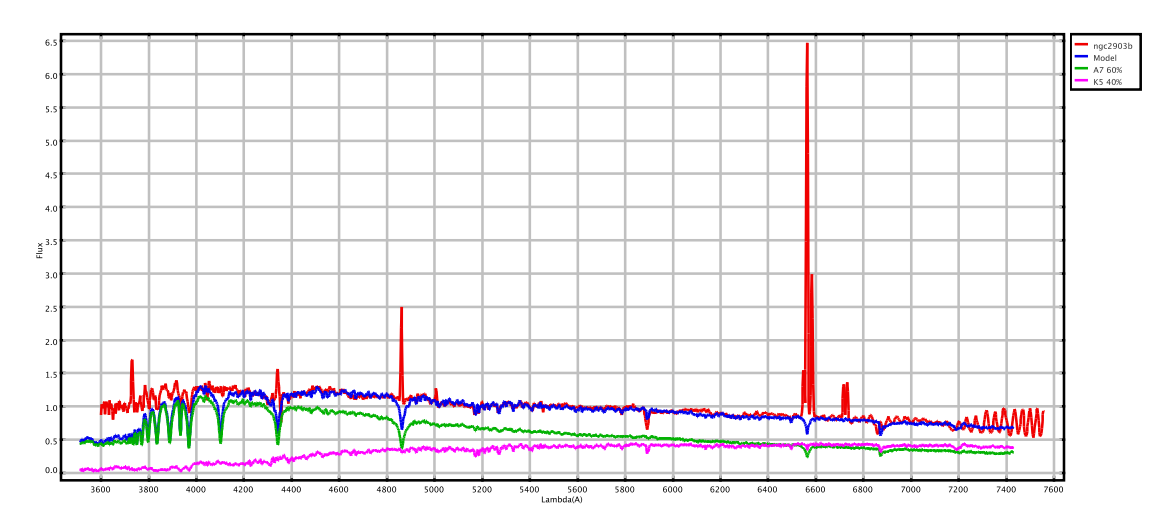


Fig. 8. Stellar population synthesis: NGC2903b

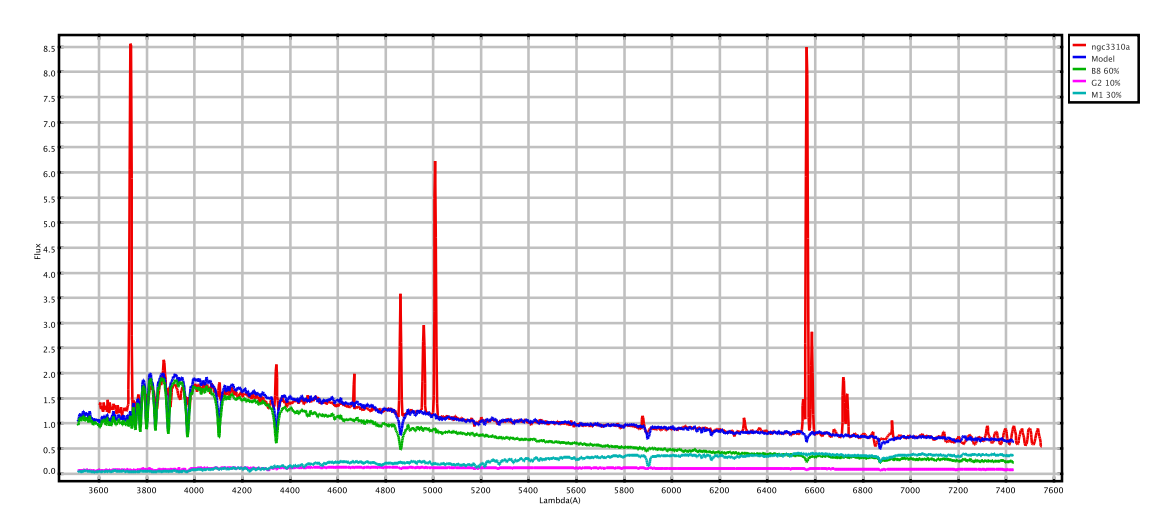


Fig. 9. Stellar population synthesis: NGC3310a

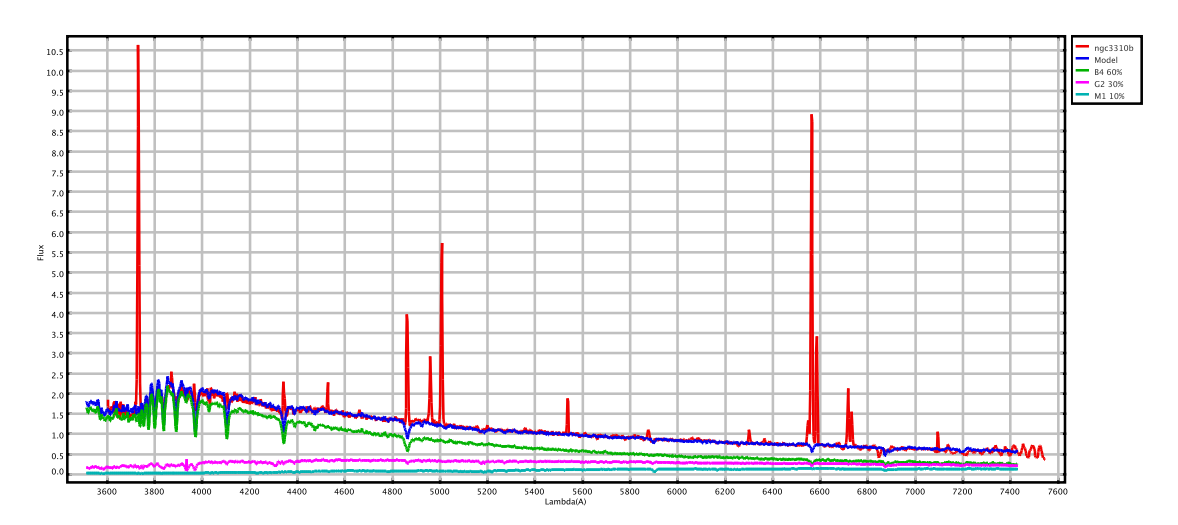


Fig. 10. Stellar population synthesis: NGC3310b

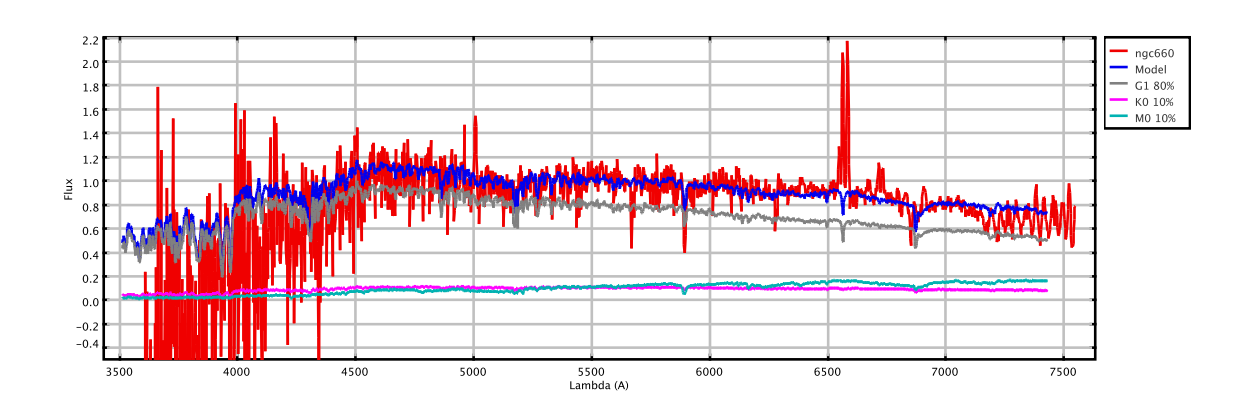


Fig. 11. Stellar population synthesis: NGC660



## Spectroscopy of NGC 6720

Martina Ghirardo, Laura Michelon, Carmelo Puliatti

Liceo scientifico G. Marconi

**Abstract.** The aim of this work was to analyse the spectrum of Planetary Nebula M57 (NGC 6720), in order to achieve some information about electron temperature and density and chemical abundances of nitrogen and oxygen. Eight regions were considered, one of them containing the central star. Approximate electron temperature and density and chemical abundances were obtained studying the emission lines of specific elements: [SII], [OII], [OIII], [ArIV].

#### 1. Introduction

A planetary nebula represents the final phase in the life of stars with an initial mass within 0.8 and 8 solar masses. During the period of instability (Asymptotic giant branch), the core of these stars continues to contract and heat up, becoming gradually a white dwarf, while the outer layers are ejected, in an expanding shell that cools down moving away from the star. The process of expansion and the gradual cooling of the nebula go on for tens of thousands years. These outer layers form nebulae with a spherical-like shape, also known as planetary nebulae. This name is due to the similarity between the first images obtained from the observation of this objects and the ones of solar giant planets. There are different categories of nebulae: emission, reflection and dark nebulae. We studied the first type. In figure (1) there is an image of M57 obtained with the Hubble Space Telescope. Each colour reveals the presence of a particular chemical element which has been ionized by the central star, for example red is the ionized nitrogen, green the ionized oxygen and blue is hot helium. The object we studied is called with different names: Ring Nebula, M57 or NGC 6720, and is also known as "Ring of smoke". It is located in the Lyra constellation, between Sheliak and Sulaphat ( $\beta$  and  $\gamma$  Lyrae), at a distance of 2300 light-years (ly) and is about 1 ly in diameter. This object is quite easy to observe and it is considered the prototype of planetary nebulae. Its structure is still a debated question: Minkowski and Osterbock (1960) have modelled this object with a toroidal structure surrounded by a thin spherical shell as outer envelope, whereas Louise (1978) do not confirm a spherical shell model for the inner ring, as originally suggested by John Herschel.

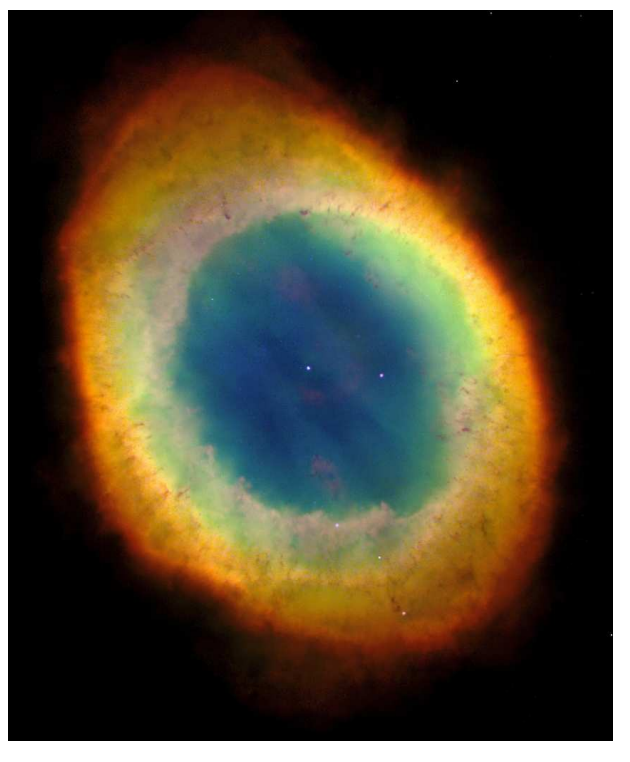


**Fig. 1.** An image of the Ring Nebula taken with the Hubble Space Telescope.

#### 2. Observational Data

Our study is based on observations made on July 27th 2007 using the 122cm telescope of the Asiago Astrophysical Observatory; in particular we analysed the long-slit spectrum of M57.

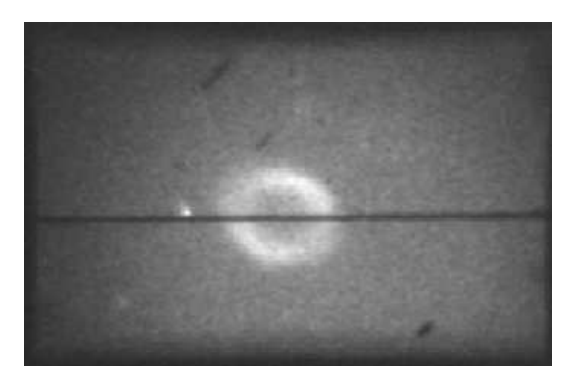


**Fig. 2.** An acquisition image of the Ring Nebula: the black rectangle indicates the position of the slit.



**Fig. 3.** The longslit spectrum of the Ring nebula taken at the 122 cm telescope of the Asiago Astrophysical Observatory.

#### 3. Work Description

To begin, the spectrum was divided in 8 regions. Each region measures 15 pixels (where 1 pixel corresponds to 0.6" and 1" is 3.6 parsec). Then, we identified the central region, C, where we have the spectral contribution from the central star and the nearest surrounding material, and 7 regions numbered progressively in order of growing distance from the core (A4, A3, A2, A1, B1, B2, B3). Afterwards we made an accurate analysis of the spectrum of each region by calculating the fluxes of the emission lines of significant elements. The process of data analysis was done using IRAF (Image Reduction and Analysis Facility) tasks.

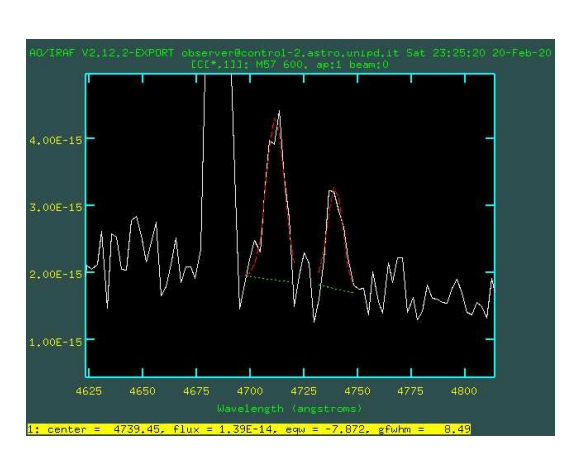


Fig. 4. An example of the analysis of the spectrum with IRAF.

Once completed the determination of the fluxes, the next step was their correction for extinction. This procedure consists in removing the reddening effect due to light absorption caused by the interstellar medium. For each region, we calculated the ratio between the flux of the  ${\rm H}\alpha$  line and the flux of the  ${\rm H}\beta$  line and we compared this value with the theoretical one, obtained from the Balmer decremet that is equal to 2.86. From this comparison, by applying Cardelli, Clayton and Mathis law (Cardelli, Clayton & Mathis, 1989), we derived A(V), the absorption in V-band. With these values we corrected for extinction each measured flux. All the calculations concerning this part of the work were made using TOPCAT.

Corrected fluxes of the emission lines – I					
Wavelength(Å)	A3	A2	C		
3727 [OII]	4.1474E-12	9.1382E-13	4.5103E-13		
4861 Hβ	8.9582E-13	6.5328E-13	4.9771E-13		
4959 [OIII]	3.0969E-12	2.5456E-12	1.7502E-12		
5007 [OIII]	9.1645E-12	7.5729E-12	4.5079E-11		
4685 HeII	1.3866E-13	2.581E-13	4.1466E-13		
5876 HeI	1.5759E-13	7.6109E-14	4.5079E-14		
6548 NII	1.2531E-12	2.35E-13	8.4509E-14		
6583 NII	4.2037E-12	8.6915E-13	3.0547E-13		

Corrected fluxes of the emission lines – II				
Wavelength(Å)	B1	B2	В3	
3727 [OII]	1.4747E-12	2.7206E-12	4.0498E-12	
4861 Hβ	1.5426E-12	1.0122E-12	5.2164E-13	
4959 [OIII]	5.7543E-12	4.0022E-12	1.4753E-12	
5007 [OIII]	1.6717E-11	1.1712E-11	4.3533E-12	
4685 HeII	6.3121E-12	3.5195E-13	2.4984E-14	
5876 HeI	1.4710E-13	1.3345E-13	9.3422E-14	
6548 NII	1.8021E-13	7.3654E-13	1.1123E-12	
6583 NII	6.3502E-13	2.2898E-12	3.6653E-12	

Using the corrected fluxes, we estimated the values of electron density and temperature at low and high ionization in each region, with the IRAF task TEMDEN, which calculates the temperature (for an assumed density) or density (for an assumed temperature) from extinction corrected emission lines ratios. In particular, we used the [SII] and [OII] forbidden lines to determine the density and temperature of low ionization regions, whereas we used the [ArIV] and [OIII] lines in high ionization regions.

Density and temperature					
Region	A3	A2	C		
<sub>e</sub> [SII]	820	660	400		
<sub>e</sub> [OII]	11470	11640	13824		
[ArIV]	820	1310	400		

12050

13824

10660

Density and temperature

Bensity and temperature					
Region	B1	B2	В3		
$N_e$ [SII]	300	900	650		
$T_e$ [OII]	15730	10950	10270		
N <sub>e</sub> [ArIV]	300	2800	650		
$T_e$ [OIII]	13160	11140	11060		

In some regions (A1 and A4) it was not possible to analyse some significant lines because of their very low intensity, which has prevented us from discerning them from the background radiation. The data was elaborated into the following graphs using EXCEL:

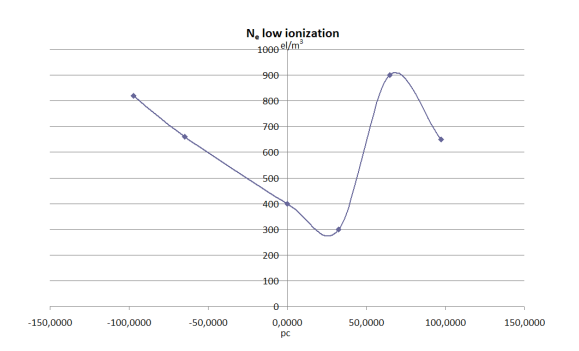


**Fig. 5.** Radial profile of the electronic density for low ionization gas.

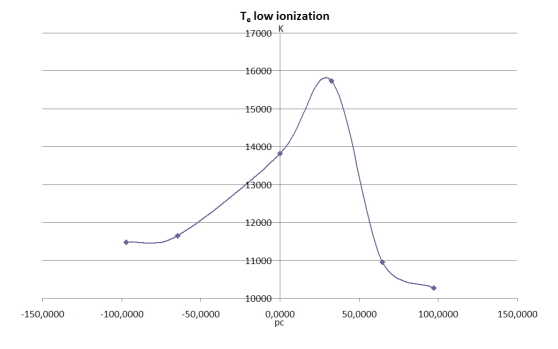


**Fig. 6.** Radial profile of the electronic temperature for low ionization gas.

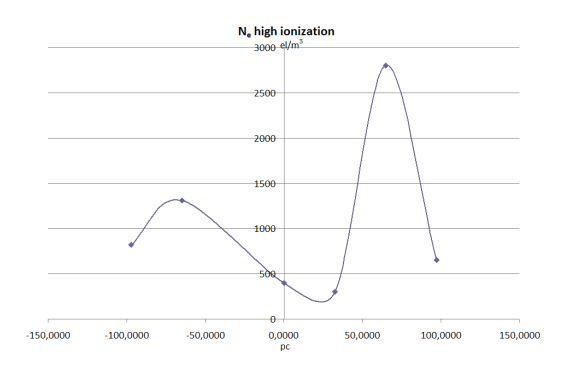


**Fig. 7.** Radial profile of the electronic density for high ionization gas.

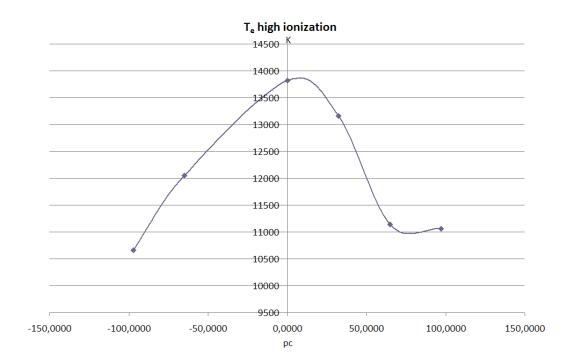


**Fig. 8.** Radial profile of the electronic temperature for high ionization gas.

These results are not far from those obtained by Guerrero et al. (1997). It can be seen that the electron temperature declines towards the edge of the ring, whereas the density varies: it increases from the central region to the ring, then drops off in the halos.

Finally, chemical abundances of nitrogen and oxygen in each region were determined, in order to define the distribution of these two elements within the nebula, because of their importance for the definition of physical phenomena which take place in it. We have applied these formulas:

 for the abundance of oxygen (which appears in 3 different forms: OI, OII and OIII)

$$12 + \log\left(\frac{\text{OI}}{\text{HI}}\right) = \log\left(\frac{I_{3727}}{I_{H\beta}}\right) + 5.89 + \frac{1.676}{t_2} - 0.40\log(t_2) + \log(1 + 1.35x)$$
(1)

$$12 + \log\left(\frac{\text{OII}}{\text{HI}}\right) = \log\left(\frac{I_{4959} + I_{5007}}{I_{H\beta}}\right) + 6.174 + \frac{1.251}{t}$$
$$-0.55\log(t_2) + \log(t)$$
(2)

$$\left(\frac{\text{OIII}}{\text{OII} + \text{OI}}\right) = 0.111 \cdot t^{-0.13} \left(\frac{I_{4686}}{I_{5876}}\right)$$
 (3)

where:

$$t = \frac{T_e[OIII]}{10^4 K} \tag{4}$$

$$t_2 = T_e[OII] = 0.243 + t(1.031 - 0.184 \cdot t)$$
 (5)

$$x = \frac{N_e}{\sqrt{t_2} \cdot 10^4} \tag{6}$$

The abundance of oxygen is the result of the ratio:

$$\frac{O}{H} = \frac{OI + OII + OIII}{HI} \tag{7}$$

- for the abundance of nitrogen:

$$\log\left(\frac{\text{OI}}{\text{NI}}\right) = \log\left(\frac{I_{3727}}{I_{6548} + I_{6583}}\right) - 0.307 + \frac{0.726}{t_2} + 0.02\log t_2 + \log\frac{1 + 1.35x}{1 + 0.116x}$$
(8)

The abundance of nitrogen is given by the ratio:

$$\frac{N}{H} = \frac{O}{OI} \cdot \frac{NI}{HI} \tag{9}$$

We obtained the following results:

1		A3	A2	С
	O/H	4.2429E-04	3.5130E-04	2.5085E-03
	N/H	1.9939E-04	1.5390E-04	8.4798E-04

	B1	B2	В3
O/H	9.9553E-04	4.3545E-04	3.6371E-04
N/H	2.1848E-04	1.7375E-04	1.5774E-04

From these data we can establish connections between the variation of oxygen and nitrogen abundances and the distance from the core of the regions where we found these elements:

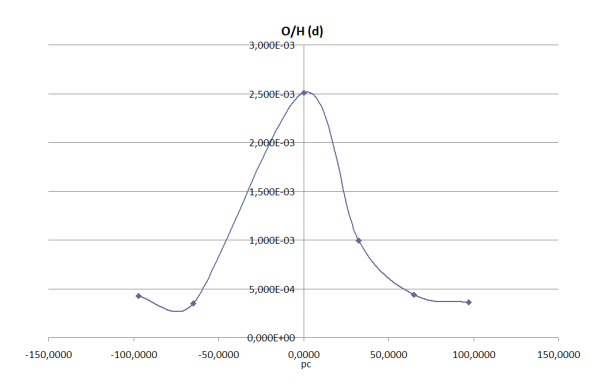


Fig. 9. Radial profile of the oxygen abundance.

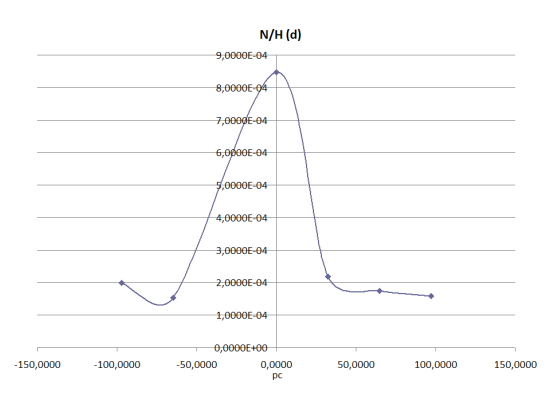


Fig. 10. Radial profile of the nitrogen abundance.

#### 4. Results

Consequently to the analysis, we drew the following conclusions. In agreement with the estimations based on theoretical data (O'Dell et al., 2006), the electron temperature shows the highest value in the central region and gradually decreases towards the external regions. Electron density also corresponds to the results we expected: the highest values were found in the outermost regions, where actually the gases ejected at very high speed are thwarted by the interstellar medium. From the chemical point of view, a symmetric distribution of nitrogen and oxygen was detected, as expected from theoretical models (Greenhouse and Haryward 1988).

#### References

Greenhouse, Hayward: 1988, H<sub>2</sub> and HI emission line imaging of the Ring Nebula, ApJ

Guerrero, Manchado, Chu: 1997, Chemical abundances and kinematics of the Ring Nebula, ApJ

O'Dell, Henney, Sabbadin: 2006, Motions and spectroscopy within NGC 6720, AJ



# Star Formation Rate in NGC 2903, NGC 3310 and NGC 3351

Beghini Alessandro<sup>1</sup>, Benedetti Silvio<sup>2</sup>, Faccioli Luca<sup>3</sup>, Gaspari Silvia<sup>4</sup>, Lonardi Fabio<sup>2</sup>, Signorini Stefano<sup>2</sup>

<sup>1</sup>Liceo *G. Fracastoro*, Verona <sup>2</sup>Liceo *P. Levi*, S. Pietro in Cariano <sup>3</sup>Liceo *E. Medi*, Villafranca <sup>4</sup>Liceo *M. Curie*, Garda

Abstract. An abstract should be given

#### 1. Introduction

Stars are formed in consequence of a gas and dust cloud collapse. These clouds have masses up to  $10^6~M_\odot$  and temperatures in the range between -263~C and few degrees below zero. The cloud stability is guaranteed by the equilibrium between gravitational and pressure forces. When the pressure is not sufficient to counterbalance the gravitational force the cloud collapses. This happens when the cloud mass is greater than the Jeans mass, given by  $M_J \geq 10^{23} \times T^{3/2}/\sqrt{\rho}$ .

Alternatively a supernova explosion in the cloud proximity could be able to provoke the cloud compression through a shock wave of ejected gas. The cloud stability could be compromised and the gravity gets the upper hand over the pressure.

In consequence of the cloud collapse, the cloud core temperature reaches 10 million degrees and the fusion process is ignited: in these conditions 4 protons are assembled to form a Helium nucleus (pp cycle).

Star formation happens mostly in the spiral arms because in these regions there are higher dust and gas concentrations.

In this work we analyse different regions in four galaxies: NGC 660, NGC 2903, NGC 3310 and NGC 3351 (Figure 1). The aim of our work is to estimate the SFR in these regions, evaluate the number of stars which are able to ionize the surrounding gas and to measure the electronic density.

#### 2. Observational data

The spectra were collected with B&C spectrograph at the Galileo telescope, 122cm, of Asiago Astrophysical Observatory, University of Padua, during the night

**Table 1.** Observed objects

Obj	R.A.	Dec.	D (Mpc)	Cl
NGC2903	09 29 20	+21 43 20	8.0	Sb/Sc
NGC660	01 40 22	+13 23 37	11.7	SBa
NGC3310	10 38 46	+53 30 12	13.0	Sb/Sc (r)
NGC3351	10 43 58	+11 42 14	9.0	SBb

between February 4th and 5th 2010, using the 300 grooves/mm grism and a slit aperture of 2.5".

The main characteristics of the observed objects are shown in Table 1.

Each spectrum was corrected for BIAS, Darks and Flat Fields, then sky subtracted, wavelength calibrated using a HgAr lamp and finally flux calibrated using the standard star HD84937. From these bi-dimensional spectra were extracted the spectra relative to each particular region, looking at the  $H\alpha$  profile along the slit.

#### 3. Work description

In NGC 3310 we found 4 regions named s2, s1, d1 and d2 respectively (Figure 2). In NGC 660 no regions were extracted because of the low signal-to-noise, probably the exposure time was too short (Figure 3. In NGC 2903 6 regions were extrated namely s1, s2, s3, s4, s5 and s6 respectively, on the other hand in NGC 3351 only two regions, a1 and a2, were analyzed. In the Figures 4, 5, 6 are shown the  $H\beta$  and  $H\alpha$  ranges of the regions' spectra for each galaxy. For NGC 3351 there is only the  $H\alpha$  range because of the low S/N.

The measured emission line fluxes are shown in Tables 2, 3, 4.



**Fig. 1.** Observed galaxies. From the top NGC 2903 (by Keith B. Quattrocchi), NGC 660 (by Ken Crowford), NGC 3310 (HST archive) and NGC 3351.

For each region we measured the Balmer decrement of  $H\alpha/H\beta$ . As a rule the values are greater than the theoretical value 2.86 (intrinsic ratio). This is due to the absorption (reddening) of neutral gas and dust

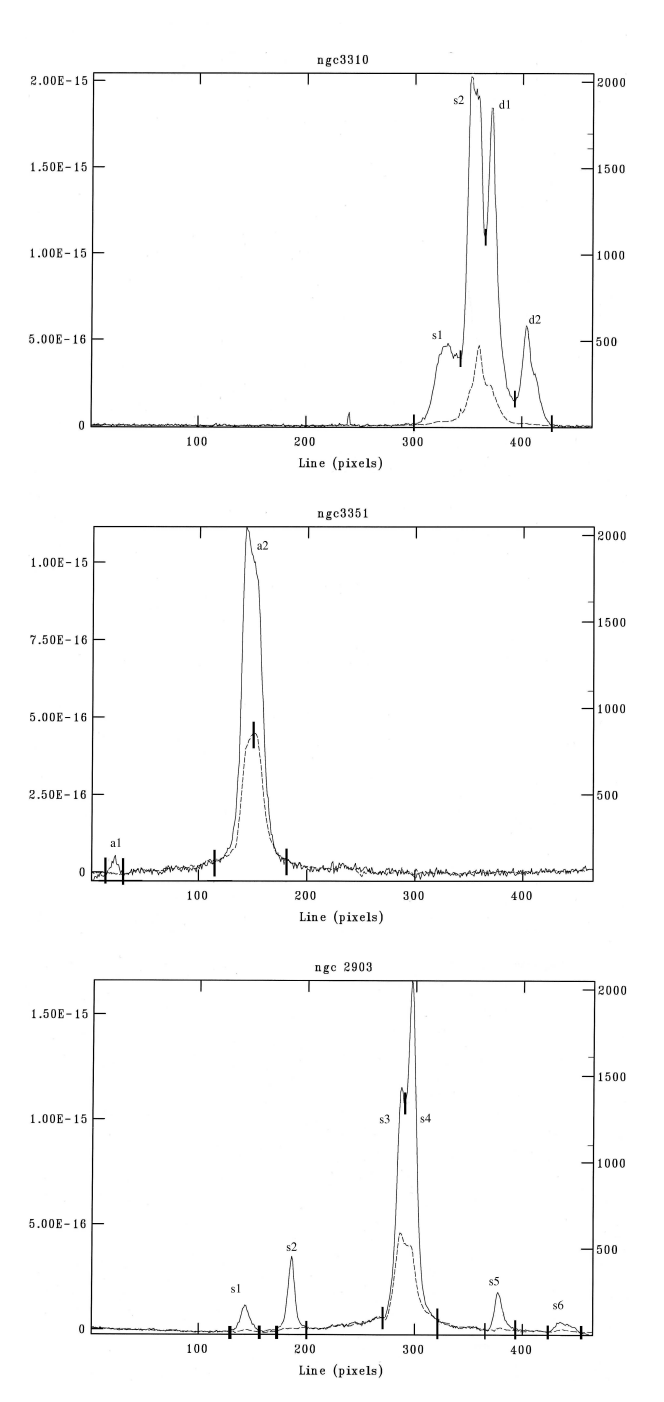


**Fig. 2.**  $H\alpha$  profile along the slit for NGC 3310, NGC 3351 and NGC 2903 respectively. In the figures are indicated the regions.

along the line of sight. In order to evaluate the reddening we applied the extinction law parametrized by Cardelli, Clayton, & Mathis (1989):

 $[I(H\alpha)/I(H\beta)]_i = [I(H\alpha)/I(H\beta)]_o \cdot 10^{-0.1386 \cdot A(V)}$ 

where  $[I(H\alpha)/I(H\beta)]_i$  and  $[I(H\alpha)/I(H\beta)]_o$  are the intrinsic and observed ratios respectively.

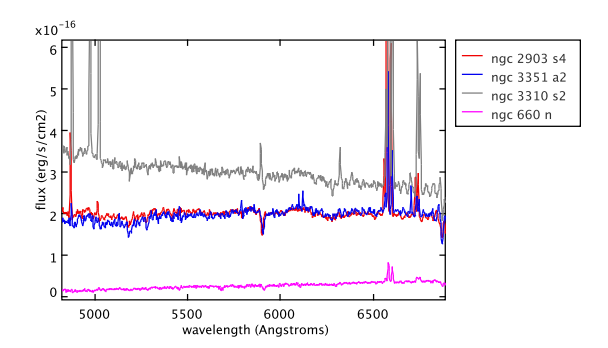
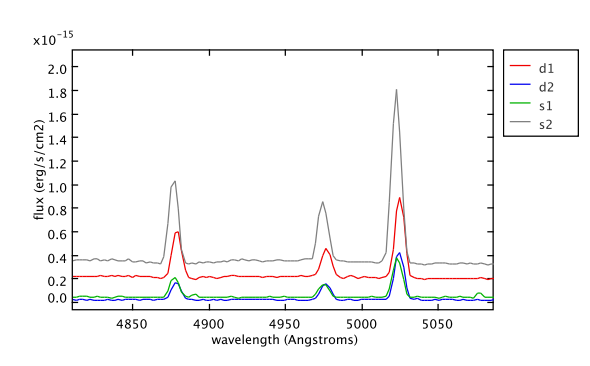
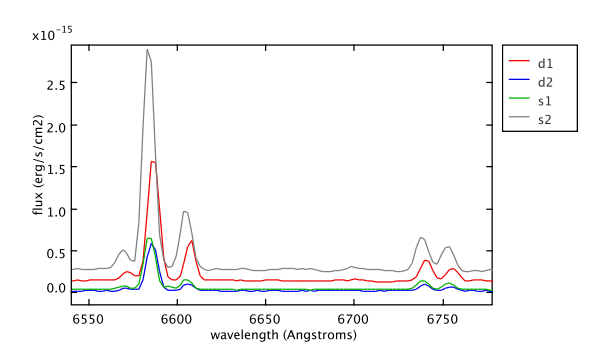
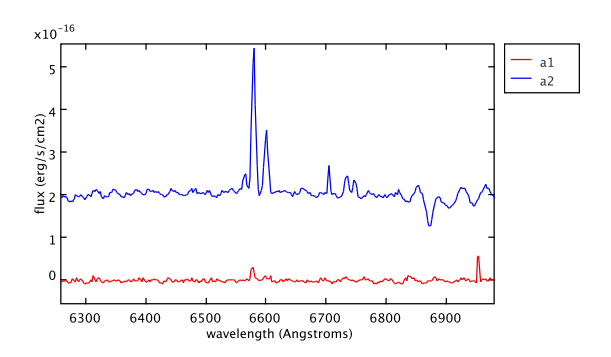


Fig. 3. Spectra with higher S/N.

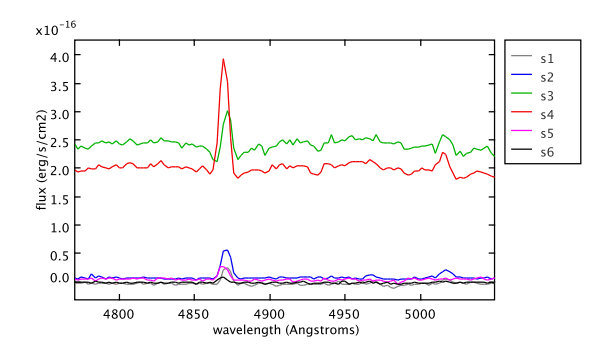




**Fig. 4.** NGC 3310:  $H\beta$  (top) and  $H\alpha$  (bottom) ranges.



**Fig. 5.** NGC 3351:  $H\alpha$ .



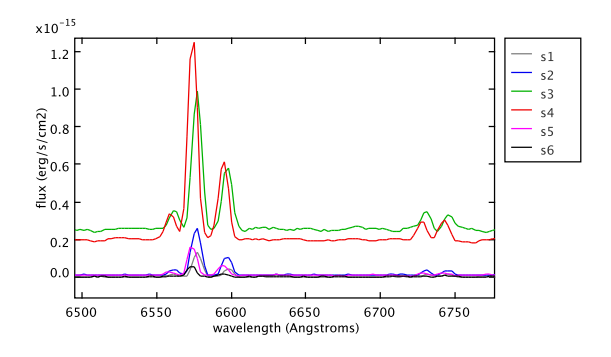


**Fig. 6.** NGC 2903:  $H\beta$  (top) and  $H\alpha$  (bottom) ranges.

**Table 2.** NGC3310, measured fluxes  $erg cm^{-2} s^{-1}$ 

region	s1	s2	d1	d2
[OII]3727	3.97E-15	1.53E-14	9.88E-15	2.72E-15
$H\beta$	1.29E-15	5.50E-15	3.11E-15	1.06E-15
[ <i>OIII</i> ]4959	8.84E-16	3.77E-015	2.00E-15	1.11E-15
[OIII]5007	2.52E-15	1.14E-14	5.38E-15	3.12E-15
[ <i>NII</i> ]6548	3.34E-16	1.77E-15	8.77E-16	2.27E-16
$H\alpha$	4.91E-15	2.16E-14	1.17E-14	4.39E-15
[ <i>NII</i> ]6584	3.43E-16	5.98E-15	3.40E-15	6.55E-16
[S11]6716	7.93E-16	3.30E-15	1.78E-15	4.44E-16
[S II]6731	6.06E-16	2.47E-15	1.06E-15	3.15E-16

**Table 3.** NGC3351, measured fluxes  $erg cm^{-2} s^{-1}$ 

region	a1	a2
[ <i>OII</i> ]3727	,	5.09E-16
$H\beta$	,	3.75E-16
[ <i>OIII</i> ]4959	,	,
[ <i>OIII</i> ]5007	,	,
[ <i>NII</i> ]6548	,	2.59E-16
$H\alpha$	2.21E-16	2.50E-15
[ <i>NII</i> ]6584	,	1.10E-15
[ <i>S II</i> ]6716	,	4.05E-16
[ <i>S II</i> ]6731	,	2.96E-16

From this formula we obtain A(V), then  $A(H\alpha)$  is given by the following relation

 $A(H\alpha) = A(V) \cdot 0,8177$ 

finally the  $H\alpha$  corrected flux is obtained by

**Table 4.** NGC2903, measured fluxes  $erg cm^{-2} s^{-1}$ 

region	s1	s2	s3
[ <i>OII</i> ]3727	1.86E-16	3.77E-16	,
Нβ	2.83E-16	4.07E-16	6.42E-16
[ <i>OIII</i> ]4959	,	,	,
[ <i>OIII</i> ]5007	,	1.03E-16	3.18E-16
[ <i>NII</i> ]6548	9.95E-17	2.46E-16	7.68E-16
$H\alpha$	9.76E-16	1.97E-15	5.830-15
[ <i>NII</i> ]6584	3.35E-16	7.56E-16	2.75E-15
[S11]6716	1.23E-16	1.54E-16	8.42E-16
[S11]6731	1.09E-16	1.55E-16	6.93E-16
region	s4	s5	s6
[OII]3727	7.24E-16	5.72E-17	1.08E-16
Ηβ	1.55E-15	1.92E-16	7.75E-17
[0]]]]1050	_		
[ <i>OIII</i> ]4959	,	,	,
[ <i>OIII</i> ]4959 [ <i>OIII</i> ]5007	3.29E-16	,	,
	3.29E-16 1.15E-15	, , 1.09E-16	, , 4.29E-17
[ <i>OIII</i> ]5007		, 1.09E-16 1.14E-15	, 4.29E-17 4.33E-16
[ <i>OIII</i> ]5007 [ <i>NII</i> ]6548	1.15E-15		
[OIII]5007 [NII]6548 Ηα	1.15E-15 8.68E-15	1.14E-15	4.33E-16

**Table 5.**  $H\alpha$  measured and reddening corrected fluxes  $erg \ cm^{-2} \ s^{-1}$ 

Obj	region	$I(H\alpha)_o$	$I(H\alpha)_c$
NGC3310	s1	4.91E-15	9.71E-15
	s2	2.16E-14	4.77E-14
	d1	1.17E-14	2.23E-14
NGC3351	a1	2.21E-16	
	a2	2.50E-15	1.28E-14
NGC2903	s1	9,76E-16	1.52E-15
	s2	1.97E-15	6.83E-15
	s3	5.83E-15	8.91E-14
	s4	8.68E-15	4.27E-14
	s5	1.14E-15	6.38E-15
	s6	4.33E-16	3.00E-15

 $I(H\alpha)_c = I(H\alpha)_o \cdot 10^{0.4 \cdot A(H\alpha)}$ 

where  $I(H\alpha)_c$  and  $I(H\alpha)_o$  are the corrected and observed flux respectively (Table 5).

In order to verify the nature of the analyzed regions we applied the principal diagnostic diagram of Veilleux and Osterbrock (1987),  $log([OIII]H\beta)$  vs  $log([NII]H\alpha)$ , parametrized by Kewley et al. (2006). This diagram is able to separate the star forming regions from the AGN (Active Galactic Nuclei). The distribution on this diagram shows that our spectra are in the star forming region, so they are relative to HII regions (Figure 7). The fluxes used in these ratios were not corrected by absorption, anyway these ratios are reddening free because the ratios involve lines with similar wavelengths. Not all the analyzed regions were classified because [OIII]5007 was not measurable in all the spectra, in particular all the spectra of NGC 3351 have a low signal-to-noise for this line.

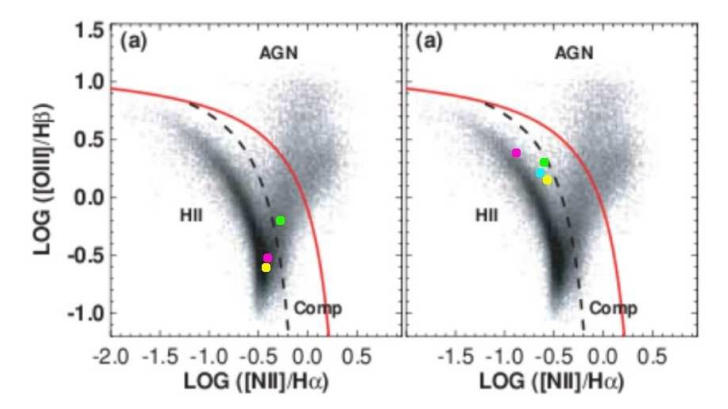


**Fig. 7.** Spectra classification of NGC 2903 (*left*) and NGC 3310 (*right*) regions

#### 3.1. SFR determination

SFR is the mass trasformed in new stars per year and per unit of surface, the mass is given in solar mass unit. In order to determine the SFR for each analyzed region we have to determine its surface. Each region is assumed rectangular, the width is given by the slit width (2.5''), the high is given by the number of pixels taken into account. The scale (S) on the focal plane is S = D(kpc)/206265, then the high (H) is  $H = S \cdot 2.5$ , and the width (W) is  $W = H(arcesc) \cdot S$ . Finally, the surface is obtained by  $W \cdot H kpc^2$ .

Next, it is necessary to determine the galaxy surface. If we assume the galaxy similar to an ellipse, the total surface is given by  $ab\pi$ , where a and b are the semi-axis major and minor respectively. Multiplying the SFR for the total galactic surface we derived the upper limit of the total SFR, under the hypothesis that the SFR surface density of the galaxy was equal to the considered region. We stress that this result is an upper limit of the galactic SFR, because not all the galactic regions are producing stars, the star formation is limited to restricted regions.

With the corrected flux of  $H\alpha$  is possible to find the  $H\alpha$  luminosity:

$$L(H\alpha) = 4\pi D^2 \cdot I(H\alpha)$$

where *D* is the distance of the galaxy. The measured luminosities are shown in Table 6 SFR is obtained applying the following formula (Kennicutt 1983)

$$SFR = 7.9 \cdot 10^{-42} \cdot L(H\alpha)$$

#### 3.2. Density determination

The electronic density  $(Ne \, cm^{-3})$  is determined from the ratio of the  $[S\,II]$ 6716, 6731 forbidden lines. In Figure 8 (Aller 1984) is shown the variation of  $I_{6716}/I_{6731}$  with the electronic density (Log(Ne)). In some regions was not possible to determine the density

**Table 6.**  $H\alpha$  luminosities  $erg\ s^{-1}$ , and SFR

Obj	Region	L (erg/s)	SFR	max SFR
NGC3310	s1	1.95E+038	1.54E-003	0.55
	s2	9.57E+038	7.56E-003	4.82
	d1	4.47E+038	3.53E-003	1.71
	d2	2.11E+038	1.67E-003	0.71
NGC3351	a1	###	###	###
	a2	1.14E+038	9.00E-004	0.25
NGC2903	s1	1.17E+037	9.24E-005	###
	s2	5.24E+037	4.14E-004	1.96
	s3	6.83E+038	5.40E-003	40.83
	s4	3.27E+038	2.58E-003	10.6
	s5	4.89E+037	3.55E-003	17.41
	s6	2.30E+037	1.82E-004	0.83

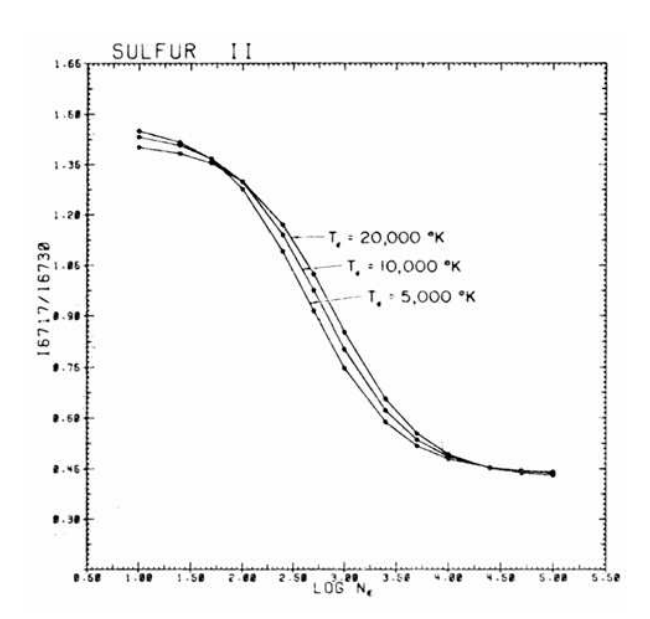


**Fig. 8.**  $Log(I_{6716}/I_{6731})$  vs Log(Ne) for three different temperatures (from Aller, 1984).

because the lines are too weak, alternatively the densities were too low, in fact the ratio is sensitive in the range  $30 - 10000 \, cm^{-3}$  (Table 7).

#### 3.3. Number of hot stars

The emission permitted lines are formed when the electrons are recombined with the respective ions. The recombination to the original level produces the photoemission. This emission added to the continuum photons produces the emission line. The ionizing photons are generated by hot stars. In an HII region, ionizations and recombinations reach an equilibrium, the number of ionizations is equal to that of recombinations, therefore the flux, and the luminosity, of a recombination spectral line is correlated to the ionizing photons. If we know the typical number of that kind of photons produced by an hot star, it is possible to estimate the quantity of hot stars from the flux of a recombination line.

**Table 7.** Density  $N_e$ 

Obj	Region	$I_{6716}/I_{6731}$	Ne $cm^{-3}$
NGC3310	s1	1.31	108
	s2	1.34	75
	d1	1.68	###
	d2	1.41	24
NGC3351	a1	###	###
	a2	1.37	52
NGC2903	s1	1.13	340
	s2	0.99	562
	s3	1.22	237
	s4	0.91	806
	s5	1.04	523
	s6	0.77	1334

Table 8. Number of O5 and B1 stars

Obj	Region	$Q_{ion} s^{-1}$	N(O5)	N(B1)
NGC3310	s1	1.42E+050	2.85	47450
	s2	6.99E+050	13.97	232870
	d1	3.26E+050	6.53	108770
	d2	1.54E+050	3.08	51343
NGC2903	s1	8.54E+048	0.17	2847
	s2	3.83E+049	0.77	12751
	s3	4.99E+050	9.97	166197
	s4	2.39E+050	4.77	79570
	s5	3.57E+049	0.71	11899
	s6	1.68E+049	0.34	5597
NGC3351	a1	#	#	#
	a2	8.32E+049	1.66	27725

The number of ionizing photons is given by  $Q_{ion}(ph/s) = 7.3 \cdot 10^{11} \cdot L(H\alpha)$ .

In this estimation we took into account only O5 and B1 stars, because these stars are the main sources of the photons we need.

The number of ionizing photons produced from these stars are:

$$Q_{ion}(O5) = 5 \cdot 10^{49} \ (ph/s)$$

$$\widetilde{Q}_{ion}(B1) = 3 \cdot 10^{45} \; (ph/s)$$

Of course, we are not able to determine the ratio between O5 and B1 stars that can be found in the region, therefore we assumed, arbitrarily, an equivalent number of ionizing photons produced by both kinds of stars.

Then the number of stars is directly obtained:

$$N(OB) = (Q_{ion}/2)/Q_{ion}(O5)$$

$$N(B1) = (Q_{ion}/2)/Q_{ion}(B1)$$

In this way we obtained an estimate of the number of O5 and B1 stars ionizing the same region (Table 8).

#### 4. Results

Obviously now we have to check our results. If we look "Misura del tasso di formazione stellare nella galassia a spirale NGC 3338" (Boscolo et al. 2006) we can consider acceptable the SFRs of the galaxies we studied. Regarding the upper limits of SFR, reading Larson & Tinsley (1978) we find results in accordance with ours. The number and ratio of the O and B

stars are fairly correct, reminding that the right ratio is  $10^4 \sim 10^5$ . We consider also very interesting the impossibility of using some measurment obtained at the telescope, such as NGC 660 spectra. This fact helped us to understand the difficulties encontered doing real researches.

#### References

Aller, L. H., 1984, in Physics of thermal gaseous nebulae, Astrophysics and space science library; v. 112, p.140

Boscolo, Cecchini, Penzo, Ribin 2006, The Sky as a Laboratory 06/07, pp 67-70, Univ. Padova.

Cardelli J. A., Clayton G. C., Mathis J. S., 1989, IAUS, 135, 5P

Kennicutt R. C., Jr., 1983, ApJ, 272, 54

Kewley L. J., Groves B., Kauffmann G., Heckman T., 2006, MNRAS, 372, 961

Kewley L. J., Groves B., Kauffmann G., Heckman T., 2006, MNRAS, 372, 961

Larson R. B., Tinsley B. M., 1978, ApJ, 219, 46



# ugriz & JHK<sub>S</sub> photometry of elliptical galaxy M59 and spiral galaxy NGC 2903

Michele Caovilla<sup>1</sup>, Federico Chiariotti<sup>2</sup>, Tommaso Frassetto<sup>1</sup>, Giulio Menegus<sup>1</sup>, Francesco Raccanello<sup>1</sup>, Alvise Sernicola<sup>3</sup>, Martino Trabuio<sup>4</sup>

<sup>1</sup>Liceo scientifico *G. Galilei*, Dolo <sup>2</sup>Liceo scientifico *G. Berto*, Mogliano Veneto <sup>3</sup>Liceo scientifico *L. da Vinci*, Treviso <sup>4</sup>Liceo scientifico *G. Bruno*, Mestre

**Abstract.** Our survey aimed at studying the photometry of the elliptical galaxy M59 and spiral galaxy NGC 2903 in 3 visible (g, r, i) and 2 near-infrared  $(H, K_S)$  bands. This study allowed us to develop and compare morphological models and brightness profiles of both galaxies.

#### 1. Introduction

Studying the morphology of galaxies is one of the most important targets in astronomy, as it is the first step towards understanding their physics: it allows us to learn more about their stellar population, their formation and age.

For decades, the morphological classifications (primarily Edwin Hubble's one) of galaxies were based upon subjective and empirical criteria. In recent times, division into morphological classes is no longer based directly on images; today we rely on quantitative methods that involve digital image processing. We use computers to draw isophote lines (i.e. lines that link pixels with the same approximate brightness) on the digital images of galaxies; we then approximate them to ellipses and plot their main physical and photometric characteristics in order to analyze how they change in function of the distance from the galactic center. Analyzing graphs is a way to sort galaxies into morphological classes. We used this method to classify and study the elliptical galaxy M59 (also known as NGC 4621) and the spiral galaxy NGC 2903.

Regular galaxies are traditionally divided into elliptical, lenticular, spiral and irregular. Elliptical galaxies appear as ellipses and have a smooth, featureless light distribution; they are marked with the letter "E" followed by a single digit that represents the ellipticity  $(e=1-\frac{b}{a}, b \text{ and } a \text{ being respectively the lengths of the semi-minor axis and semi-major axis) multiplied by 10 and rounded; so E0 denotes a near-circular galaxy, while E7 denotes a heavily flattened galaxy. Evidently, we measure the axes on the images we can take from$ 

the Earth, so we cannot determine whether a galaxy appears as an ellipse (or a circle) because it actually is so or because we are not looking at it from its top.

The main feature of spiral galaxies is the presence of a disk, on which one or more (usually two) spiral arms extend from the bulge. Some spiral galaxies, including NGC-2903, have a bar-like structure crossing the bulge, at the ends of which the spiral arms begin. According to Hubble's classification, all spiral galaxies are marked with a capital S, but barred spiral galaxies have an additional capital B. There are three S sub-types, marked a, b and c. Sa and SBa galaxies are similar to lenticular galaxies, as the bulge is very pronounced and the spiral arms are shorter and tightly wound, while Sc and SBc galaxies have a small bulge and longer, loosely wound arms.

Lenticular galaxies are similar to elliptical ones, with a prominent bulge, but they share the disk feature with spiral galaxies, although without any arm.

#### 2. Observational data

The images we worked on have been taken from two public image archives: SDSS for visible light bands and 2MASS for the near-infrared ones. The SDSS (*Sloan Digital Sky Survey*) has obtained images of more than a quarter of the sky in over than eight years of operation and is planned to continue through 2014; its data have been released to the scientific community in annual releases. SDSS uses a dedicated 2.5-meter telescope at Apache Point Observatory, in New Mexico (USA); its images use the ugriz photometric filter set, composed

of five filters (u, g, r, i, z), whose central wavelengths are:

1	u	g	r	i	Z
	3551 Å	4686 Å	6165 Å	7481 Å	8931 Å

The 2MASS (Two Micron All Sky Survey) aimed at providing near-infrared imaging of the whole sky to replace the old images taken by the TMSS (Two Micron Sky Survey) in the sixties; it began in 1997 and was completed in 2001. It was meant to detect galaxies in the zone of avoidance, a strip of sky where dust within the Milky Way makes optical galaxy surveys incomplete, to discover some brown dwarfs and low mass stars and to catalog everything it had detected. It used two 1.3-meter telescopes, one in Mt. Hopkins, Arizona (USA) and one at CTIO (Chile). It used the standard near-infrared JHK<sub>S</sub> filter set, whose central wavelengths are:

J	Н	$K_S$
$1.25  \mu {\rm m}$	$1.65  \mu {\rm m}$	$2.17  \mu \text{m}$

The coordinates of M59 and NGC 2903 are:

Object	M59	NGC 2903
Right Ascension	12h42m02.3s	09h32m10.1s
Declination	+11d38m49s	+21d30m03s
Constellation	Virgo	Leo

The digital images provided by either SDSS or 2MASS are arrays of pixels; each pixel has a value that is proportional to the number of photons collected by the photosensitive element. The position of a point in the image is commonly expressed in pixels; each pixel corresponds to 0.4 arcseconds in the SDSS images and to 1 second of arc in the 2MASS ones.

#### 3. Work Description

#### 3.1. Elliptical galaxy M59

### 3.1.1. Preliminary task: the distance

In order to calculate the distance we used a spectrum of the galaxy (figure 2) taken from NED (NASA/IPAC Extragalactic Database) and calculated the redshift of the H $\alpha$  spectral line. From the spectrum we measured the wavelength of the top of the H $\alpha$  line (see figure 3) that is at 6537 Å. The wavelength measured in the lab-

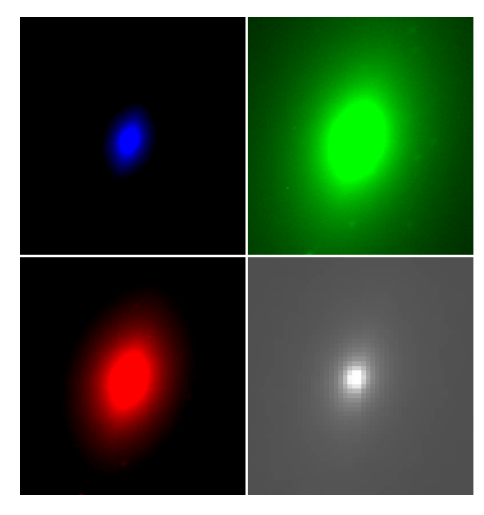


**Fig. 1.** M59 images in g, r (top), i, H (bottom) filters, north up, east left. The first three images have the same colormap settings (contrast and bias).

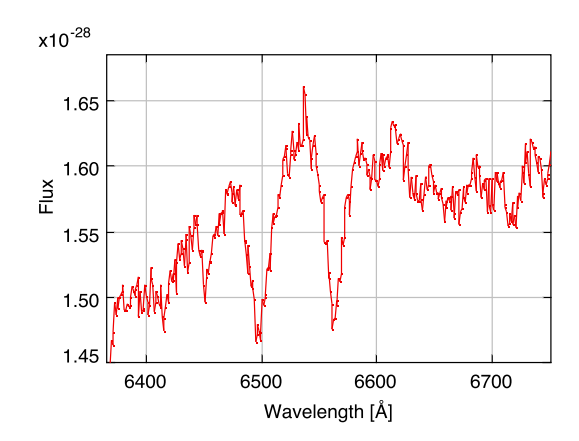


**Fig. 2.** M59 spectrum around H $\alpha$ .

oratory is 6563 Å.

$$z = \frac{v}{c} = \frac{\Delta \lambda}{\lambda} \tag{1}$$

$$v = z \cdot c \tag{2}$$

$$d = \frac{v}{H_0} = \frac{\Delta \lambda \cdot c}{\lambda \cdot H_0} \approx 16.9 \text{ Mpc}$$
 (3)

We used  $H_0 \approx 70 \frac{\text{km}}{\text{s·Mpc}}$ , corresponding to an age of the universe  $\approx 14$  billion years; we also neglected the relativistic effects because  $z \approx 0.004 \ll 1$ .

In the SDSS images, each pixel is 0.4'' wide; the actual width of the pixel is  $\alpha \cdot d$ , with  $\alpha$  in radians; an arcsecond is  $\approx \frac{1}{206265}$  rad, so we obtain:

$$l = (.4'') \cdot \left(\frac{1''}{206265 \text{ rad}}\right) \cdot (16.9 \text{ Mpc}) \approx 33 \frac{\text{pc}}{\text{pixel}}$$
 (4)

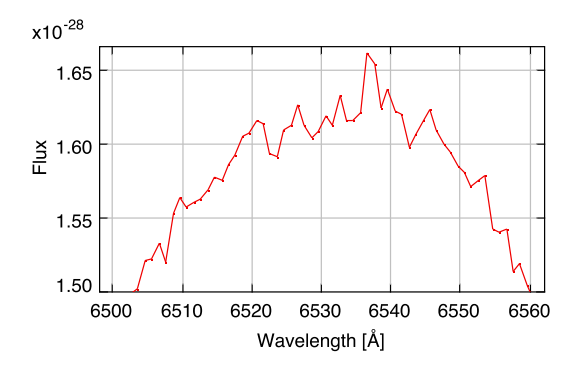


**Fig. 3.** M59 spectrum of the H $\alpha$  line.

while for 2MASS images (whose pixels are 1" wide), we obtain:

$$l = (1'') \cdot \left(\frac{1''}{206265 \text{ rad}}\right) \cdot (16.9 \text{ Mpc}) \approx 82 \frac{\text{pc}}{\text{pixel}}$$
 (5)

#### 3.1.2. Isophote ellipses

We began our study of the photometry of the elliptical galaxy M59 by drawing an ellipse circumscribing the galaxy and determining its main characteristics, like its semi-minor axis and semi-major axis (SMA), ellipticity, position angle (PA), and coordinates of the ellipse's center (X0 and Y0, the coordinates of the center in the images, expressed in pixels).

We then used the ellipse task of IRAF software (Image Reduction and Analysis Facility) to draw isophotes ellipses of increasing brightness inwards and decreasing outwards; the program could change the axes, the position angle and the center. The software was provided with our ellipse's data and the digital image; we had previously masked the brightest stars around the galaxy to increase software accuracy. The isophote ellipses it found have then been checked for consistency; the coherent ones have been used. We stopped when the computer was no longer able to draw isophotes (it usually happened near the outer limit of the galaxy). So we obtained a set of ellipses with the main characteristics of each one.

Then, we used again the ellipse task; this time, the center's coordinates were set as the coordinates of the ellipse we drew at the beginning. This way, we obtained a second set of ellipses sharing the same center.

We followed the same procedure for the five images we were processing (taken in the g, r, i, H and  $K_S$  filters respectively).

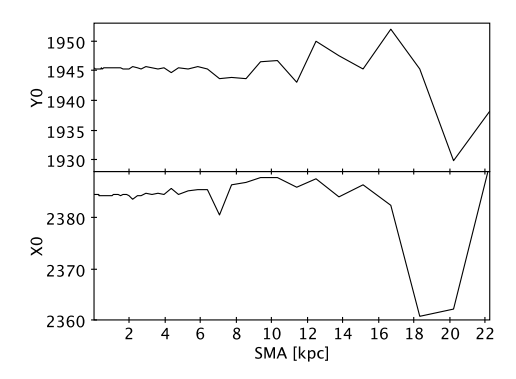


**Fig. 4.** Plot of the coordinates of the isophotes centers found in the image (filter r).

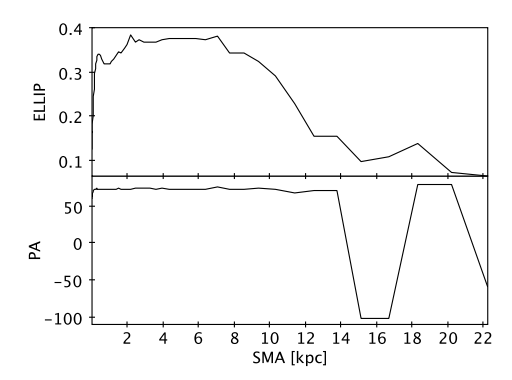


**Fig. 5.** Plot of position angle and ellipticity of the isophotes found in the image (filter r).

#### 3.1.3. Morphological model

To analyze the way the ellipses vary in function of the semi-major axis, we plotted the ellipticity, the position angle and the center coordinates with the TOPCAT software (*Tool for OPerations on Catalogues And Tables*); the resulting graphs are figures 4 and 5. The graphs show that the coordinates of the centers, the ellipticity and the position angle of the ellipses are quite steady (at least until 15 kpc); similar graphs have been obtained by processing the images taken in the other filters. The fact that the isophotes we obtained with the different images are similar proves that M59 is really an elliptical galaxy and it does not possess spiral arms or a disk.

In order to verify the consistency of our isophote ellipses, we used the bmodel task for each filter to build an image based on the brightness of each ellipse, i.e. to draw a morphological model. Then we subtracted the value of each pixel of the model images from the original ones; the resulting residuals were nearly flat, showing very little trace of the galaxy; that means that the models are consistent with the actual images. The

 $e = 1 - \frac{b}{a}$ , b and a being the lengths of the axes.

<sup>&</sup>lt;sup>2</sup> The position angle is the angle between the major axis and the north, measured towards the east, expressed in degrees.

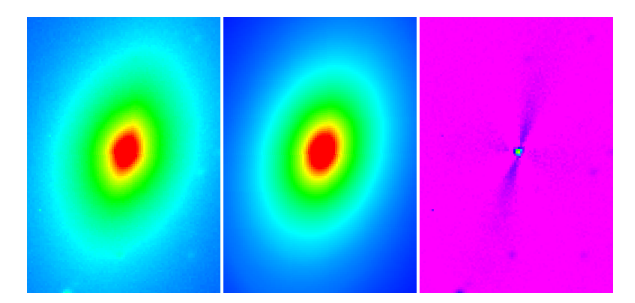


**Fig. 6.** From left to right: M59 image in r filter; morphological model for the previous image; residual of the previous model. All three images share the same colormap settings.

original image, model image and residual for filter r are shown in figure 6.

#### 3.1.4. Brightness profiles

We used a macro to calculate the surface brightness of the area near each ellipse in the different filters from the tables of ellipses with a fixed center. The formula it used is:

$$I_{surf} = \frac{I_{\star} - I_{sky} \cdot N_{pix}}{t_{exp} \cdot A_{pix}}$$
 (6)

where  $I_{\star}$  is the measured flux (taken from the TFLUX\_E column produced by the ellipse tool),  $I_{sky}$  is the average value of the pixels outside the galaxy,  $N_{pix}$  is the number of pixels,  $t_{exp}$  is the exposure time and  $A_{pix}$  is the surface of each pixel. Then, we calculated the instrumental magnitude  $\mu$ :

$$\mu_{\text{inst}} = -2.5 \cdot \log I_{\text{surf}} \tag{7}$$

To calculate the actual magnitude from the instrumental one, we used the following formula:

$$m_{cal} = \mu_{inst} + m_0 - k \cdot x \tag{8}$$

where  $m_0$  is the photometric zero point, k is the extinction coefficient and x is the airmass (all three parameters are provided either in the SDSS site or in the header of the 2MASS images).

Then we tried to fit the magnitude data with some empirical laws; the most effective one is the one that approximates the brightness profile of a bulge, named after the French astronomer Gérard Henri de Vaucouleurs (1918–1995):

$$\mu_{\rm B} = \mu_{\rm e} + 8.325 \left[ \sqrt[4]{\left(\frac{\rm r}{\rm r_{\rm e}}\right)} - 1 \right]$$
 (9)

We found the best parameters by trial and error plotting the model and the actual data using TOPCAT; the optimal parameters are

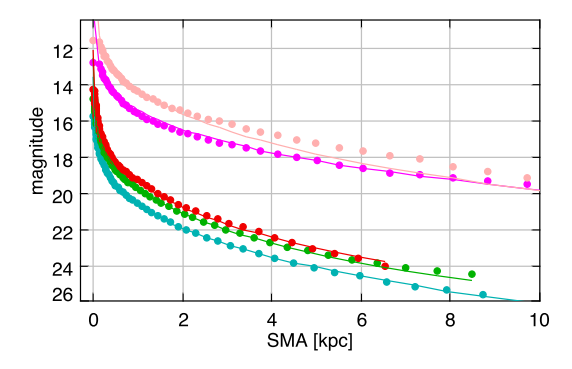


**Fig. 7.** Graph of the magnitudes (dots) and models (lines); g filter data are light blue, r are green, i are red, H are dark pink,  $K_S$  are light pink.

Filter	$\mu_{ m e}$	r <sub>e</sub> (pixels)	r <sub>e</sub> (arcseconds)
g	22	60	24
r	21	55	22
i	20.5	51	20.4
Н	18.2	58	58
Ks	15.5	22	22

Then we considered the morphological type of the galaxy: the average ellipticity in the different filters was 0.28, so the galaxy's type is E3.

Finally, we calculated the magnitude of the galaxy in the different filters. The total brightness of the galaxy is:

$$I_{tot}^{bulge} = 11.93 \cdot I_e \cdot r_e^2 \tag{10}$$

where  $I_e$  is the brightness computed from  $\mu_e$ :

$$I_e = 10^{(\mu_e/-2.5)}$$
 (11)

and  $r_e$  is measured in arcseconds. The total magnitude is:

$$m_{\text{tot}} = -2.5 \log I_{\text{tot}}^{\text{bulge}} \tag{12}$$

Our results are:

Filter	m <sub>tot</sub>
g	12.41
r	11.60
i	11.26
Н	6.69
$K_S$	6.10

We plotted the actual magnitudes and the ones from the model in the same graph; the result is figure 7.

#### 3.1.5. Results

Our calculations show that the brightness is greater in the images taken in the filters towards the infrared light.

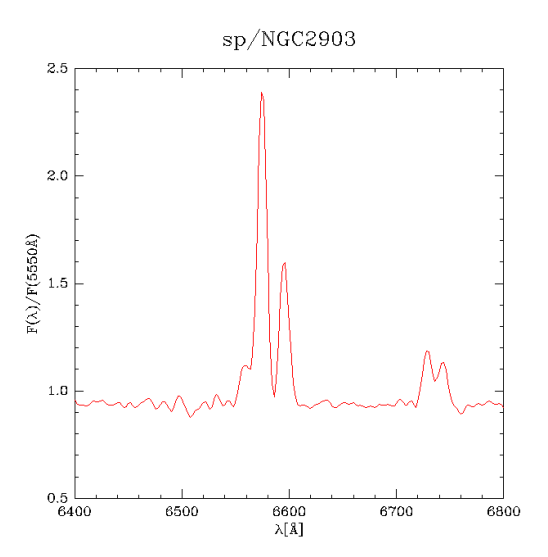


**Fig. 8.** NGC2903 spectrum around H $\alpha$ .

This happens because the galaxy is quite old and its stars emit more light in the infrared bands.

The residuals (figure 6) show a darker cross whose arms form an angle of 45 degrees with the axes of the galaxy. Thus, the galaxy's isophotes are disky.<sup>3</sup> It is commonly accepted that galaxies with disky isophotes are supported by their rotation (while galaxies with boxy isophotes are pressure-supported). Recent studies such as Naab, Burkert & Hernquist (1999) show that both types of galaxies were originated from a merger event.

#### 3.2. Spiral Galaxy NGC 2903

#### 3.2.1. Preliminary task: the distance

As we did for M59, we used a spectrum of the galaxy we obtained from the NED Database to determine the redshift of the H $\alpha$  spectral line. The top wavelength of the H $\alpha$  line was measured at 6574 Å, whilst the laboratory value for H $\alpha$  is 6563 Å.

$$d = \frac{v}{H_0} = \frac{z \cdot c}{H_0} = \frac{\Delta \lambda \cdot c}{\lambda \cdot H_0} \approx 7.18 \text{ Mpc}$$
 (13)

For the details of this procedure, as well as the pixel sizes, please refer to section 3.1.1.

#### 3.2.2. Isophote ellipses

The spiral galaxy we studied is NGC 2903, a barred spiral galaxy about 20 million light-years away in the Leo constellation. The particularly intense star formation in the nucleus causes its brightness in the infrared region of the spectrum. We conducted the mor-

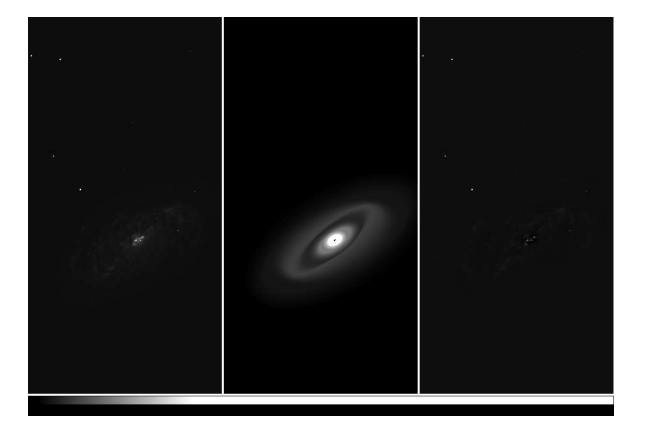


**Fig. 9.** Comparison between the actual galaxy (on the left), the virtual model (on the center) and the residue (on the right) in the g band

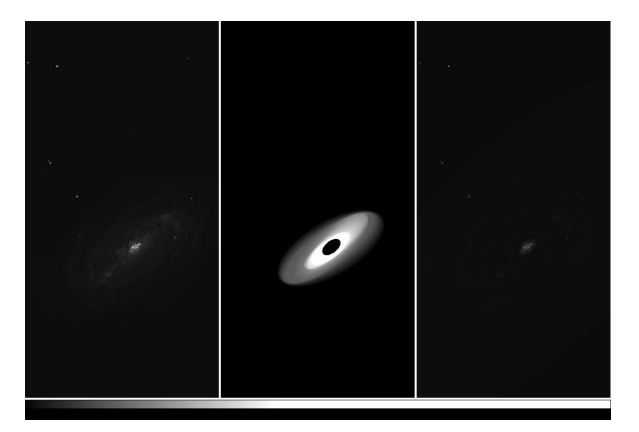


**Fig. 10.** Comparison between the actual galaxy (on the left), the virtual model (on the center) and the residue (on the right) in the r band

phological study of the galaxy by using curves along which the galaxy's luminosity is constant (isophotes). As NGC 2903 is a barred spiral galaxy, its isophotes are irregular, but we fit regular ellipses to the actual isophotes. The mathematics was performed by the ellipse tool of IRAF; after we had drawn an approximate elliptical border of the galaxy and chosen a center in the graphic interface program DS9, IRAF created a series of elliptical isophotes with the same center and another series whose ellipses had different centers. The program had some issues while calculating the smaller isophotes; this was due to the irregularity of the bulge, as its elongated shape prevented the program from calculating elliptical isophotes with a semi-axis smaller than about 50 pixels. However, outside the central area there were no major issues in the individuation of the isophotes. Basing on the isophotes we obtained, we used the bmodel tool of IRAF to create a theoretical model of the galaxy. We then subtracted the model from the original image to create a residual image: the residual represents the difference between the virtual model

<sup>&</sup>lt;sup>3</sup> Disky isophotes are like flattened ellipses; boxy ones are like taller ellipses.

and the actual appearance of the galaxy. As expected, the residual was quite significant because the virtual model is always an elliptical galaxy and NGC 2903 is a barred spiral one.

#### 3.2.3. Brightness profiles

We determined the brightness profile of the spiral galaxy NGC 2903 by using isophote ellipses with fixed centers, with different SMA and PA. The profile can be useful for analyzing the bulge and disk sections of the galaxy, plotting the graph results by means of empirical laws. Brightness expresses a measure of magnitude, relative to the area of a single pixel (in square arcseconds).

$$\mu = -2.5 \log (Intensity/PixelArea)$$
 (14)

The equivalence of the formula of magnitude,  $m = -2.5 \log (Intensity)$ , is justified, since Pixel Area is directly proportional to Intensity (the latter being defined as luminosity per surface unit).

However, the magnitude the brightness expresses is not real but instrumental, as the Intensity resulting from the photon counts per pixel does not represent a physical unit of measure. We have calculated a calibrated magnitude using the formula:

$$m_{cal} = \mu_{inst} + m_0 - k \cdot x \tag{15}$$

The photometric zero point  $m_0$ , the extinction coefficient k and the airmass x were provided by the SDSS or the 2MASS databases. The calibrated magnitude was determined empirically and equals the photon count in a dark area of the digital image.

We calculated one profile for each of the two sets of filters (ugriz and  $JHK_S$ ) choosing the data relative to g and H filters, which were identified as the most meaningful. In both cases, we set up the data concerning the ellipses with fixed centers (from IRAF) in a table (using TOPCAT) and we graphed the brightness values (calibrated magnitude, as defined above) in function of the distance from the fixed center (of the ellipses), measured in seconds of arc (1 Pix = 0.4") and then in kpc (multiplying the seconds by D/206265, D = distance of the galaxy).

We attempted to isolate and describe the structural components of the spiral galaxy (bulge, disk, and spiral) by plotting the observational data with the curves describing empirical laws for the behavior of these components' magnitudes. We were able to modify a series of arbitrary parameters of these laws and so adapt them to the profile of the galaxy. The brightness of the bulge (B) is described by the exponential bulge formula:

$$\mu(B) = \mu_e + 1.824 [(r/r_e) - 1]$$
 (16)

The parameters  $r_e$  and  $\mu_e$  express the effective radius, i.e. the SMA of the ellipse containing half the light of the galaxy, and the magnitude relative to  $r_e$ . The light

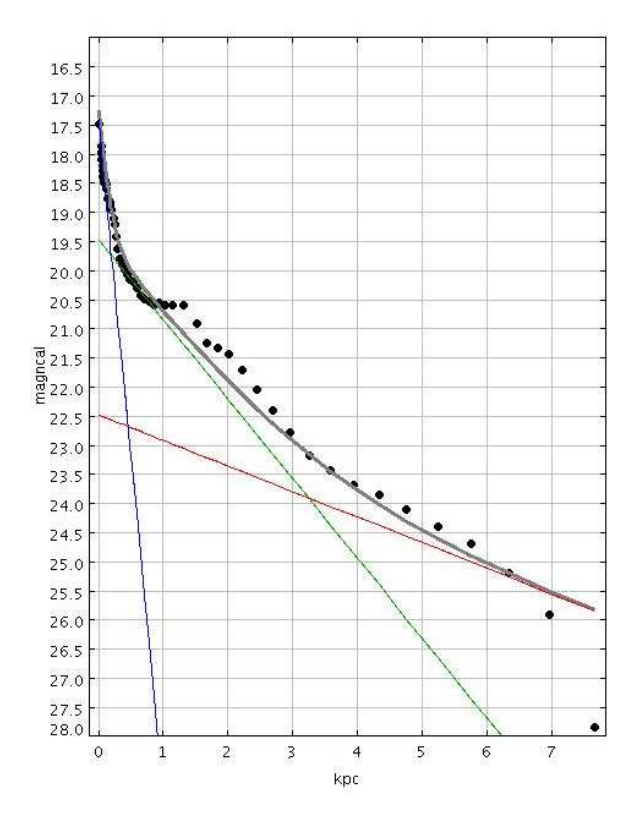


**Fig. 11.** Brightness profile of the g passband with the plotted curves made with empirical laws that represent the bulge and the two disks.

intensity of the bulge is described by the previous law turned to intensity:

$$I(B) = 5.36 \cdot I_e \cdot \exp[-1.68(r/r_e)]$$
 (17)

We were able to distinguish two separate disks (D) through the exponential disk formula:

$$\mu(D) = \mu_0 + 1.085 \,(r/h)$$
 (18)

that is:

$$I(D) = I(0) \cdot \exp(-r/h) \tag{19}$$

with h = scale height and I(0) = intensity in the galactic center.

This result led us to the hypothesis that NGC 2903 originated from the merging of two separate galaxies, which could explain its starburst quality (for the discussion on the results, see section 3.2.4).

Finally, we plotted the spiral, the magnitude of which is the total magnitude of bulge and disk components [as magnitude is a logarithm, the total cannot be a sum of magnitudes but the logarithm of the sum of Intensities =  $-2.5 \log(Bulge + Disk)$ ]. The arbitrary parameters  $I_e$ ,  $r_e$ , and h, determined above, allowed us to express the total intensity of bulge and disk  $[I(B) = 11.93 \cdot I_e \cdot r_e^2$  and  $I(D) = 2\pi h^2 \cdot I(0)$ ] and the intensity of the whole galaxy I(tot), as the sum of the former ones. These values were used to determine the

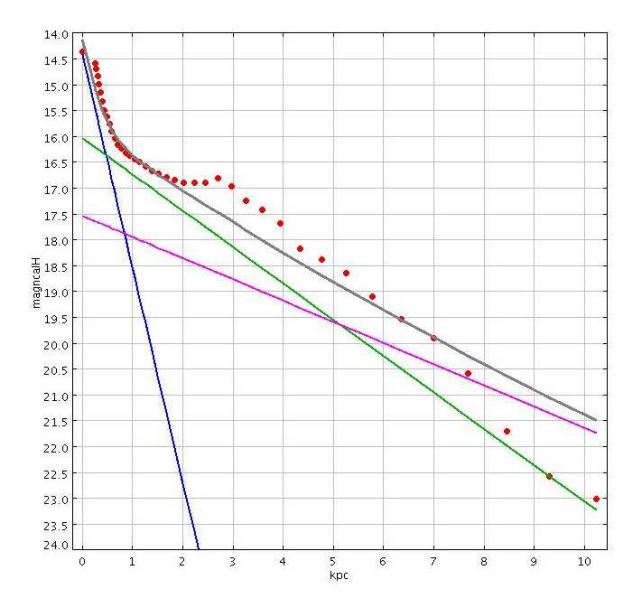


**Fig. 12.** Brightness profile of the r passband with the plotted curves made with empirical laws that represent the bulge and the two disks.

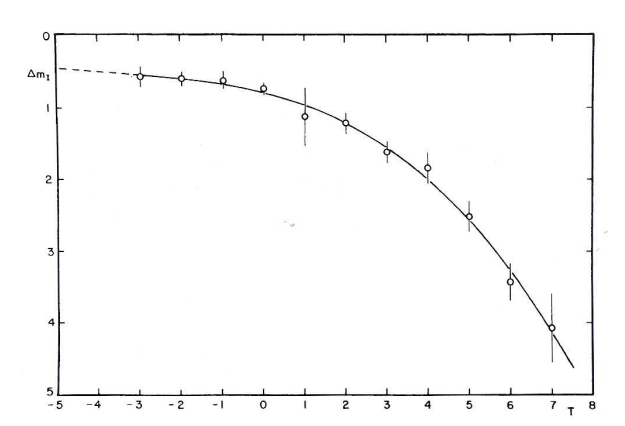


**Fig. 13.** This graph represents the relation between the  $\Delta m$  and the T-type.

bulge fraction of the galaxy B/T [I(B) over I(tot)], a parameter that is relevant to classify the morphology of a spiral galaxy. The mean value of B/T in g and H filters was 0.0507.

We determined the morphology type of NGC 2903 by using the T-Type scale, which is based on the value of  $\Delta m$ , the positive difference between the magnitudes of bulge and disk (this time the magnitudes are subtracted, so  $\Delta m$  is the logarithm of the fraction of Intensities B/D, as with B/T). We associated  $\Delta m = 3.19$  to T – Type = 5, comparing the results of bulge-to-disk ratios provided by the NASA Astrophysics Data System. The corresponding morphological type is Mixed (Barred) Spiral SBc, according to the coding table of Revised Morphological Types.

#### 3.2.4. Results

At the end of our work, we can compare the results of the studies about the brightness profiles and the residuals. By studying the brightness profiles, we found that in H and K<sub>S</sub> passbands (near Infrared) the intensity is greater than in g, r and i passbands (visible); this is due to the presence of gases and small materials that emit long-wavelength waves. These elements explain the starburst quality of the galaxy, as the production of stars inside it is a hundred times faster than in normal galaxies and this great production of stars require a lot of raw materials. A starburst galaxy derives from the interaction or merger of two galaxies; in this case, one is already inside the other. That caused the presence of two disks in the galaxy. By using the positive difference between the magnitudes of the bulge and the two disks, we found that NGC 2903 is a SBc Mixed Spiral; this means that it is very different from an elliptical one. The residuals (the difference between the galaxy and its virtual model made with the isophotes with unfixed centres) confirm it, as they are very significant (they are composed of the bar and the two long spiral arms). The bar can also be seen in the brightness profile, where it coincides with the horizontal part of the graph, and in the E-PA/SMA graphs; in these graphs, if E increases, but PA remains the same, it means that there is a bar.

#### 4. Conclusions

The two galaxies are morphologically different, as figures 7, 11, 12 and 13 show. The M59 brightness profile (figure 7) is almost identical to the theoretical curve because M59 is an elliptical galaxy, while NGC 2903's brightness profile (figures 11, 12 and 13) shows that the galaxy presents complex structures. The morphological models confirm this hypothesis, as M59 is very similar to its virtual model, as figure 6 shows, while the difference between the theoretical model and NGC 2903's actual image is quite evident in figures 9 and 10. The complete morphological analysis shows that M59 is an elliptical galaxy without arms or other structures, while NGC 2903 is a barred spiral galaxy with two separate disks. While studying NGC 2903, we encountered a peculiar phenomenon: the galactic center was much brighter in the infrared bands. The cause of this unusual brightness is the particularly intense stellar formation in NGC 2903's central regions.

#### References

Naab, T., Burkert, A. & Hernquist, L., On the Formation of Boxy and Disky Elliptical Galaxies, 1999

This research has made use of the NASA/IPAC Extragalactic Database (NED) which is operated by the Jet Propulsion Laboratory, California Institute of Technology, under contract with the National Aeronautics and Space Administration.



## Kinematics of spiral galaxies NGC2903 NGC3310 NGC3351 NGC660

Bertotto Niccolò<sup>1</sup>, Buffo Sacha<sup>1</sup>, Ceola Filippo<sup>2</sup>, Conti Matteo<sup>1</sup>

<sup>1</sup>Liceo scientifico "G.B. Quadri" – Vicenza <sup>2</sup>Liceo sperimentale "D.G. Fogazzaro" – Vicenza

**Abstract.** We studied spectra of galaxies NGC 2903, NGC 3310, NGC 3351, NGC 660 in order to measure redshifts, distances and masses within a certain radius. Observations were made at Asiago Observatory with the 1.22m Galileo Telescope and the Boller & Chivens spectrograph between February 3rd and February 4th 2010.

#### 1. Introduction

Galaxies are stellar systems composed by stars, dust and gas with a mass that ranges from  $10^8$  to  $10^{11}$  M<sub> $\odot$ </sub>. the determination of mass, internal kinematics and redshift of these stellar systems is of primary importance in modern astronomy. Spectroscopic observations are well suitable to obtain these measurements. During the night between February 3rd and February 4th 2010, we made an observational run using the 122cm "Galileo" telescope at Asiago - Colle Pennar equipped with a Boller & Chivens spectrograph. A 300 gr/mm grating was employed. We obtained spectra of galaxies NGC 2903, NGC 3310, NGC 3351, NGC 660 in order to get the rotational curve of these galaxies. From the rotational curves we analyzed the kinematics and, in particular, we estimated the mass of these objects within the observable radius.

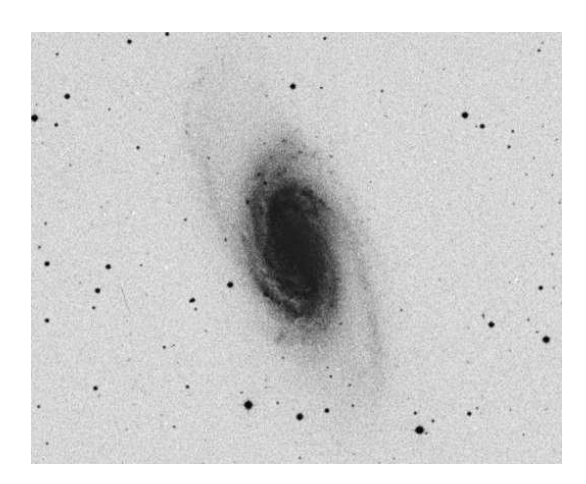


Fig. 1. Galaxy NGC2903 source: SAOdss

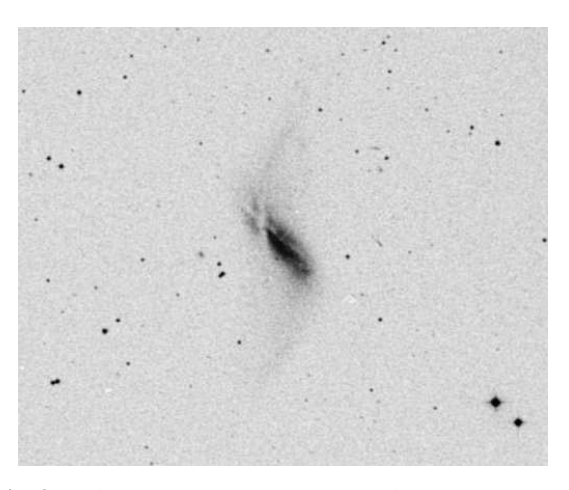


Fig. 2. Galaxy NGC660 source: SAOdss

#### 2. Observational Data

The following table shows the object list. In order to enhance the signal, we gathered 2 and 3 1800 seconds exposures for galaxy NGC660 ang NGC 2903 respectively. Slit width was  $250\mu$ .

NGC	α	δ	Class.
660	1h 43m	+13° 38′	SB(s)a-pec
2903	9h 32.2m	+21° 30′	SAB(rs)bc
3310	10h 38.7m	$+53^{\circ}\ 30^{'}$	SAB(r)bc
3351	10h 44m	+11° 42′	SB(r)b

Classification comes from NED archive. Note that the galaxies show rings and a peculiar morphological type.

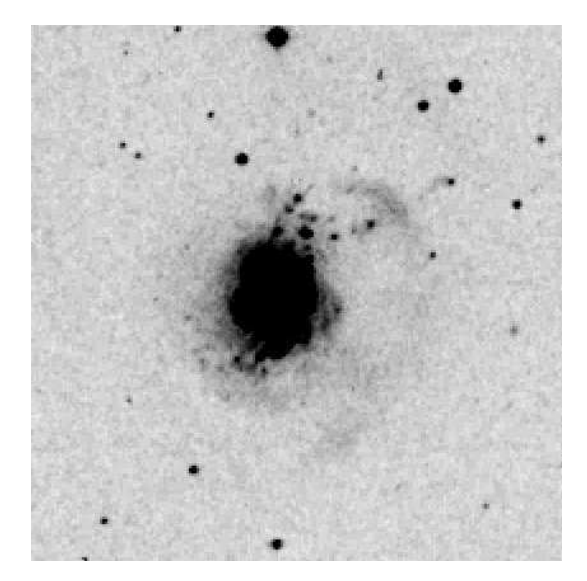


Fig. 3. Galaxy NGC3310

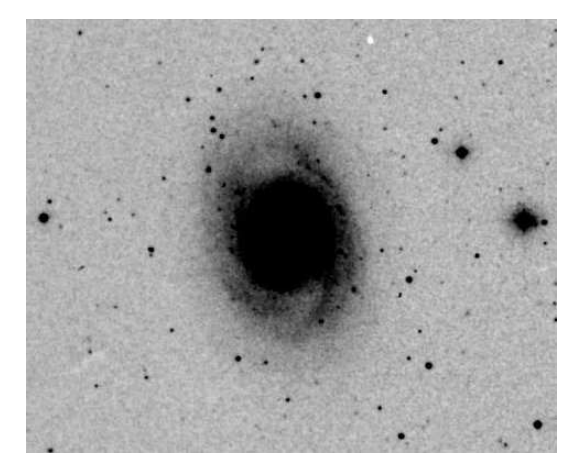


Fig. 4. Galaxy NGC3351

Spectra were reduced with IRAF software package (NOAO) in the standard way. Wavelenght calibration was made through the comparison with spectra of a HgAr and a Ne lamp, while flux calibration was achieved through HD84937 standard star. We focused on  $H_{\alpha}$  emission lines: we could calculate the redshift of galaxies and the distance through the Hubble's law. The orientation of the slit was not the same for each galaxy: for the object NGC 660 the slit was moved  $14^{o}$  est from the major axis, for NGC 3310  $35^{o}$  est, for NGC 3351  $15^{o}$  est and, in particular, for NGC 2903 the slit was moved  $32^{o}$  west to be able to catch a guide star in the camera field.

### 3. Work description

We measured the wavelenght of the  $H_{\alpha}$  emission line, scanning the frame in normal direction with respect to the wavelength. To enhance the signal we considered,

for each step, the mean value of five row on the ccd frame. Through the Doppler effect formula:

$$V_{rad} = \frac{\Delta \lambda}{\lambda_0} \cdot c \tag{1}$$

the recession velocity  $V_{rad}$  was obtained. Knowing the telescope scale (0.6''/pix) and thanks to the measured galaxy's distance, we were able to obtain the radial velocity curve (Km/s – Kpc)

We deprojected radial velocities and the radius of the galaxies, considering the extimated inclination angle and the slit position with respect to the major axis.

$$\tan(\theta) = \frac{\tan(\Phi)}{\cos(i)} \tag{2}$$

where  $\theta$  is the point position angle in the galaxy disk plane,  $\Phi$  is the point position angle in the plane of the sky, and i = arcsin(b/a) is the inclination angle

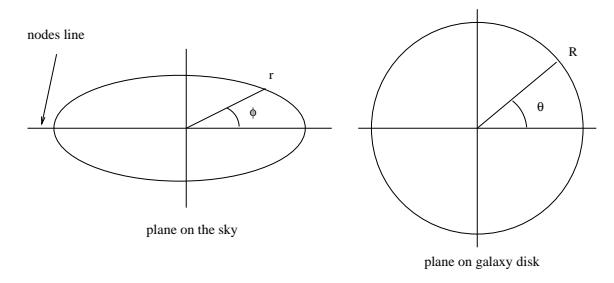


Fig. 5. galaxy disk projection

Hence, from the observed  $V(r, \Phi)$  and r we have:

$$V_{deproj} = \frac{V(r, \Phi)}{\cos(\theta) \sin(i)}$$
 (3)

$$R = r \cdot \frac{\cos(\Phi)}{\cos(\theta)} \tag{4}$$

To evaluate the velocity curves we adopted the following formula:

$$V(R) = A \cdot R \cdot (R^2 + C0^2)^{-p/2}$$
 (5)

*A*, *C*0 and *p* are free parameters; *p* ranges from 1 to 1.5 accordingly with Bertola *et al.* 1991.

NGC	A	C0	p
660	220	0.65	1.1
2903	70	0.05	1.5
	210	2.2	1.
3310	80	0.05	1.5
	320	4.	1.
3351	90	0.15	1.35

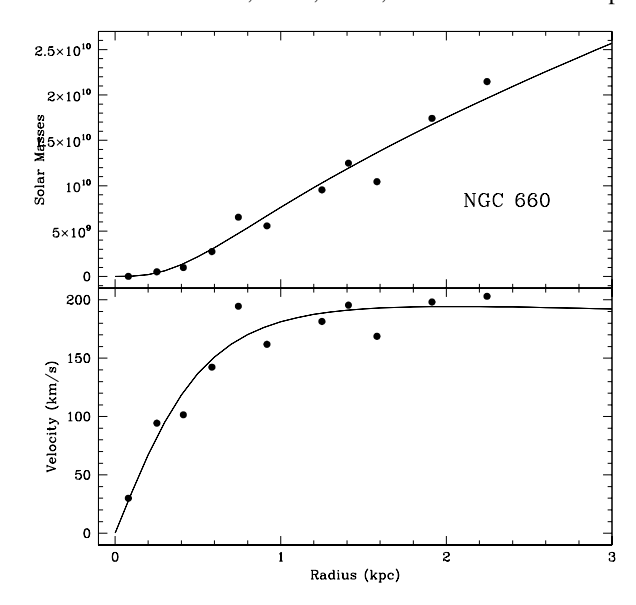


Fig. 6. Radial velocity curve and mass of NGC 660

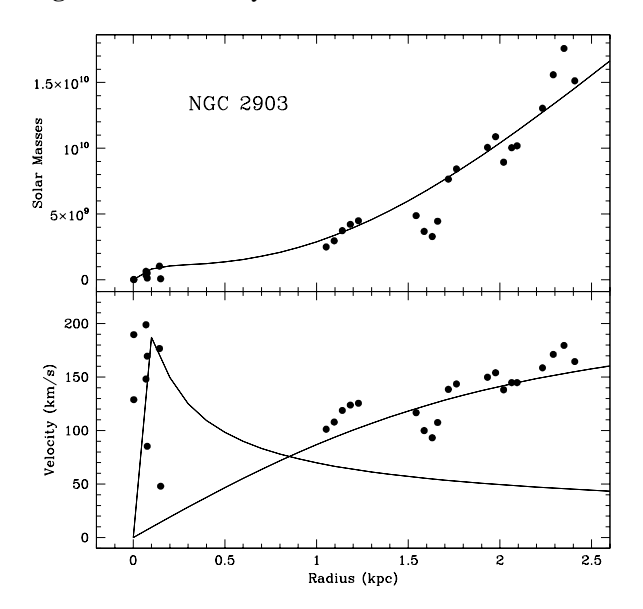


Fig. 7. Radial velocity curve and mass of NGC 2903

The mass as function of the radius R is given by :

$$M(R) = \frac{A^2 \cdot R^3}{G \cdot (R^2 + C0^2)^p} = \frac{V^2(R) \cdot R}{G}$$
 (6)

where G is the universal gravitational constant. We did not employ a rigorous fitting procedure, so the parameters should be considered simply as a reasonable guess obtained by trial and error.

NGC	V (Km/s)	D (Mpc)	$M_{\odot} 10^{9}$
660	911.9	12.1	17.5
2903	571.8	7.6	10.7
3310	975.9	13.0	11.0
3351	763.3	10.1	1.2

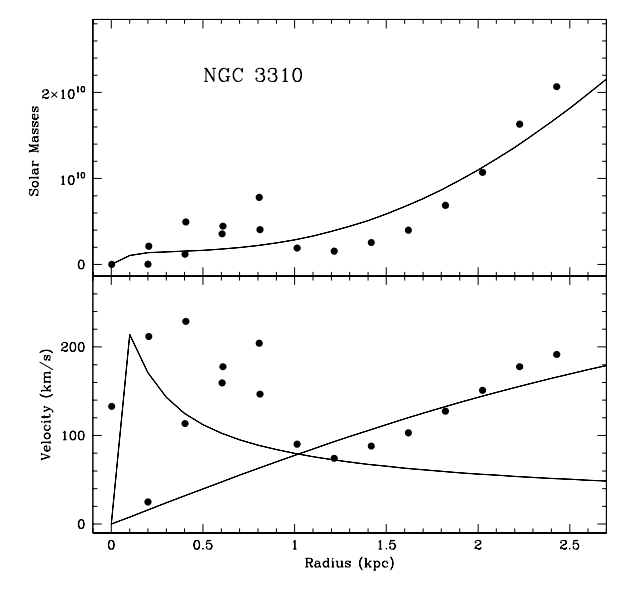


Fig. 8. Radial velocity curve and mass of NGC 3310

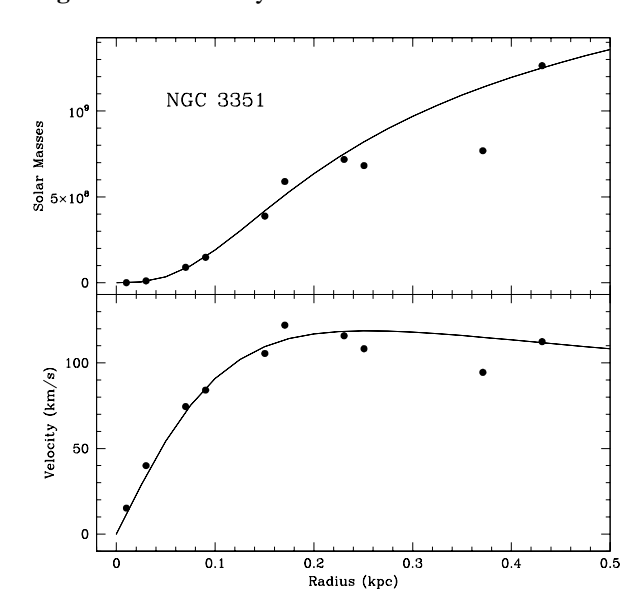


Fig. 9. Radial velocity curve and mass of NGC 3351

In this table the masses were determined at 2 Kpc from the galaxy center but NGC 3351, whose mass refer to 0.4 Kpc from the center.

Distances were computed through Hubble's law  $V = H \cdot d$ . We adopted:  $H = 75Km/(s \cdot Mpc)$ .

#### 4. Results

The radial velocity, distance and radial velocity curve of NGC 660, NGC 2903, NGC 3310 anf NGC 3351 were obtained. Radial velocities and distances we derived from our spectra are in good agreement with (e.g.) the data from the NED archive. The guessed radial velocity curves and the computed masses seem reasonably acceptable. For NGC 3310 and NGC 2903 we suggest

two distinct components. A solution for NGC3310 was difficult to find; this could mean that this galaxy has perturbed dynamics, as proposed by Kregel and Sancisi (2001). The masses were computed at a reference radius of 2 Kpc but NGC 3351, for which the mass was evaluated at 0.4 Kpc radius. In fact, no measurements outside this radius were obtained, due to the poor signal

#### References

Bertola, Bettoni, Danziger, Sadler, Sparke, De Zeeuw 1991, ApJ, 373, 369 Kregel, Sancisi, 2001 A.& A. 376, 59



## The mass of galaxies in the Abell 671 cluster

Ancona Marco<sup>1</sup>, Loro Arianna<sup>1</sup>, Trubian Stefano<sup>1</sup>, Mansutti Giulia<sup>1</sup>

<sup>1</sup>Liceo E. Curiel, sez. Scientifico, Padova

**Abstract.** The aim of this research was to calculate the mass of different galaxies using the virial theorem, which connects together the effective radius and the velocity dispersion. The galaxies are located in the Abell 671 cluster.

#### 1. Introduction

According to the virial theorem, the stars of a galaxy are prevented from collapsing towards the galaxy centre by their own movement; thus there is an equilibrium between kinetic and potential energy. A generalization for gravitational energy of this theorem states that

$$2K + P = 0 \tag{1}$$

where K represents the kinetic energy and P the potential energy. From this theorem derives another equation, which enables to calculate the mass of the galaxy:

$$I = \frac{Re \cdot \sigma^2}{8.33 \cdot G} \tag{2}$$

where Re represents the effective radius and  $\sigma$  the velocity dispersion. Both the elliptical galaxies and bulges of spiral galaxies are characterized by stars that have different velocities that form a gaussian distribution:  $\sigma$  represents the average variation from the mean. The effective radius is the radius of the imaginary circle that includes half of the galaxy light.

#### 2. Observational Data

The images used for this research were taken from the public archive of the Sloan Digital Sky Survey (SDSS). SDSS is a project that provides optical images covering more than a quarter of the sky and a tridimensional map containing about one million galaxies and 120000 quasars. SDSS used a 2.5 m telescope at Apache Point in New Mexico. For the photometric survey were used five filters (u, g, r, i, z).

The study was focused on the Abell 671 cluster, which is estimated to be around 600 million light years away. From that cluster eleven galaxies were selected. The examined galaxies are reported in the following table and marked in Fig.1.

Ref	Object name	RA (deg)	DEC (deg)
215	KUG 0826+305	127.35869	30.42468
227	2MASX J08285059+3035474	127.21100	30.59652
253	IC 2380	127.18286	30.40453
259	2MASX J08291010+30230541	127.29205	30.38493
292	2MASX J08282365+3022513	127.09844	30.38092
296	CGCG 149-029 NED02	127.11357	30.41421
297	2MASX J08283454+3015583	127.14380	30.26639
302	IC 2378	127.13186	30.43133
304	IC 2374	127.09223	30.44320
564	2MASX J08282280+3021233	127.09506	30.35637
574	2MASX J08280564+3027082	127.02353	30.45215

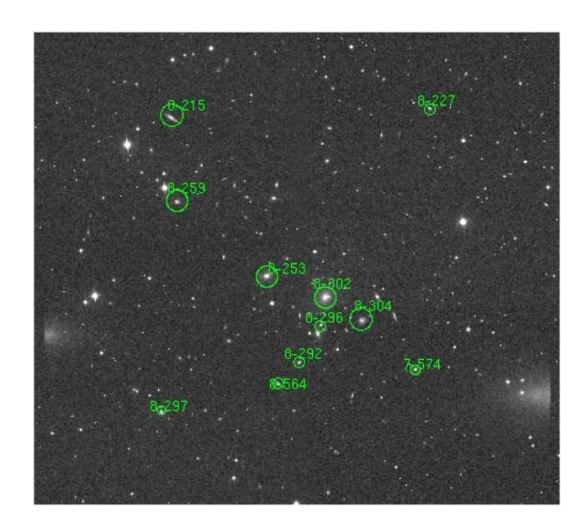


**Fig. 1.** The Abell 671 cluster. Marked galaxies are the ones examined. Numbers refer to the "Ref" column in the previous table.

#### 3. Work description

This research could be divided into two parts: in the first, the effective radius was calculated and in the second, the velocity distribution was studied.

#### 3.1. Calculation of the effective radius

First of all, the biggest galaxies were chosen among the whole cluster and isolated from the others. Then IRAF was used in order to find each galaxy's isophotes, which are imaginary lines that link together the points with the same brightness. For elliptical galaxies a first ellipse was drawn to encircle the external edge of the galaxy, while for spiral galaxies the ellipse contained only the bulge. This work was done twice: the first time holding the centre of the isophotes, the second with variable centres. From this second study the trend of the ellipticity in function of the semi-major axis was observed: elliptical galaxies present a more regular ellipticity and a simpler structure than spiral galaxies. The morphology of the galaxies was also deducted from the variations on the position of the galaxy centre: elliptical galaxies have a fixed centre, while any movements of the centre indicate different types of galaxies. From the first study, instead, the superficial intensity of the galaxies was extracted from the relation:

$$I = \frac{i - (i_c \cdot n_p)}{t \cdot S_p} \tag{3}$$

where I is the superficial intensity, i the intensity of each isophote,  $i_c$  the intensity of the sky,  $n_p$  the number of pixels in each isophote, t the exposure time of the image and  $S_p$  the area of each pixel. This work was due to find

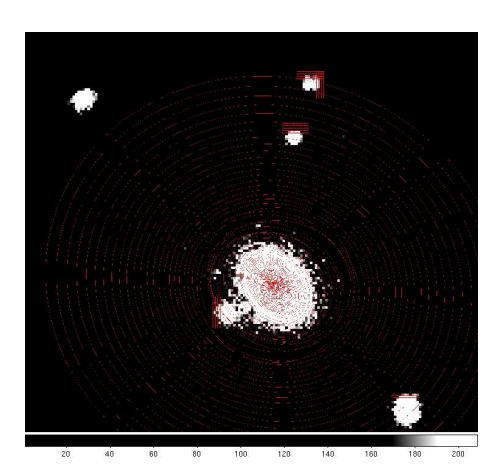


**Fig. 2.** Isophotes of galaxy 297. Red lines connect points with same brightness.

the brightness of the galaxies, which can be calculated using the equation:

$$B = -2.5 \cdot \log_{10} I \tag{4}$$

where B is the brightness and I the superficial intensity. Then it is possible to trace a graph that relates the brightness (on the ordinate axis) and the semi-major axis elevated to the  $\frac{1}{4}$ th (on the abscissa axis). The graph represents the brightness profile, which describes the brightness (magnitude per unit area) as a function of the

semi-major axis. If the resultant function is a straight line, the galaxy is elliptical, otherwise the galaxy is a spiral. The theoretic function has been adapted to the sperimental one using Sersic's law. From this law, two different equations had been extracted. The first is De Vacouleurs's law, used for elliptical galaxies:

$$\mu_b = \mu_e + 8.325 \cdot \left[ \left( \frac{R}{R_e} \right)^{\frac{1}{4}} - 1 \right] \tag{5}$$

The second is the equation of the exponential bulge:

$$\mu_b = \mu_e + 1.824 \cdot (\frac{R}{R_e} - 1) \tag{6}$$

where  $R_e$  is the radius of the isophote containing half the luminosity and  $\mu_e$  is the surface brightness at  $R_e$ .

This equation was used for spiral galaxies and the resultant function had to fit only the part of the experimental graph concerning the bulge. Once found the theoretical function that fits best the experimental one, it is possible to calculate the effective radius.

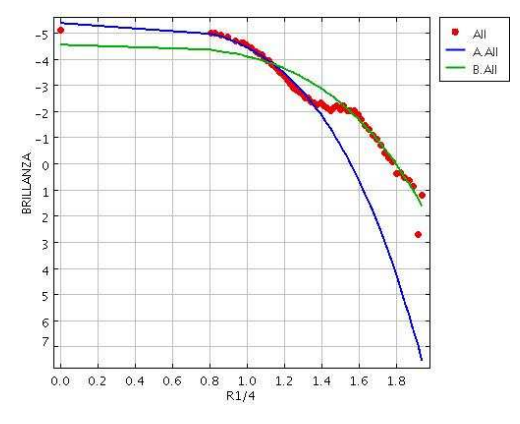


**Fig. 3.** Brightness profile of barred galaxy number 227 (ref. Fig. 1). The red dots are the observational data, the blue line represents the theoretical function for the bulge and the green one the theoretical one for the external disc.

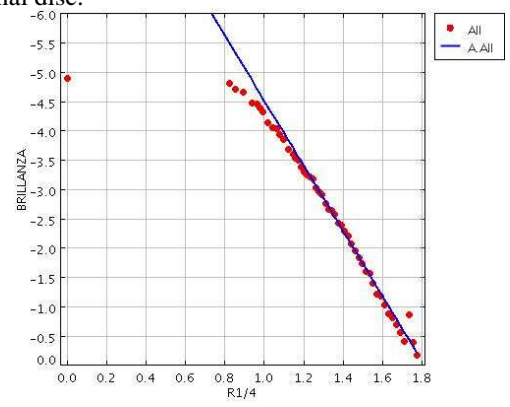


**Fig. 4.** Brightness profile of elliptical galaxy 296 (ref. Fig.1). The red dots are the observational data and the red line the theoretical function.

#### 3.2. Calculation of the velocity dispersion

The study proceeded in order to calculate the parameters of the velocity distribution, using the cross-correlation method. Unlike the spectrum of a star, the spectrum of a galaxy presents stretched lines because of the kinematic effect. Considering that the velocity dispersion of the stars in a galaxy follows a normal distribution, the width of the correlation pick is function of  $\sigma$ . We first compared the original spectrum of a F class star with its spectrum opportunely modified considering a  $\sigma$  value variable from 50 to 400 km/sec. From each comparison we obtained a correlation peak whose width was measured. The same operation was also repeated with a G class star and with a K class star, because the dominant stellar component was initially unknown.

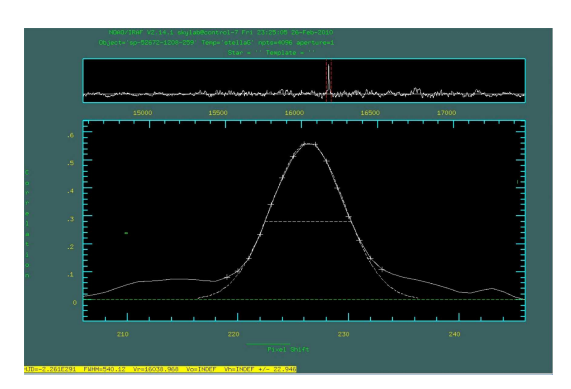


**Fig. 5.** On the top, the correlation function with the correlation peak marked. On the bottom, gaussian velocity distribution of galaxy number 259 (ref. Fig.1).

Finally, comparing the spectra of stars and galaxies, we managed to calculate the width of the peaks and to obtain the  $\sigma$  value as an average of the 3 results (one for each star class).

The following table reports  $\sigma$  values for each star class, their average, and the effective radius of the examined galaxies. Object numbers refer to Fig.1.

Object	$\sigma_{\it K}$	$\sigma_G$	$\sigma_F$	$\sigma$	$R_e$ (kpc)
215	105.7	89.3	97.5	97.5	8.176
227	108.9	113.0	125.4	115.8	0.780
253	262.6	246.0	254.7	254.4	5.386
259	131.0	136.0	160.8	142.6	0.828
292	127.7	130.2	125.5	127.8	1.845
296	221.2	210.0	223.2	218.1	2.095
297	251.0	224.0	233.0	236.0	2.544
302	300.5	280.0	292.0	290.8	14.137
304	87.0	131.5	140.5	129.7	0.776
564	184.0	149.5	210.0	181.2	0.711
574	118.1	97.0	135.7	117.0	1.866

After calculating the effective radius and the parameter of the velocity ditribution, it is possible to calculate

the mass of the galaxy. The effective radius was converted first from pixels to arcseconds (1 pixel = 0.4 arcseconds) and then from arcseconds to kiloparsecs. Finally, the mass was calculated using the equation:

$$I = \frac{Re \cdot \sigma^2}{8.33 \cdot G} \tag{7}$$

where  $R_e$  is the effective radius and  $\sigma^2$  the square of the arithmetic mean of the three  $\sigma$  values previously found.

#### 4. Results

As a result of the study, the masses of the galaxies were calculated and their values are reported in the following table. Object numbers refer to Fig.1.

Object	Туре	Mass (kg)	Solar masses
215	Spiral	$1.089 \cdot 10^{41}$	$5.474 \cdot 10^{10}$
227	Barred spiral	$1.465 \cdot 10^{40}$	$7.366 \cdot 10^9$
253	Elliptical	$4.885 \cdot 10^{41}$	$2.456 \cdot 10^{11}$
259	Barred spiral	$2.360 \cdot 10^{40}$	$1.187 \cdot 10^{10}$
292	Elliptical	$4.838 \cdot 10^{40}$	$2.432 \cdot 10^{10}$
296	Elliptical	$1.396 \cdot 10^{41}$	$7.020 \cdot 10^{10}$
297	Elliptical	$1.985 \cdot 10^{41}$	$9.980 \cdot 10^{10}$
302	Elliptical	$1.675 \cdot 10^{42}$	$8.422 \cdot 10^{11}$
304	Barred spiral	$1.557 \cdot 10^{40}$	$7.827 \cdot 10^9$
564	Spiral	$3.271 \cdot 10^{40}$	$1.644 \cdot 10^{10}$
574	Elliptical	$3.575 \cdot 10^{40}$	$1.797 \cdot 10^{10}$

Normal mass ranges are  $10^7$  -  $10^{14}~M_{\odot}$  for elliptical galaxies and  $10^9$  -  $10^{12}~M_{\odot}$  for the bulge of spiral galaxies. All our results are within these ranges.

Abell 671 is estimated to be around 600 million light years away. A great number of galaxies of various types can be detected but it contains mainly ellipticals probably because of interactions between its members that have stripped away gas and material.

#### References

Antonucci, R.R.J & Miller, J.S. 1985, ApJ, 297, 612 Antonucci, R. 1993, ARA&A, 31, 473 Cid Fernandes, R., et al. 2004, ApJ, 605, 105 Cid Fernandes, R., Mateus, A., Sodré, L., Stasińska, G., & Gomes, J. M. 2005, MNRAS, 358, 363



## Mass, luminosity and velocity dispersion of the ABELL 671 cluster

Roberto Casotto<sup>1</sup>, Andrea Galtarossa <sup>2</sup>, Michele Gambuto<sup>3</sup>, Carlo Alberto Gottardo<sup>4</sup>, Marco Perini<sup>2</sup>, Francesco Sovrano<sup>4</sup>, Nicola Viafora<sup>4</sup>

<sup>1</sup>Liceo G. Galilei, sez. Scientifico, Selvazzano
 <sup>2</sup>Liceo E. Fermi, sez. Scientifico, Padova
 <sup>3</sup>Liceo F. Morosini, sez. Scientifico, Venezia
 <sup>4</sup>Liceo I. Nievo, sez. Scientifico, Padova

**Abstract.** We studied the magnitudes and the redshifts of the galaxies belonging to the ABELL 671 cluster in order to calculate the mass and luminosity of the cluster and the velocity dispersion of the galaxies in it.

#### 1. Introduction

The ABELL 671 cluster contains about 40 galaxies among which there are a few big ones (their size is a little smaller than that of our Galaxy) and many dwarf galaxies. The work was made at the Asiago Astrophysics Observatory during the project "Il Cielo come Laboratorio" on February 24th-27th 2010. Because of unfavorable weather, the group worked on previously acquired data: photometric images of the cluster and spectra of the single luminous objects detected in the images. Thanks to the Sextractor software, the group obtained the apparent magnitudes of the light sources using g, r, i, z filters, belonging to the ugriz system, and then transformed their values according to B, V, R, I filters. To calculate the redshift of the galaxies, the team referred to absorption lines of some Milky Way stellar spectra; the chosen lines were CaH, Mg, Na,  $H_{\alpha}$  and Ca II. Moreover, emission spectra of the galaxies were considered, but only  $H_{\alpha}$  line was regarded. Average redshift value for every galaxy was used to determine recession velocity, useful to select the galaxies belonging to the cluster. Then, absolute magnitude was measured. Absolute magnitude allowed to extract the cluster luminosity, velocity dispersion, harmonic radius, and then the mass of the whole cluster. The work was accomplished by two different workgroups, who at first worked simultaneously on the same data and images, to finally compare the results.

#### 2. Observational Data

The study began with 25'x 25' sky images of the cluster ABELL 671 seen though g, r, i, z filters. The software

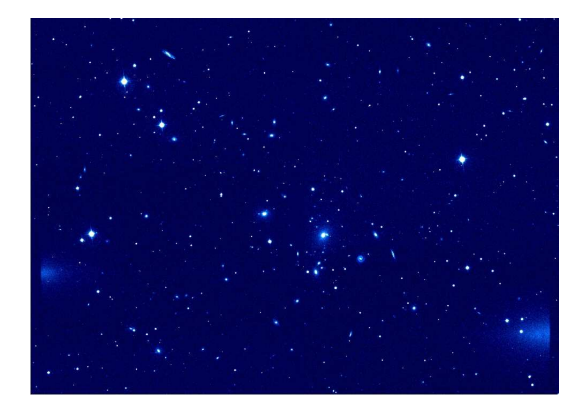


Fig. 1. The ABEL 671 cluster

Sextractor detected the number of sufficiently luminous sources according to the parameter DETECT-TRESH set on values between 3 and 4. The number of recognized sources is reported in the following table:

Filter g	1228 sources
Filter r	1570 sources
Filter i	1732 sources
Filter z	879 sources

Then, every identified source was circumscribed into an ellipse defined by the shape of the object (fig.2).

To calculate the redshift of a single galaxy, emission and absorption spectra, previously collected selecting only the ones corresponding to the objects taken into account by Sextractor, were used.

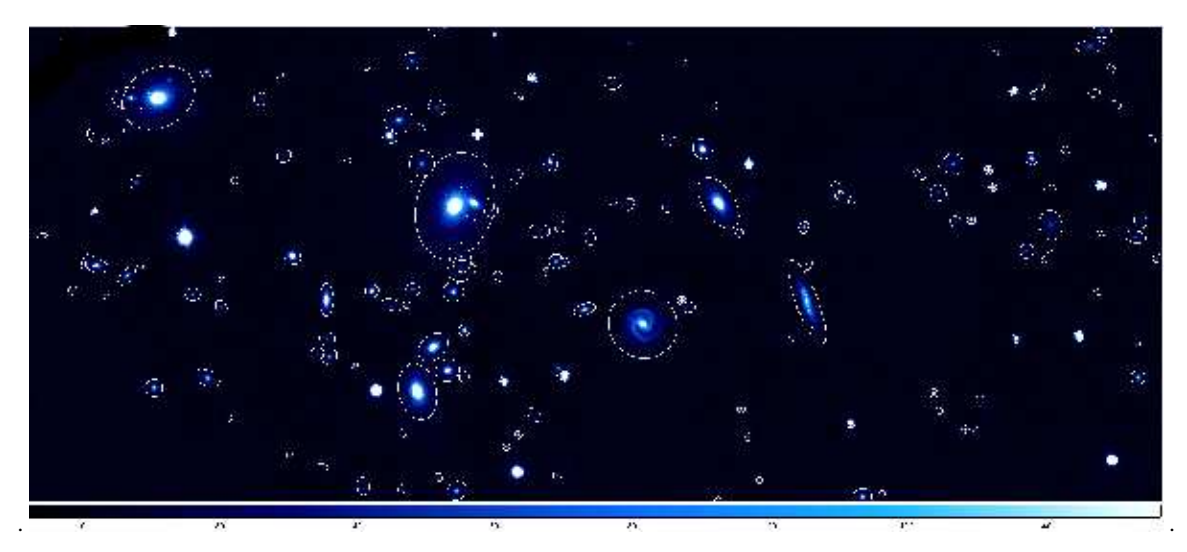


Fig. 2. Sources identification on a g filter using Sextractor

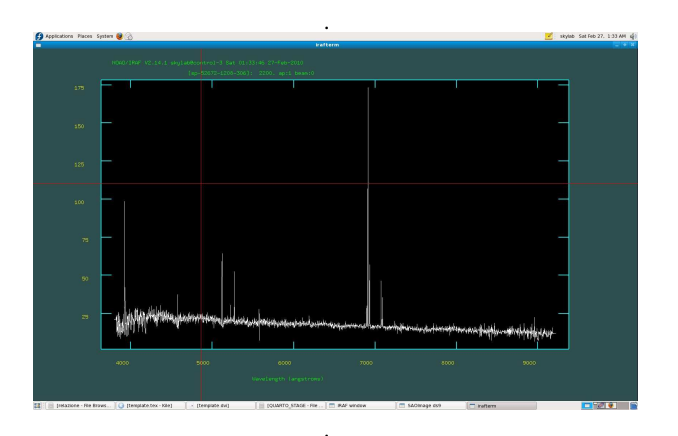


Fig. 3. Emission spectrum of a galaxy from ABELL 671

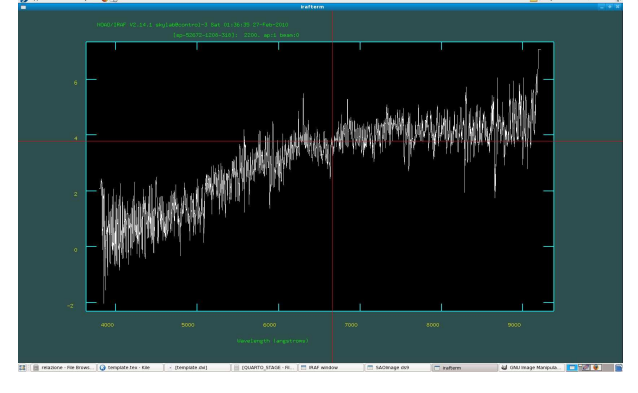


Fig. 4. Absorption spectrum of a galaxy from ABELL 671

### 3. Work Description

The first step was to select enough luminous and elliptic sources to be galaxies in each filter images. The Sextractor parameter that analyzes luminosity is based on Root Mean Square (RMS) defined as:

$$\sigma = \sqrt{\sum (x - \bar{x})^2 / (n - 1)} \tag{1}$$

It measures the luminosity difference of two pixels in order to distinguish areas brighter than an average (corresponding approximately to the sky background luminosity). Once recognized the sources, the Sextractor parameter CLASS-STAR discerned the stars from the galaxies assigning a value between 0 (galaxy) and 1 (star) to the objects. In this way it was possible to reduce the number of objects to analyze, discarding the ones that were clearly not galaxies (fig. 5).

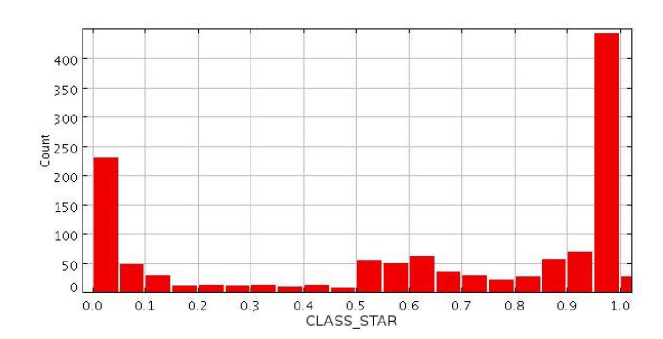


**Fig. 5.** Distribution of stellar objects as identified by the CLASS-STAR parameter: col9 stands for CLASS-STAR

The group obtained 4 tables (one for each filter) containing the apparent instrumental magnitude, coordinates and ellipticity of the objects.

Calibrated magnitudes for each filter were calculated using the following formula:

$$m_{cal} = m_s + m_0 - k_\lambda \cdot x_\lambda - 25 \tag{2}$$

where  $m_s$  stands for the instrumental magnitude measured by Sextractor,  $m_0$  is a constant, called photometric zero point, that transforms the value of  $m_s$  (expressed in number of photons) into  $erg/cm^2$ , while  $k_\lambda$  is the airmass crossed by the light rays and  $x_\lambda$  is the coefficient of atmospheric extinction which is proportional to the airmass and depends on the wavelength of the photons. The values we used are reported in the following table:

Filter	$k_{\lambda}$	$x_{\lambda}$
g	0.161 mag	1.010
r	0.082 mag	1.012
i	0.032 mag	1.012
Z	0.034 mag	1.010

The -25 coefficient is needed to measure the real value of the calibrated magnitude because the instrumental magnitude was increased by 25 to grant a positive value. Finally, the exposition time of 54 sec (i.e. the time spent by the telescope camera to acquire the image on which apparent magnitude where defined) must be considered. After few steps the equation becomes:

$$m_{cal} = 2.5 \cdot \log(t_{exp}) + 2.5 \cdot \log(I) - k_{\lambda} \cdot x_{\lambda} - 25$$
 (3)

where I is the luminosity expressed in  $erg/cm^2s$ . With the proper formulas,  $m_{cal}$  can be transformed into the UBVRI system, obtaining B, V, R, I magnitudes that can be used to build the color index distribution diagram (see fig. 6).

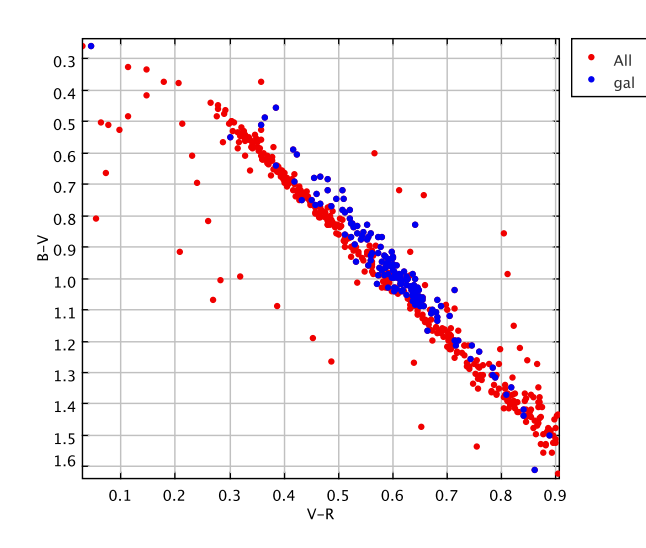


**Fig. 6.** The distribution of the galaxies in the V-R B-V diagram. Blu points are galaxies, red ones are stars.

A quadruple match was made with TOPCAT in order to unify the objects with the same coordinates that were in all four tables, obtaining a single table with 72 galaxies. The table so obtained was matched with the one containing the spectra files in order to connect every detected galaxy to its spectrum. Every spectrum was displayed and examined with IRAF (Image Reduction and Analysis Facility) taking as a reference absorption lines (CaH, Mg, Na,  $H\alpha$  and CaII). We divided in two the work, so that each group analyzed 36 spectra, measuring the difference between the wavelength of the redshifted galactic lines and the laboratory wavelengths (see fig.7).

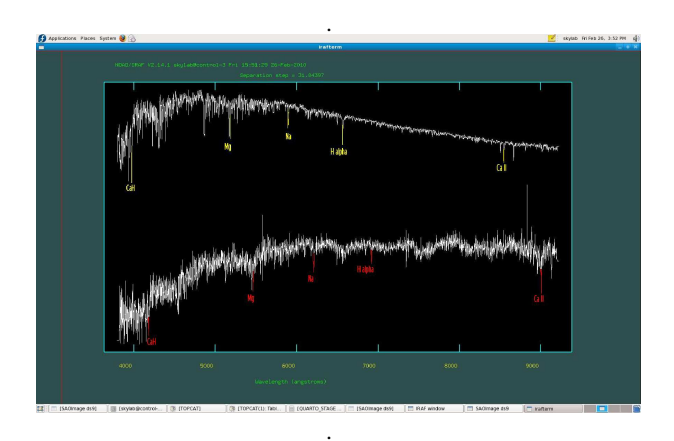


**Fig. 7.** Comparison between two spectra: above there is a stellar spectrum, whereas on the bottom there is a galactic one. It can be seen that galactic lines (in red) are shifted to the right (red-shift)

The redshift of every line is computed through the formula:

$$z = (\Delta \lambda / \lambda) \tag{4}$$

The redshift of the galaxy was drawn taking the mean of the lines redshifts. Multiplying it by the speed of light in the vacuum, we got the recessional velocity of the galaxy. Unifying the data obtained by both the working groups and building an histogram, it can be noticed that there are a recurrent redshift around 0.05 and a recurrent recessional velocity of about  $1.5 \cdot 10^4 \text{kms}^{-1}$ . Only the 44 galaxies presenting these values were taken into account.

Applying Hubble's law to each of the 44 galaxies, the distance of the cluster was thus extracted:

$$V = d \cdot H \tag{5}$$

where V equals to  $1.5 \cdot 10^4 \text{kms}^{-1}$  and Hubble constant is  $75 Km/(s \cdot Mpc)$ . The distance derived was about 200 Mpc.

Knowing the distance of the cluster, it was possible to find the absolute magnitude (in B, V, R, I filters)

of every galaxy, exploiting the distance modulus definition:

$$M - m = 5 - 5 \cdot \log(d) \tag{6}$$

The absolute magnitudes were converted into luminosities, measured in solar luminosities, through the equation:

$$L_{\rm B} = 10^{-0.4(M_{\rm B} - M_{\odot})} \cdot L_{\odot} \tag{7}$$

Adding all the galaxies luminosities, we got the cluster luminosity equal to  $4.485*10^{11}$  solar luminosities.

Afterward, the group obtained the velocity dispersion i.e. the range of velocity differences from the average value of 15000kms<sup>-1</sup>. Velocity dispersion, for definition, has the same expression as the RMS:

$$\sigma = \sqrt{\frac{\sum (V_i - \bar{V})^2}{\sum (L_i)}} \tag{8}$$

Introducing in the formula the recession velocity of every galaxy, the velocity dispersion equals to 785 Km/s. Finally, to find the mass of the whole cluster it was necessary to calculate the harmonic radius i.e. the radius containing half the luminosity of the cluster, considering as centre the central galaxy. Harmonic radius is defined as:

$$R_{\rm H} = \frac{\sum (L_{\rm i})^2}{2 \cdot \sum (\frac{L_{\rm i} \cdot L_{\rm j}}{R_{\rm ii}})} \tag{9}$$

where the numerator is the summation of the square power of the luminosity of each galaxy divided by the summation of relative luminosity divided by the mutual distance between galaxies.

The application of Pythagoras' theorem, considering the galaxies lying on a plane as they are approximately equally distant, provided the reciprocal distances:

$$R_{12} = \sqrt{(x_2 - x_1)^2 + (y_2 - y_1)^2}$$
 (10)

We introduced the coordinates of all the galaxies, obtaining 946 mutual distances. Substituting these values in the equation of the harmonic radius, we derived a value of 971.37 pixels or 388.55 arcseconds, which converted into kiloparsec gave a value of 376 kpc and converted in kilometers gave  $1.16 \cdot 10^{19}$  Km (see fig.8).

These last values can be used to find the mass of the cluster through the equation:

$$M = \sigma^2 \cdot R_H \cdot 3\pi/G \tag{11}$$

The value derived was  $5.06 \cdot 10^{14}$  solar masses.

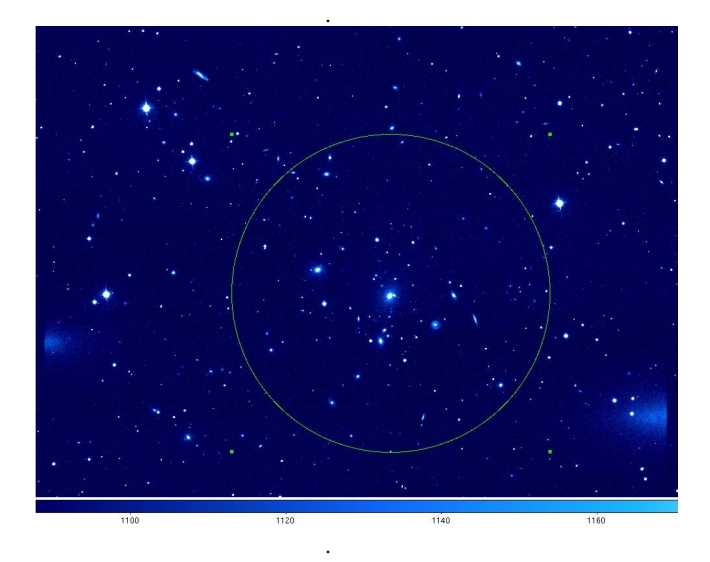


Fig. 8. The extension of the harmonic radius of the cluster

#### 4. Results

From spectroscopic and photometric observational data of the ABELL 671 cluster, information about velocity dispersion, luminosity and mass of the cluster were acquired through computer elaboration. The result is that the mass of the whole cluster is  $5.06 \cdot 10^{14}$  solar masses.

## Index

ugriz PSF photometry of the globular cluster M53	p.	1
Photometric analysis of the open cluster NGC2420	p.	7
Temperature and radius analysis of 5000 stars	p.	13
Relation between spectral lines and temperature of a star	p.	17
Study of the stellar population of the galaxies NGC3351, NGC660, NGC2903, NGC3310	p.	21
Spectroscopy of NGC6720	p.	27
Star Formation Rate in NGC2903, NGC3310 and NGC3351	p.	31
ugriz & JHK $_{\rm S}$ photometry of elliptical galaxy M59 and spiral galaxy NGC2903	p.	37
Kinematics of spiral galaxies NGC2903, NGC3310, NGC3351, NGC660	p.	45
The mass of galaxies in the Abell671 cluster	p.	49
Mass, luminosity and velocity dispersion of the ABELL671 cluster	p.	53